FINAL SCIENTIFIC/TECHNICAL REPORT
COVER PAGE

DEPARTMENT OF ENERGY
NATIONAL ENERGY TECHNOLOGY LABORATORY

DOE AWARD NUMBER: DE-FE 0008774

PROJECT TITLE: FABRICATION AND PROCESSING OF NEXT-GENERATION OXYGEN CARRIER MATERIALS FOR CHEMICAL LOOPING COMBUSTION

PI: PROFESSOR, Arunan Nadarajah, PhD

SUBMITTING OFFCIAL: Arunan Nadarajah

(419) 530-8031

nadarajah@utoledo.edu

SUBMISSION DATE: April 26, 2017

DUNS NUMBER: 05-162-3734

RECIPIENT ORGANIZATION: THE UNIVERSITY OF TOELDO

2801 W. BANCROFT ST., TOLEDO, OH 43606-3390.

PROJECT PERIOD: 09/04/2012 – 09/03/2016

TYPE OF REPORT: FINAL REPORT

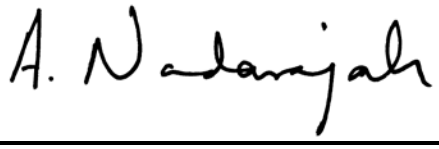

Arunan Nadarajah, PI

THE UNIVERSITY OF TOLEDO

SIGNATURE OF THE SUBMITTING OFFICIAL

DISCLAIMER* -- The Disclaimer must follow the title page, and must contain the following paragraph:

Abstract

Among numerous methods of controlling the global warming effect, Chemical Looping Combustion is known to be the most viable option currently. A key factor to a successful chemical looping process is the presence of highly effective oxygen carriers that enable fuel combustion by going through oxidation and reduction in the presence of air and fuel respectively. In this study, $CaMnO_{3-\delta}$ was used as the base material and doped on the A-site (Sr or La) and B-site (Fe, Ti, Zn and Al) by 10 mol % of dopants. Solid state reaction followed by mechanical extrusion (optimized paste formula) was used as the preparation method A series of novel doped perovskite-type oxygen carrier particles (Ca_xLa (Or Sa)$_{1-x}$ $Mn_{1-y}B_yO_{3-\delta}$ (Bsite = Fe, Ti, Al, or Zr)) were synthesized by the proposed extrusion formula. The produced samples were characterized with XRD, SEM, BET and TGA techniques. According to the results obtained from TGA analysis, the oxygen capacity of the samples ranged between 1.2 for CLMZ and 1.75 for CSMF.

Reactivity and oxygen uncoupling behaviors of the prepared samples were also evaluated using a fluidized bed chemical looping reactor using methane as the fuel at four different temperatures (800, 850, 900, 950 °C). All of the oxygen carriers showed oxygen uncoupling behavior and they were able to capture and release oxygen. Mass-based conversion of the perovskites was calculated and temperature increase proved to increase the mass-based conversion rate in all of the samples under study. Gas yield was calculated at 950 °C as well, and results showed that CLMZ, CM and CSMF showed 100% gas yields and CLMF and CSMZ showed approximately 85% yield in fluidized bed reactor, which is a high and acceptable quantity.

Based on extended reactor tests the modified calcium manganese perovskite structures (CSMF) can be a good candidate for future pilot tests.

Keywords: Porous perovskite, Chemical looping combustion and Calcium manganese

Contents

EXECUTIVE SUMMARY

Among numerous methods of controlling the global warming effect, Chemical Looping Combustion is known to be the most viable option currently. This method facilitates CO_2 capture by lower energy penalties compared with other methods in this category. The major challenges encountered in CLC are oxygen carrier, reactor and fuel-type selection. A proper combination of these factors is required for an efficient CLC. There have been several studies with regard to oxygen carriers applicable to these processes: novel oxygen carriers, single perovskites and potential oxygen carriers, double perovskites, have been investigated for their oxygen capture and release properties in a number of studies. Different kinds of reactors have also been proposed for use in CLC processes. Although there are several oxygen carriers and reactors with the desired function and efficiency for CLC, there remains the need for further improvement and optimization in both areas

A key factor to a successful chemical looping process is the presence of highly effective oxygen carriers that enable fuel combustion by going through oxidation and reduction in the presence of air and fuel respectively. Perovskites have proven to be great candidates for such purpose due to their special characteristics and their tunability. $CaMnO_{3-\delta}$ is a group of perovskites that has been studied to a great extent because of its high oxygen capacity (1.64%). Because of lack of stability in this structure, there have been plenty of efforts to stabilize the structure and increase its oxygen capacity. This study follows a method to achieve such purpose. The method was using $CaMnO_{3-\delta}$ as the base material and doping it on the A-site (Sr or La) and B-site (Fe, Ti, Zn and Al) by 10 mol % of dopants. Solid state reaction followed by mechanical extrusion was used as the preparation method. A proper formulation for the extrusion experiments was suggested. The main goal was to keep the slurry formulation simple to make it possible for further large-scale production of oxygen-carrier. The optimization was performed on the perovskite type $Ca_{0.9}La_{0.1}Mn_{0.9}Fe_{0.1}O_{3-\delta}$. The results showed that the starch amount in the paste composition has an optimum value. In our case this value was 1.2 wt. %. A series of novel

doped perovskite-type oxygen carrier particles (Ca_xLa (Or Sa)$_{1-x}$ $Mn_{1-y}B_yO_{3-\delta}$ (Bsite = Fe, Ti, Al, or Zr)) were synthesized by the proposed extrusion formula. The produced samples were characterized with XRD, SEM, BET and TGA techniques. The results showed that the proposed composition was suitable for other doping systems (B = Ti, Al, or Zr) as well and almost all the samples had the same surface area which was the main goal of the extrusion technique. In addition, all the samples were single phase and there was no evidence of any other second or residual phase among them. Based on TGA results, all single perovskite samples demonstrated store and release oxygen behaviors. According to the results obtained from TGA analysis, the oxygen capacity of the samples ranged between 1.2 for CLMZ and 1.75 for CSMF. Iodometric titration experiments were also conducted for evaluating the manganese ion charge and its variability in association with different doping elements.

Reactivity and oxygen uncoupling behaviors of the prepared samples were also evaluated using a fluidized bed chemical looping reactor using methane as the fuel at four different temperatures (800, 850, 900, 950 °C). All of the oxygen carriers showed oxygen uncoupling behavior and they were able to capture and release oxygen. Mass-based conversion of the perovskites was calculated and temperature increase proved to increase the mass-based conversion rate in all of the samples under study. Gas yield was calculated at 950 °C as well, and results showed that CLMZ, CM and CSMF showed 100% gas yields and CLMF and CSMZ showed approximately 85% yield in fluidized bed reactor, which is a high and acceptable quantity.

In the final step, extended chemical looping combustion was performed on two kinds of oxygen carriers.

500 g of $CaMnO_3$ (CM) and $Ca_{0.9}Sr_{0.1}Mn_{0.9}Fe_{0.1}O_3$ (CSMF) were synthesized by the previous reported technique. 30 g of each oxygen carrier with size distribution of 125−250 μm were used. The tests were carried out at 950 °C. The fuel reactivity was examined through a reaction with CH_4 gas (methane) and the CLOU (Chemical Looping with Oxygen Uncoupling) properties of the particles were investigated by measuring the oxygen release from the oxidized particles in nitrogen. The experiments were performed in a cyclic fashion, in which a period of oxidation was followed by a period of reduction, which constitutes one cycle, the experiment was repeated for minimum of 100-150 cycles. As the reactor had no cooling system and in order to avoid a large temperature increase during the combustion reaction, 8.5% O_2 concentration was utilized. The oxidation was conducted with stream containing 8.5 % O_2 and 91.5% N_2 with flow rate of

900 mLN min-1 (normalized to 1 bar and 25°C). The oxidation periods necessary for complete oxidation varied between 600 and 900s. N_2 was introduced for 45 s after each oxidation-reduction period to avoid the mixing of CH_4 and O_2. To avoid exceeding the terminal velocity of the particles due to the increase of the gas velocity produced during the CH_4 conversion, the fuel reduction was conducted with stream containing 18.8 vol % CH_4 and 81.2 vol % N_2 with flow rate of 1100 mLN min-1.The reduction period was 20 s. The tested samples were characterized before and after the long tests with XRD, SEM, BET and TGA analyses. XRD results revealed that the manganese-doped structure ($SrFe_{0.9}Mn_{0.1}O_{3-\delta}$) remained stable after extended runs, while the undoped sample of $CaMnO_3$ started decomposing to double perovskite structure after 150 cycles. Comparing SEM images of CM and CSMF before and after 150 cycles concluded that, while the size and porosity of CSMF particles did not show obvious change, the size of CM particles decreased and there were considerable amount of fine particles. TGA results before and after reactor tests also showed that the oxygen capacity of CM particles reduced by 1.5 %, while the oxygen capacity of CSMF carriers increased by 1.5%. The CH_4, O_2, And CO_2 profiles of each oxygen carrier during the 150 cycles confirmed that CSMF carriers resulted in complete combustion of methane after 100 cycles. On the other hand, the amount of uncombusted CH_4 increased by time in CM particles. This is supporting the fact that CM particles are decomposing over the time, whereas CSMF particles remained stable. Based on the new finding the modified calcium manganese perovskite structures can be a good candidate for future pilot tests.

Summary of perovskites used as oxygen carrier materials for CLC processes in the presented work

Perovskite	A-site doping elements	B-site doping elements	Methane conversion/%	Surface area/(m^2 g^{-1})	Synthesis method	Cost (1000$) per ton
Manganese-based perovskites	**La, Sr**	**Fe, Zr, Al, Ti**	**85-100**	**0.5-1**	**Solid Reaction**	**100-300**
Iron-based perovskites	**Sr**	**Mn**	**80-90**	**0.2-0.6**	**Solid Reaction**	**200-400**

1. Introduction

Global warming has become a serious challenge for humanity as it has caused climate patterns to fluctuate and the earth's surface air temperature to increase. There are several gases that contribute to climate change, such as H_2O, CO_2, CH_4, N_2O, CFC's and SF_6 [1]. Among these gases, CO_2 is the major contributor to global warming due to its long-term residence in the atmosphere and its high production rate from anthropogenic activities. Among these activities, the burning of fossil fuels contributes one third of CO_2 release [2]. The effect of global warming and its severe damage to the earth makes finding solutions to mitigate it necessary. In recent years, several approaches have been developed to overcome this problem, which is mostly due to CO_2 emissions from the burning of fossil fuels for power generation. One approach is the use of renewable resources to reduce CO_2 production in the first place, such as biofuels, wind, solar power, etc. However, technologies based on renewable resources are at their elementary stages of evolution, hence, at least in the near future they cannot represent viable options [3]. Another alternative is to reduce energy consumption by increasing the energy efficiency of current fuels; this, however, might not be practical in the near future. Another method is carbon capture and sequestration (CCS). There are currently a number of methods available for CO_2 capture, such as oxy-fuel combustion in which the fuel is in contact with pure oxygen instead of air [4, 5], post-combustion which is separation of the CO_2 from the fuel gas by chemical absorption using amines and other different methods including pre-combustion in which the fuel undergoes the de-carbonization process prior to entering the reactor [2, 6]. In these technologies, after capturing the CO_2, it will be pressurized to render it transferable to storage facilities. These techniques, besides their advantages, possess the major disadvantage of being energy-intensive, thereby rendering them poor candidates for further development [2]. A relatively new method of CO_2 capture, chemical looping combustion (CLC), has recently been introduced, which has attracted attention due to its ability to burn the fossil fuels for energy generation with CO_2 and water vapor as side-products (100 % CO_2 separation [7]). In this technology, the fuel is in contact with pure oxygen by means of oxygen carriers (OC; usually metal oxides) that are capable of capturing oxygen when they are in an atmosphere with high oxygen partial pressures and releasing it under low oxygen partial pressures. These OC materials are usually composed of transition metals and can be oxidized in air (which has a high oxygen partial pressure) and be reduced in contact with the fuel which consumes their captured oxygen. Subsequently, the OC materials again come in contact with air and the cycle continues.

The use of this technology will facilitate CO_2 separation by only using a condensation utility. It also eliminates the use of external energy-intensive utilities for CO_2 separation. Providing the ability for the fuel to be in contact with pure oxygen and not air results in eliminating NO_x as a by-product of the process.

Several review papers have been published on CLC-related fields. [8] reported on recent progress in oxygen carrier mechanism studies, their characterization and proper reactor design for CLC. [2] addressed recent advances in CLC by reporting on changes in oxygen carrier material and proposing Ni-based metal oxides as promising oxygen carriers in this field, requiring further improvement. They also recommend the reactor design to be two interconnected fluidized bed reactors. [7] provided information on recent progress in chemical looping with oxygen uncoupling (CLOU) and the oxygen carriers applicable to it (over 2008–2013). This study also discusses reactor design for CLOU. CLOU is similar to CLC in terms of efficiency and the products of the burning process but the mechanism by which the fuel is burnt is quite different. [1] collated information up to 2010 on progress in CLC and chemical looping reforming (CLR) of gaseous and solid fuels. They also gathered information on advances in metal oxides used in these technologies and process-modeling on different scales. Despite all the research and outstanding advances in this field, this technology has not yet been industrialized.

A promising CLC process requires effective and efficient oxygen carriers, which is a major concern in this field. In addition, proper reactor designs for different kinds of processes and fuels (liquid, solid, gaseous) are an important factor in CLC. This highlights the need for more research and understanding of the process, oxygen carriers and reactor design. The present review affords a full explanation of CLC processes and recent advances in the oxygen carrier materials used in these technologies.

Since metallic surfaces are able to catalyze carbonaceous fuel decomposition, metal oxides are used as oxygen carriers in CLC, to enable the fuel burning in the fuel tank to have a reducing atmosphere [9]. The application of several metal oxides to CLC has been studied. Ni-based oxygen carriers have been shown to have a high reactivity with carbonaceous fuels but tend to agglomerate after several oxidation and reduction cycles. They also show poor re-oxidation behavior. Fe-based materials have also attracted attention due to their low cost and favorable thermodynamics. However, after the alternation of oxidation and reduction reactions, cracks appear in their structure and cause fissure formation. Cu-based oxygen

carriers have been shown to be highly reactive with the fuel and can enable full conversion of the fuel. Their low cost also attracts attention. The downside of using this material is its decomposition at comparatively low temperatures. It also has a tendency to agglomerate because of its low melting point [2]. Ilmenite is composed of $FeTiO_3$ ($FeO \cdot TiO$) in which FeO is the active phase of the material that renders it suitable for CLC processes. In addition to its low cost, it has high reactivity with H_2 and moderate reactivity with CO and CH_4. In its highly reduced state, it can exhibit defluidization behavior. It can also be subject to structural changes after calcination [10, 11]. Using a combination of metal oxides in a single structure will facilitate the creation of good synergic effects, thereby combining the advantages of each material in a single material [9]. Recently there has been experimental research into special kinds of ceramics, perovskites and double perovskites as promising oxygen carriers in the near future due to their special characteristics. These ceramics are a combination of different metal oxides with different characteristics. A full description of these ceramics will be provided throughout the paper and there will also be a review of recent experimental research into reactor designs applicable to CLC technologies.

Chemical looping combustion

CLC, as shown schematically in Figure 1-1, is an approach to CO_2 capture without the need for external energy-intensive utilities. This process usually takes place in two interconnected fluidized beds, one being the air tank and the other the fuel tank. Oxygen carriers are oxidized in the air tank then transferred to the fuel tank to be reduced and make fuel-burning occur [12-14]. This allows the fuel to burn in pure oxygen and makes it possible to have CO_2 and water vapor as products. Two main reactions occur during oxidation and reduction cycles in the process:

$$2Me_xO_{y-1} + O_2 \rightarrow 2Me_xO_y + \text{air } (N_2 + \text{unreacted } O_2) \quad (1)$$

$$C_nH_{2m} + (2n+m)Me_xO_y \rightarrow (2n+m)Me_xO_{y-1} + nCO_2 + mH_2O \quad (2)$$

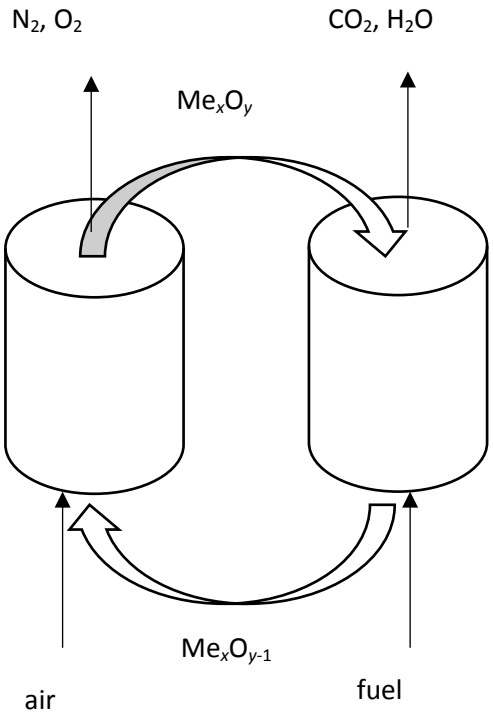

Figure 1-1 Schematic representation of two interconnected fluidized bed reactors for CLC, in which Me_xO_y and Me_xO_{y-1} are oxidized and reduced forms of oxygen carrier.

The reactions described by Eqs. (1) and (2) occur in the air tank and fuel tank, respectively. The oxidation reaction is exothermic but the reduction reaction in the fuel tank can be exothermic and endothermic depending on the type of fuel and oxygen carrier [13].

It is of great importance that, besides being energy-efficient, this process releases at least as much heat as normal combustion (summation of heat released in Eqs. (1) and (2) [15]. CLOU, on the other hand, has a different mechanism for burning the fuel. The oxidation and reduction cycles in CLOU are as follows:

$$2Me_xO_y \rightarrow 2Me_xO_{y-1} + \text{air } (N_2 + \text{unreacted } O_2) \quad (3)$$

$$C_nH_{2m} + (n + m/2)O_2 \rightarrow nCO_2 + mH_2O \quad (4)$$

In these reactions, the oxygen carrier will release gaseous oxygen to be in contact with the fuel and the reduced oxygen carrier will return to the air tank for re-oxidation. CLOU release at least as much heat as CLC but with a different fuel-oxidizing approach [7]. The use of CLOU is more efficient when using a solid fuel in the fuel tank [7, 16].

Solid, gaseous and liquid fuels can all be used in CLC technologies. However, gaseous fuels are more common since they have the least complicated mechanism for burning the fuel.

Liquid fuels are not common kinds of fuel in CLC and CLOU and there has been a limited amount of research in evaluating their functionality in an efficient CLC. These fuels can result in a high efficiency unit if they are injected directly into the fuel tank. Otherwise, evaporation will occur resulting in the formation of CO and H_2 prior to their being fully oxidized into water vapor and CO_2. If the fuel is injected directly into the fuel tank, evaporation and oxidation occur simultaneously and, as a result, CO_2 and water will be the reaction products. This process becomes more complicated for solid fuels. These fuels can be changed to a gaseous phase by using an external utility and undergoing CLC like gaseous fuels; however, this process is not economically favorable. Another option is to inject them into the fuel tank directly, resulting in fuel conversion to a solid charred part and a volatile part. The volatile part undergoes oxidation directly by direct contact with oxygen carriers. However, the char part by contact with steam and CO_2 produces CO and H_2 which can be the reactants of the oxidation reaction with CO_2 and water vapor as products. This approach can be time-consuming, especially with the char part of the solid fuel. It is also probable that the char exits the reactor without conversion to the desired products (this can happen when the fuel reactor is not large enough and consequently there is a short residence time for the char in the reactor) thereby decreasing the efficiency of the whole process. This process can be rapid if CLOU is used [7, 17, 18].

As stated above, the use of a good oxygen carrier is the key to an efficient CLC process. The oxygen carriers used in these systems should possess several qualities for the system to work efficiently. They must be reactive and stable and resistant to agglomeration. They should have high mechanical strength and be able to convert the fuel fully during the oxidation and redox cycles. These particles also should be non-toxic, economically viable and environmentally benign. Their melting temperature should also be a matter of concern [2, 13, 19]. Trial and error and heuristic methods have generally been used for producing oxygen carriers to date. However, current theoretical methods such as microkinetic modelling have also been introduced to facilitate the approach to oxygen carrier design. [20].

The following sections provide information on perovskites, double-perovskites and recent research into using them in CLC technologies and related fields.

Single perovskites

The general formula for an ideal perovskite structure is ABX_3 in which A and B are both cations, with A as a larger cation than B [21-23]. Transition metals will usually locate on the B-site, halides and oxides on the X-site and larger cations (such as Na^+, K^+, Ca^{2+}, Sr^{2+}, Ba^{2+}) will be located on the A-site [23, 24]. The perovskites that have usually been synthesized have the formula of ABO_3. The ideal, as shown in Figure 1-2, is a cubic crystal structure with octahedrons located at each edge of the cube. The atoms are located at the center of the cube. The B atoms are located at the corners of the cubic structure, located at the center of the octahedron. Oxygen atoms are also located at the 8 corners of the octahedron. They are important for their diverse chemical and physical characteristics over a wide temperature range [23]. Perovskite compounds can also be synthesized by doping the A and B-sites with different cations changing the formula to $A_{1-x}A'_xB_{1-x}B'_xO_3$. The substituted cations on the A-site and the B-site should have an appropriate charge and size for the structure to stay stable [25]. The properties of perovskite materials are highly dependent on their preparation method; as a result, several methods of synthesis have been introduced for perovskite production to date which strongly influence their surface physicochemical properties, surface area, porosity, purity and stability and crystal size [26, 27]. Of all the proposed techniques, the solid state reaction, the sol-gel method, the combustion method, mechanical-chemical processing, the Pechini method and the microwave route are the most common [28].

If the chemical structure of the cubic crystal changes, some oxygen vacancies might occur inside the crystal structure. Vacancy occurrence may be due to the partial substitution of the A and/or B-sites by a lower valence ion or the B-site ion reduction causing the formula to change to $A_xB_{-x}O_{3-\delta}$. Different materials can be doped on the B-site, each of which can have their own effect on the catalytic properties and oxygen absorption capacity of the oxygen carrier [29]. Due to the oxygen deficiency, these materials represent the ion conduction ability rendering them suitable candidates for CLC technologies [25, 30].

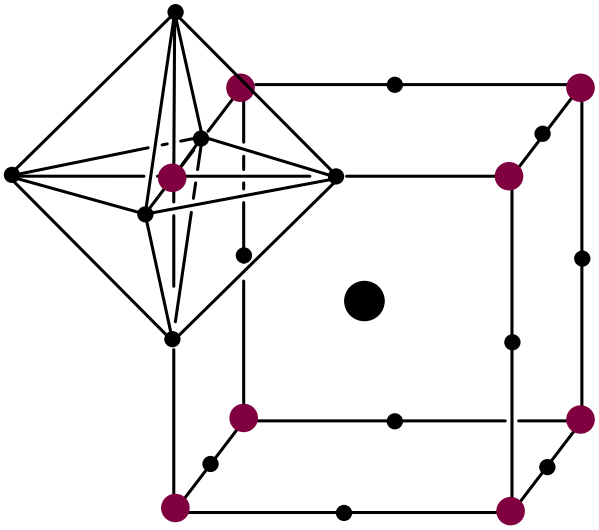

Figure 1-2 Ideal cubic perovskite structure; – A, – B, – C.

Perovskites in the air tank (air-flows through the air tank) capture oxygen, release the captured oxygen into the fuel tank and the released oxygen can be measured via Eq. (5).

$$ABO_{(3-\delta)A} \leftrightarrow ABO_{(3-\delta)F} + 1/2(\delta F - \delta A) \quad (5)$$

The term δ calculates the degree of oxygen non-stoichiometry. *A* and *F* refer to the air and the fuel tank, respectively, hence (δF–δA) represents the amount of gaseous oxygen released. Calculating the enthalpy of the oxidation/reduction of the perovskite can clarify the oxygen partial pressure at which δ starts to grow and for the number of oxygen atoms to start to deviate from 3. Oxygen non-stoichiometry can be calculated using coulometric titration and thermogravimetry [31]. In recent years, several studies have been conducted into synthesizing more efficient perovskites applicable to CLC as oxygen carriers [30]. A brief description of new research follows.

Iron and/or cobalt group

A family of perovskites with La at the A-site and Fe at the B-site were doped at the A and B-sites in various studies. $La_{1-x}Sr_xFeO_3$ (x = 0.1, 0.3, 0.5 and 0.9) are single perovskites that were investigated for methane partial oxidation using a fixed-bed reactor [32]. These materials were produced using the combustion method. Scanning electron microscope (SEM) images proved that this production method resulted in porous materials which increased the perovskites' oxygen capacity [32].The X-ray diffraction (XRD) results of fresh samples demonstrated monophasic crystalline structures (orthorhombic). These results also

demonstrated that, as the degree of Sr substitution increased, there would be more distinct peak shifts along the 2θ axis. As more La^{3+} is substituted by Sr^{2+}, more Fe^{3+} changes to Fe^{4+} and/or more oxygen vacancies are formed. As Fe^{4+} has a smaller ionic radius than Fe^{3+}, the XRD results are justified (in accordance with Bragg's law). Hence, as the results demonstrated, Sr substitution can increase the amount of oxygen vacancies in the perovskite structure. It was proved that this substitution had an optimal amount (x = 0.3–0.5). However, doping the A-site with Sr decreases the oxygen carrier's selectivity towards CO/H_2 and its reactivity with methane [32]. This perovskite structure was also examined in two-step steam-reforming of methane towards the simultaneous production of syngas and pure hydrogen and was shown to be a promising oxygen carrier [33]. Hydrogen can be produced as a by-product of chemical looping processes during the steam-reforming of carbonaceous fuels via the water-splitting reaction discussed extensively by [34].

$La_{0.8}Sr_{0.2}Fe_{0.9}Co_{0.1}O_3$ was also introduced as an oxygen carrier for methane partial oxidation to produce syngas. This perovskite structure was synthesized using the sol–gel method. Experiments were conducted in a fixed-bed quartz micro-reactor and resulted in an average methane conversion of 85 % and CO selectivity of 93.1 %. These materials exhibited the potential for use in methane partial oxidation. However, the XRD results demonstrated that the samples after several oxidation and reduction cycles did not have a perovskite structure. This observation showed a lack of structural stability for these perovskites over several consecutive oxidation and reduction cycles. Structural instability occurs when, at high temperatures and in a reductive atmosphere, the perovskite loses its lattice oxygen which results in structural collapse. The results demonstrated a notable increase in the oxygen carrier's activity after the B-site doping with Co (x = 0.1) [35]. Doping of the B-site with the equal amounts of Co and Fe resulted in having $La_{0.8}Sr_{0.2}Fe_{0.5}Co_{0.5}O_3$ as an oxygen carrier in the partial oxidation of methane. The citrate method was used for this material's synthesis. During experiments in a packed-bed reactor, it was observed that both chemical cracking and combustion occurred along with partial oxidation. However, this material exhibited high methane conversion (more than 85 %) and high selectivity towards H_2 and CO (over H_2O and CO_2) [36].

[9] proposed materials applicable to methane combustion (CLC) and methane partial oxidation to produce syngas ($La_xSr_{1-x}Fe_yCo_{1-y}O_{3-\delta}$). The study stated $La_{0.5}Sr_{0.5}Fe_{0.5}Co_{0.5}O_3$ (synthesized by the glycine nitrate combustion method and the spray drying method) to be a viable option for use in CLC. The results showed it to have high selectivity towards water

vapor and CO_2 production and high reactivity with methane. XRD analysis confirmed that this material maintained its perovskite structure. Samples without Co as a dopant were also investigated. It was shown that these materials underwent three stages, the first stage being combustion resulting in H_2O and CO_2 as products. The duration of this stage for $LaFeO_{3-\delta}$, $La_{0.8}Sr_{0.2}FeO_{3-\delta}$ and $La_{0.5}Sr_{0.5}FeO_{3-\delta}$ was shortest to longest, respectively. The second stage was the methane partial oxidation which is of interest for these materials, which exhibited high selectivity towards CO and H_2 without the formation of solid carbon. The final stage was solid carbon formation. These materials also exhibited the ability to maintain their perovskite structure. As stated previously they can be used in methane partial oxidation.

$La_xSr_xCo_{1-y}Fe_yO_{3-\delta}$ synthesized by the citric acid method was also investigated for its applicability to the CLC of natural gas. The in-situ powder XRD method was used to investigate the structural properties of perovskites during the reaction. The experiments revealed that structures with high amounts of Co exhibited decomposition to La_2O_3, cobalt metals and at least one unknown phase during reduction. However, $La_{0.8}Sr_{0.2}Co_{0.2}Fe_{0.8}O_{3-\delta}$ was revealed as a promising material with the appropriate amount of Co for CLC processes since it did not undergo structural changes during the oxidation and reduction cycles. This perovskite has a low oxygen capacity, hence a high-speed gas switching system is required [37]. A comparison between the above structures was also made [38]. $LaFeO_3$, $La_{0.8}Sr_{0.2}FeO_3$ and $La_{0.8}Sr_{0.2}Fe_{0.9}Co_{0.1}O_3$ (synthesized by the sol–gel method) was made in terms of methane partial oxidation activity. It was proven that A-site substitution or a combination of A and B-site substitutions resulted in an increase in catalytic activity and oxygen availability of the structures during the reduction period, as previously concluded. However, A and B-site doping decreased selectivity towards CO. $La_{0.8}Sr_{0.2}Fe_{0.9}Co_{0.1}O_3$ showed less structural stability during reduction than the other two perovskite oxides because of Co as a B-site dopant [38]. The reactivity and performance of $La_{0.6}Sr_{0.4}Co_{0.2}Fe_{0.8}O_3$, $La_{0.7}Sr_{0.3}FeO_3$, co-precipitated iron oxide (60 %; Fe_2O_3/Al_2O_3) and supported nickel oxide (20 %; NiO/Al_2O_3) were also evaluated and compared in the chemical looping water-gas shift process. A decline in H_2 production and carbon deposition for co-precipitated iron oxide and supported nickel oxide was observed. $La_{0.7}Sr_{0.3}FeO_3$ was shown to have the best performance over a large number of cycles[39].

A three-dimensionally ordered macro porous perovskite was also investigated and compared with a simple single perovskite [40]. $LaFeO_3$ nano-powder was compared to three-dimensionally ordered macroporous $LaFeO_3$ (Three-dimensional ordered macroporous-

3DOM) perovskites. These perovskites were prepared using the polystyrene colloidal crystal-templating method and were proven to exhibit more stability towards the production of CO and H_2 in the methane reaction. Overall, 3DOM was presented as a better catalyst and oxygen carrier in the chemical looping reforming of methane [40].

[41] took a more general approach to investigating these materials by including Ni, Cr and Cu in addition to the Co-doped materials previously investigated, resulting in $La_{1-x}Sr_xM_yFe_{1-y}O_3$ (M = Ni, Co, Cr, Cu). These materials were used for syngas generation from methane, and the citrate method was used as the production method. No impurities or unreacted species were identified in the course of the experiments. The results reveal that the addition of a small amount of NiO by mechanical mixing (Ni cannot be incorporated into the structure) leads to increased reactivity and selectivity of the particles towards CO and H_2. All samples were shown as good for use in methane partial oxidation. However, the best performance was observed for $La_{0.7}Sr_{0.3}Cr_{0.05}Fe_{0.95}O_3$ associated with 5 % NiO which resulted in H_2 yields of up to 90 % and good stability. $LaCoO_3$ perovskite was doped with Cu ($LaCo_{0.8}Cu_{0.2}O_3$) by [42]. These materials were produced by a polymerizable complex route and were investigated for methane partial oxidation. The results proved the existence of a single phase for both perovskites, which means that no additional or undesired phase was formed. High activity to syngas was observed for $LaCoO_3$ but a considerable amount of carbon deposition occurred during the reaction, which might result in catalyst deactivation. By copper substitution on the B-site, the structure acquired the ability to be resistant to carbon deposition. An increase in reducibility and decrease in temperature to produce syngas were other results of copper substitution.

[43] presented $La_{1-x}Sr_xMnO_3$ (x = 0, 0.3, 0.7) perovskite as a candidate for use in the steam-reforming of methane. XRD results confirmed the presence of minor traces of a tetragonal phase, identified as Sr_2MnO_4 which became clearer as the amount of doped Sr was increased in the perovskite. This additional unwanted phase was in negligible amounts which did not affect the material's functionality. This material resulted in 70 % of water conversion at 1273 K and no coke was formed.

In another study by [44], instead of a fraction of La and Sr on the A-site, Sr was used as the A-site cation and Fe and Cu were the B-site cations. $SrFe_{1-x}Cu_xO_{3-n}$ was synthesized by sintering the raw material at 700 ^oC for 20 h. Thermogravimetric analysis (TGA) experiments

on these samples revealed their high oxygen mobility. The results also showed an increase in the oxygen mobility with increasing the Cu content in the structure.

Cerium group

$La_{1-x}Ce_xBO_3$ (B = Co, Mn) are another family of perovskites whose oxygen capture and release abilities were investigated in CLC. $LaCoO_3$ and $LaMnO_3$ perovskites were prepared using the reactive grinding method (LaCeCo-RG) [45]. $LaMnO_3$ was also produced using the nanocasting method (LaCeCo-NC). These methods are preferable since preparing samples by these methods gives the structure a higher specific surface area and higher oxygen mobility. All the perovskites exhibited the desired functionality during the oxidation and reduction cycles. However, $LaMnO_3$ appeared to have higher reducibility and higher surface oxygen (α-O_2) and these characteristics were more marked when the nanocasting method was used. Doping the A-site with Ce did not affect the oxygen capacity proportional to the increase in surface area of the structure [45]. [46] introduced CeO_2-promoted $LaMnO_3$ perovskites as oxygen carriers. These perovskites were synthesized using the co-precipitation method and the experiments were conducted using a steady-state fixed-bed reactor. The XRD results showed $LaMnO_3$ as having an orthorhombic structure and CeO_2 an cubic structure, meaning that not all the CeO_2 used was incorporated in the perovskite structure. The XRD results also revealed the stability of these structures after four oxidation and reduction cycles (each cycle of approximately 40 min). Some slight morphological changes were observed using SEM analysis but these changes did not affect the structure and efficiency of these perovskites. Reactor tests showed a high methane conversion in the first 10 minutes of each cycle and no syngas was detected during the first cycle. As the cycle number increased, the amount of syngas production increased, indicating less surface oxygen at the surface of the structure resulting in lattice oxygen release and, consequently, methane partial oxidation. CeO_2 clearly had an effect on the perovskite function in this set of experiments [46] (in contrast with the previous article [45]). This might be due to differences in the synthesizing methods.

Nickel group

$LaNiO_3$ was doped with zinc to produce $LaNi_{1-x}Zn_xO_3$ (x = 0.2, 0.4, 0.6, 0.8, 1) by [47]. These materials were used in the methane partial oxidation process and were produced using the sol–gel related method. The experiments demonstrated an enhancement in the conversion rate, stability and carbon deposition resistivity. The amount of substituted Zn was

also investigated and it was shown that, for $x \leq 0.4$, the material was highly active. However, it showed a decreased conversion (lower than 20 %) for $x \geq 0.6$. $x = 0.2$ was an optimal amount for this perovskite since $LaNi_{0.8}Zn_{0.2}O_3$ showed the highest reactivity with methane but Zn substitution resulted in a more difficult reduction reaction for the structure.

Manganese group

The $CaMnO_3$ perovskite structure was investigated in the literature [48, 49]. The investigations revealed this material as able to release and capture oxygen at oxygen partial pressures of 1–100 kPa. This phenomenon occurs due to the transformation of Mn^{4+} to Mn^{3+} thereby facilitating the oxygen release in the fuel tank. However, this structure is subject to change to Ca_2MnO_4 and $CaMn_2O_4$ which might cause a decrease in the perovskite efficiency during oxidation reduction cycles at high temperatures. According to the literature, to resolve this problem, transition metals such as Ti, Fe, Zr and Cu can be doped with the B-site cation (Mn), leading to a more stable structure during the process. $CaMn_{1-x}Ti_xO_3$ was proposed as applicable to CLOU. This material was synthesized using spray pyrolysis and the experiments were conducted using both TGA analysis and a fluidized-bed reactor. An optimal amount of Ti was detected with the most efficient perovskite structure as being 0.125 ($CaMn_{0.875}Ti_{0.125}O_3$). In this set of experiments, gaseous (methane) and solid (petroleum coke) fuels were used. Ti-substitution was revealed to be beneficial to the $CaMnO_3$ perovskite structure, since it exhibited no CO formation even in dry methane. Experiments involving both TGA and a fluidized bed showed this oxygen carrier to be a promising applicant for use in CLC processes. This material also proved to be stable over numerous oxidation−reduction cycles [50]. This perovskite was also investigated in the CLC and CLOU of natural gas. It was concluded from XRD analysis that the particles maintained most of their physical properties and underwent some compositional changes (formation of $CaMn_2O_4$). No coke formation was observed during the experiments. Ca is susceptible to poisoning by sulfur which results in the perovskite structure breaking up and, other problems occurring which are undesirable in an efficient CLC process [51].

A more general experiment was carried out by [29] evaluating $CaMn_{1-x}M_xO_{3-\delta}$ (M = Ti, Fe, Mg) using a batch fluidized-bed reactor. The particles were synthesized using spray-drying and all exhibited a significant O_2 release and good reactivity with methane and syngas. However, an undesired phase ($CaMn_2O_4$) was observed for every single one of these perovskites, albeit not affecting their efficiency. Fe and Ti were shown to be incorporated into

the perovskite structure. However, this was not the case for Mg, since a separate phase of MgO was observed. The structure doped with MgO exhibited the best fuel conversion, superseding the strength and fluidization behavior of all. The XRD results also endorsed this observation, showing MgO as a separate phase, not incorporated into the structure, which is due to its small ionic radius. They suggested that MgO had better properties than Ti- and Fe-doped manganese oxides, stating that "MgO might be an active component in the oxidation reaction with methane, for instance, it may have a role as reforming catalyst on the particle exterior." Further experiments are needed to understand the effect of this separate phase [52-54].

In addition to Ti, Fe and Mg as B-site dopants, [55] also investigated Cu as a B-site dopant and La as an A-site dopant for oxygen carriers used in CLOU. $Ca_xLa_{1-x}Mn_{1-y}M_yO_{3-\delta}$ (M = Mg, Ti, Fe, Cu), using mechanical homogenization followed by extrusion as the method of synthesis, were characterized and examined (using a laboratory-scale fluidized-bed reactor) for possible applications to CLOU. Methane, synthesis gas and devolatilized wood char were used as fuels. As observed in other articles, perovskites doped with Mg, Ti and Fe exhibited promising features for use in CLOU, such as high reactivity, high oxygen release, almost complete gas yields, stability and no agglomeration. However, the Cu-doped perovskite exhibited defluidization behavior while in contact with methane; hence a complete gas yield was not achieved. On the other hand, while using synthesis gas as fuel, all the synthesized particles achieved a complete gas yield. Devolatized wood char was also used for measuring their oxygen release rate and all of them exhibited a reasonable amount of oxygen release during reduction.

[56] investigated a new perovskite oxide with the formula $SrMn_{1-x}Ni_xO_3$ (x = 0, 0.2, 0.5, 0.8, 1). These materials were used for hydrogen CLC and were synthesized using mechanical mixing. They were shown as maintaining their physicochemical properties, with no tendency for agglomeration. They were also proved to have a high melting point (higher than 1100) rendering them interesting candidates for the desired application. $SrNiO_3$ and $SrMnO_3$ had the highest and lowest oxygen capacities, respectively, with all the other perovskites with different amounts of nickel between these values. Since nickel is a toxic substance, decreasing its amount in the production process results in less environmental damage. However, since it has a high reductive capability, an optimal amount should be used. [57] previously investigated this material and reported its applicability to the CLC of fuels.

Table 1-1 summarizes single perovskite materials investigated as suitable oxygen carriers in the literature, to date.

As this brief introduction to recent research on perovskites in CLC presents, there is a growing interest in the use of perovskite structures as oxygen carriers in the scientific community. Selecting the most suitable oxygen carrier for the system in use might be a difficult task since many competing factors can influence the final choice of perovskite material such as cost, availability, environmental considerations, etc. It is obvious that, among all the perovskites investigated so far, a good fuel (mostly methane) conversion was achieved, but the process conditions and oxygen carriers need to be even further optimized. Sr substitution on the A-site of the perovskite with the general formula of $LaFeO_3$ resulted in a higher oxygen vacancy concentration and lower reactivity with the fuel during the process. The effect of the B-site dopant was also investigated using an optimal amount (differing in each case) of Co for reactivity enhancements. In some cases, metal could not be incorporated into the structure (NiO, MgO, and CeO_2) and, in these cases, an efficiency improvement was observed. In the case of CeO_2, some of it was incorporated into the structure and some was recognized as a separate phase by using XRD mainly. In addition to La as a major A-site material, Ca was also investigated as an A-site material. Besides its sensitivity to sculpture which may cause oxygen carrier deactivation, it was demonstrated as a viable option for CLC purposes.

$CaMnO_3$ was doped at both A- and B-sites in different cases to avoid its compositional changes under reaction conditions at high temperatures [50]. The B-site was doped with Mg, Ti, Fe and Cu and the A-site with La. All the synthesized oxygen carriers exhibited oxygen capture and release in oxidative and reductive atmospheres. Some are more suitable for methane partial oxidation for syngas production and some are better suited for chemical looping combustion. It was shown that, as Sr-doping in the structure increases, the oxygen carrier becomes more capable of functioning at chemical looping combustion. In most cases, methane was used as the fuel. The literature contains many synthesis methods, among which the most common are spray-pyrolysis, spray-drying, reactive grinding and citrate method.

Table 1-1 Summary of perovskites used as oxygen carrier materials for CLC processes

Perovskite	Advantages	Disadvantages	Methane conversion/%	Particle size/mesh	Surface area/(m^2 g^{-1})	Synthesis method
Iron and/or cobalt group						
$La_{1-x}Sr_xFeO_3$ (x = 0.3–0.5)	high oxygen capacity by Sr substitution	Sr substitution results in low reactivity with methane	100	80–100	≈ 11.495	combustion method
$La_{0.8}Sr_{0.2}Fe_{0.9}Co_{0.1}O_3$	Co-doping resulted in increased oxygen activity with methane	lack of structural stability during red-ox cycles	≈ 85	40–80	–	sol–gel method
$La_{0.8}Sr_{0.2}Fe_{0.5}Co_{0.5}O_3$	–	–	> 98	270–1250	< 1	citrate method
$La_{0.5}Sr_{0.5}Fe_{0.5}Co_{0.5}O_{3-\delta}$	stability after several red–ox cycles	no proven advantage over other potential metal oxides	95	–	–	glycine–nitrate combustion method and spray-drying

$La_{0.8}Sr_{0.2}Co_{0.2}Fe_{0.8}O_{3-\delta}$	structural stability	low oxygen capacity	–	–	–	citric acid method
$La_{0.7}Sr_{0.3}Cr_{0.1}Fe_{0.9}O_3$ + 5 % NiO	structural stability	–	≈ 95	–	< 5	citrate method
$LaCo_{0.8}Cu_{0.2}O_3$	carbon deposition resistant, higher reducibility and lower reaction temperature than $LaCoO_3$	lack of structural stability	≈ 56	55.6[a]	< 10	polymerizable complex route
$La_{1-x}Sr_xMnO_3$ (x = 0, 0.3, 0.7)	no coke formation, stable behavior, high activity level achieved	not energy efficient	≈ 90	–	< 2	metal precursor dilution
$Sr(Fe_{1-x}Cu_x)O_{3-n}$ (x = 0–1)	high O_2 transport ability, high melting temperature and low agglomeration tendency	–	–	18–400	–	sintering
Cerium group						

$La_{1-x}Ce_xBO_3$ (B = Co, Mn)	structural stability	Ce substitution had no effect on OC performance; some limited agglomeration observed	≈ 80	–	LaCo/Ce-RG: 550 LaMn-RG/NC: ~625/LaCo/Ce-RG: 30.5 LaMn-RG/NC: 42.5	reactive grinding method and nano-casting
CeO_2 promoted $LaMnO_3$	structural stability	slight morphological changes, substantial decrease in methane conversion after 10 min	< 100	–	–	co-precipitation method
Nickel group						
$LaNi_{0.8}Zn_{0.2}O_3$	higher activity, stability and less coke formation than $LaNiO_3$	more difficult reduction process	≈ 90	30–60	–	sol–gel related method
Manganese group						
$CaMn_{0.875}Ti_{0.125}O_3$	no coke formation, stable, good fluidization properties, ability to oxidize at low	possible particle dissolution, forming $CaMn_2O_4$, sensitive to sulfur poisoning	≈ 85	≈ 120–170	–	spray pyrolysis

	O_2 partial pressures					
$CaMn_{1-x}M_xO_{3-\delta}$ (M = Ti, Fe, Mg)	good fluidization (Mg-doped- best out of three)	small amounts of $CaMn_2O_4$ as impurity	≈ 90 (achieved full conversion)	≈ 70–80	–	spray-drying
$Ca_xLa_{1-x}Mn_{1-y}M_y$ (M = Mg, Ti, Fe, Cu)	high reactivity, high oxygen release, stability, no agglomeration	defluidization properties (Cu-doped)	≈ 100	≈ 325	≈ 0.32	mechanical homogenisation followed by extrusion
$SrMn_{1-x}Ni_xO_3$	high stability, no agglomeration tendency	toxic properties of Ni	–	> 60	≈ 2	mechanical mixing

a) In nm.

Double perovskites

As stated above, perovskites are materials that, due to their special properties, have applications to CLC and CLOU processes. These materials have the general formula of ABO_3. Another group of perovskite oxides with more variation than single perovskites are known as double-perovskites, as shown in Figure 1-3. Their formula is $A_2BB'O_6$[58] and they have been proposed as suitable candidates for CLC processes due to their ability to rapidly store and release oxygen. Within their structure, the B sub-lattice is occupied by two different B and B′ cations. If the alteration in the ionic radii or the charges between both B and B′ cations is large enough, they become ordered in a perovskite superstructure. In this way, they have larger unit-cell parameters than a primitive perovskite cell, a 0–4 Å. When the ordering of B and B′ is established, a rock-salt sub-structure is detected at the B sub-lattice. The superstructure will be face-centered cubic for large A cations, and it can be described in the Fd-3m space group (s.g.). The advanced tilt of the BO_6 and $B'O_6$ octahedral takes place for smaller A cations, This leads to further distortion of the superstructure, with tetragonal symmetry (s.g. I4/m) or even monoclinic symmetry (s.g. P21/n). In perfectly ordered double perovskites, a three-dimensional array of B–O–B′ linkages can be detected. From the catalytic perspective, this specific arrangement of alternating different B cations can attract great interest, as the nature, oxidation states and relative arrangement of the B-site cations of perovskites determine their catalyst activity [59].

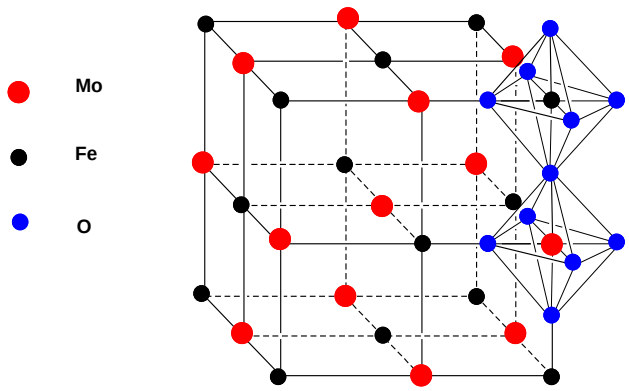

Figure 1-3 Schematic representation of crystallographic structure of double perovskite with general formula of A2BB′O6; – Mo, – Fe, – O.

In ordered double perovskites, denoted as $A_2BB'O_6$ (A = alkaline-earth or rare-earth element ion (Ba, Sr, Ca), B (Mg, Ca, Co, Ni, Cu, Cd) and B′ is the transition metal ion), the differences in the valence and size between the B and B′ cations are crucial for controlling the physical properties [60]. Accordingly, the electrical and magnetic properties of the compounds are highly dependent on the valence pair (B, B′) [61].

$(AA')–(BB')O_6$ are compounds which have cubic perovskite structures. In these compounds, A and A′, which are the larger cations, can be incorporated into the perovskite structure at cation sites at random surrounded by 12 oxygen ions. B and B′ in this structure, on the other hand, can be incorporated in both a random and an orderly manner in cation sites sieged by six oxygen ions in an octahedral [62]. The ability of these materials to store and release oxygen stems from the fact that the cations in these materials can vary in their oxidation state, thereby allowing the oxygen stoichiometry to vary. Altering the cation composition in these materials affords optimization of both the amount of oxygen stored and the storage/release kinetics. However, in the last decade only a few works exploring the double perovskite material from this perspective have been reported.

The solid oxide fuel cell (SOFC) is an electrochemical energy-conversion device which converts stored chemical energy in a fuel to electrical energy with low levels of pollution. It consists of a cathode, an anode and an electrolyte in between (Figure 1-4).

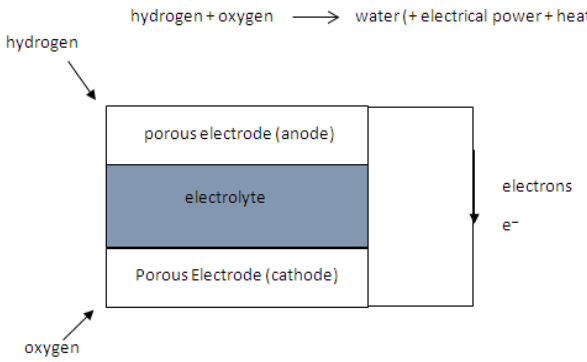

Figure 1-4 Solid oxide fuel cell [63].

Air passes over the cathode material. This material captures oxygen and releases it in the cell to be transferred to the anode. As a result, it is important for an efficient and functional solid oxide fuel cell to be constructed of materials that are capable of oxygen capture and release. As a result, double perovskites can be candidates of interest for use as both anode and cathode materials in SOFCs.

Double perovskites referred to in the literature that have exhibited the ability to rapidly store and release oxygen are classified in Table 1-2 based on their main metal on the B-site. The majority of double perovskite structures included in the literature were investigated in SOFC applications.

The table indicates five groups to date, denoted as follows: (i) AMo, (ii) ACo, (iii) AMn, (iv) mixed (a combination of (i) and (iii)), (v) (not allocated to other groups).

AMo double perovskites

$Sr_2FeMoO_{6-\delta}$ was investigated by [64] as a potential oxygen carrier for methane combustion. The results demonstrated this system's ability to incorporate oxygen into the structure and the existence of oxygen vacancies throughout the structure. The material was shown to have a double perovskite structure using wet chemistry procedures for production. $Sr_2FeMoO_{6-\delta}$ can also be a mixed ionic and electronic conductor due to the Fe^{3+}/Fe^{2+} valence and the Mo^{6+}/ Mo^{5+} valence. There is an equilibrium reaction in this double perovskite structure which affords electronic conductivity. This characteristic renders the structure a good candidate as cathode material in SOFCs.

Co-doped $Sr_2FeMoO_{6-\delta}$ was also examined for its applicability to SOFCs. The doped structure was shown to have enhanced electrochemical activity as cathode for the desired application. This material was synthesized using the glycine-nitrate combustion process and the results indicated that the conductivity of the cathode in SOFC increased with the Co content, implying that Co-doping can increase the oxygen vacancy concentration [65].

$Sr_2Mg_{1-x}Fe_xMoO_{6-\delta}$ was examined for methane oxidation catalysis by [62]. The catalytic properties of this perovskite structure were strongly affected by Fe substitution. The highest activity was observed for $x = 0.8$ ($Sr_2Mg_{0.2}Fe_{0.8}MoO_{6-\delta}$). Having Fe in the structure, due to the possible existence of (Fe^{2+}, Mo^{6+}) and (Fe^{3+}, Mo^{5+}) valence pairs, the results at higher activity compared with those of the structure without iron. This material was synthesised using the citrate sol–gel method and the results indicated good catalytic properties for methane combustion. The valence pairs referred to above play an effective role in activating gaseous oxygen and the existence of higher oxygen vacancy concentrations in the double perovskite structure. It is claimed that the surface lattice oxygen molecules are responsible for the combustion of methane and that the active surface lattice oxygen species

play a role in catalytic performance which is also related to the Fe composition doped in the structure.

[66] reported $Sr_2Mg_{1-x}Mn_xMoO_{6-\delta}$ as an appropriate anode material for SOFCs while using natural gas as the fuel at operating temperatures ranging from 650 °C to 1000 °C. This double perovskite structure exhibited long-term stability with a tolerance to sulfur and a superior single-cell performance in hydrogen and methane.

Sr_2MMoO_6 (M = Mg, Mn) double perovskites have recently been proposed as an anode material in SOFC. The thermal evolution of the crystal structure of Sr_2MMoO_6 (M = Mg, Mn) under the actual working conditions of an anode in an SOFC from "in situ" neutron powder diffraction (NPD) experiments, in tandem with thermal expansion measurements under a reducing atmosphere, were investigated. This material showed promising applicability as an anode material to SOFCs [59].

$Sr_{2-x}Sm_xMgMoO_{6-\delta}$ with x ranging from 0 to 0.8 is a double perovskite which was investigated as an anode substance in SOFCs. Experiments were carried out using $La_{0.9}Sr_{0.1}Ga_{0.8}Mg_{0.2}O_{3-\delta}$ (LSGM) as electrolyte and the results demonstrated that x ranging from 0 to 0.4 produced a single-phase double perovskite. However, at x = 0.6 or more, some impurities such as $SrMoO_4$ and Sm_2O_3 were observed. It was shown that the substitution of Sm for Sr had a notable effect on increasing electrical conductivity. The power densities of single cells achieved with x = 0, 0.2 0.4, 0.6 and 0.8 anodes on a 300 µm thick on LSGM electrolyte were 633 mW cm^{-2}, 770 mW cm^{-2}, 860 mW cm^{-2}, 907 mW cm^{-2} and 672 mW cm^{-2}, respectively, in H_2 at 850 °C. The experiments showed x = 0.4 to be the best anode candidate [67].

Double perovskites of the general formula of Ba_2MMoO_6, prepared using the sol–gel method, were investigated as alternative anode materials for SOFCs,. Under a reducing atmosphere, BFMO, BCMO and BMMO were stable but BNMO decomposed to other substances. All the Ba_2MMoO_6 samples exhibited the ability to lose a limited amount of oxygen in a reducing atmosphere. BFMO, BCMO, BMMO and BNMO showed the highest to lowest power outputs. The different performances for these perovskites were related to their differences in conductivity and oxygen vacancy [68]. BFMO was also confirmed as being suited for use in methane oxidation as a catalyst [64]. $A_2FeMoO_{6-\delta}$ (A = Ca, Sr, Ba) was reported as a viable material for use as an anode in SOFC and as a catalyst for methane oxidation. These materials were prepared by solid-state reactions and they can adopt

monoclinic, tetragonal and cubic structures at ambient temperature. $Ca_2FeMoO_{6-\delta}$ had a low oxygen vacancy concentration and showed the least stability (decomposition) at high temperatures, rendering it a poor candidate as catalyst in methane oxidation and as anode material. $Sr_2FeMoO_{6-\delta}$ exhibited the highest electrochemical performance, being higher than $Ba_2FeMoO_{6-\delta}$, being higher than $Ca_2FeMoO_{6-\delta}$. $Sr_2FeMoO_{6-\delta}$ in particular exhibited a high electrical conductivity, good thermal stability and excellent electrochemical performance, making it the best (out of the other two perovskites) candidate for SOFCs and methane oxidation [64, 69].

ACo double perovskites

Zhou et al. (2008) represented $SmBaCo_2O_{5+\delta}$ (SBCO) which has double perovskite structure as a good candidate for use in cathodes in SOFCs. The XRD results demonstrated the SBCO cathode to be chemically compatible with SDC and LSGM as electrolytes. The maximal power densities for SDC and LSGM electrolytes associated with SBCO as cathode material achieved 641 mW cm^{-2} and 777 mW cm^{-2} at 800 °C, respectively. The experiments showed this double perovskite material to be a promising material for use in SOFCs [70]. $SmBaCuCoO_{5+\delta}$ is a double perovskite and was investigated for its applicability to SOFCs, using $BaCe_{0.7}Zr_{0.1}Y_{0.2}O_{3-\delta}$ as electrolyte. $SmBaCuCoO_{5+\delta}$ has a better thermal expansion coefficent than $SmBaCo_2O_{5+\delta}$. Humidified hydrogen was used as the fuel in this process and the results demonstrated $SmBaCuCoO_{5+\delta}$ to be a potential candidate for proton conduction in SOFCs [71].

[72] examined a new double perovskite as cathode material in SOFCs. Ln $BaCoFeO_{5+\delta}$ (Ln = Pr, Nd) has attracted attention in recent years due to its special characteristics. It forms a mixed ionic-electronic conductor and it has high oxygen permeation, thereby rendering it an excellent electrochemically active substance. This material has been shown to have high oxygen diffusion and high oxygen surface kinetics. Despite its advantages, Ln $BaCoFeO_{5+\delta}$ has a high thermal expansion coefficient, its inherent cobalt element is expensive and it exhibits poor long-term chemical stability. It was synthesized using the ethylenediaminetetraacetic acid (EDTA)-citrate complexing method. The results have shown PBCF to have a higher power density than NBCF.

AMn double perovskite

Tao and Irvine [73] reported a perovskite $La_{0.75}Sr_{0.25}Cr_{0.5}Mn_{0.5}O_{3-\delta}$ (LSCM) and used it as anode material. The experiments were conducted using methane and the results showed a desirable performance from this perovskite structure for methane oxidation with no excess steam requirement. However, this material exhibited a low electronic conductivity under a reducing atmosphere. It was also noted that the structure exhibited low stability in fuels containing 10 % of H_2S. [65].

Mixed double perovskite

Another double perovskite introduced as an anode material for SOFCs is $Sr_2MMoO_{6-\delta}$ (M = Co, Ni) [74]. The samples were synthesized using the sol–gel method and both had limited concentrations of oxygen vacancies in reducing atmosphere in anode. Using an anode of 300 µm in thickness with $La_{0.8}Sr_{0.2}Ga_{0.83}Mg_{0.17}O_{2.85}$ as electrolyte and $SrFe_{0.2}Co_{0.8}O_{3-\delta}$ as cathode, Sr_2CoMoO_6 had the maximum power density for H_2 and wet CH_4 at 800 °C, while Sr_2NiMoO_6 exhibited a high power output only in dry CH_4. The stronger octahedral site preference of Ni^{2+} over Co^{2+} can be the reason for the lower performance of M = Ni as anode material [74]. The double perovskite $LaCaMnCoO_6$, was of interest as a sequential methane-coupling catalyst due to its unique structure and redox properties. The material was reported to have an ordered perovskite structure exhibiting multiple occupations of both A (La and Ca) and B (Mn and Co) sub-lattices [75, 76].

Other double perovskites

The double perovskite La_2CuNiO_6 was examined for methane catalytic combustion. This perovskite was synthesized using the sol-gel method and exhibited enhanced catalytic activity over a mixture of 1 : 1 ratio single perovskites $LaNiO_3$ and $LaCuO_3$. The combustion of methane was carried out in a conventional flow system under atmospheric pressure. The only products detected from the outlet stream were carbon dioxide and negligible amounts of carbon monoxide during the methane oxidation process [58].

$PrBaCo_{2/3}Fe_{2/3}Cu_{2/3}O_{5+\delta}$ (PBCFC) has been shown to be a potential double perovskite as a cathode material in SOFC applications. This material was synthesized using the EDTA-citrate complexing method. This material exhibits good chemical compatibility with $Ce_{0.8}Sm_{0.2}O_{1.9}$ (SDC) and $Ce_{0.9}Gd_{0.1}O_{1.95}$ (GDC) as electrolytes. XPS analysis demonstrated that rare earth and transition metal cations existed in two different valence states, Pr^{3+}/Pr^{4+}, Co^{3+}/Co^{4+}, Fe^{3+}/Fe^{4+} and Cu^{+}/Cu^{2+}. The maximal power densities using PBCFC as cathode

and GDC as electrolyte achieved 659 mW cm^{-2} and 512 mW cm^{-2} at 800 °C and 750 °C, respectively. The results revealed that PBCFC had the potential to act as cathode in the presence of GDC as electrolyte in SOFC applications [77].

Perovskite	Formula	Properties	Particle size/mesh	Surface area/(M^2 g^{-1})	Reference
AMo					
AFM	$A_2FeMoO_{6-\delta}$ (A = Ca, Sr, Ba)	good catalytic activity for methane oxidation	30–40	7.6	[64]
SFCM	$Sr_2Fe_{1.5-x}Co_xMo_{0.5}O_6$ (x = 0, 0.5, 1)	material for direct electrochemical combustion of CH_4	–	–	[65]
SMFM	$Sr_2Mg_{1-x}Fe_xMoO_{6-\delta}$	catalytic oxidation of methane	–	–	[62]
SMMM	$Sr_2Mg_{1-x}Mn_xMoO_{6-\delta}$	proposed as anode materials in SOFC	–	–	[66]
SMM	Sr_2MMoO_6 (M = Mg, Mn)	proposed as anode materials in SOFC performance in methane combustion	–	–	[59]
SSMM	$Sr_{2-x}Sm_xMgMoO_{6-\delta}$	SOFC anodes	4800–12000	–	[67]
BMM	Ba_2MMoO_6 (M = Fe, Co, Mn, Ni)	Ba_2FeMoO_6 exhibits the best electrochemical performance and catalytic activity for methane oxidation	–	–	[68]
AFM	$A_2FeMoO_{6-\delta}$ (A = Ca, Sr, Ba)	anodes for solid-oxide fuel cells	CFM (1250–2500), SFM (5000–12000), BFM (2500–	–	[69]

		4800)			
ACo					
SBC	$SmBaCo_2O_{5+\delta}$	cathode material for intermediate-temperature solid-oxide fuel cells	–	–	[70]
SBCC	$SmBaCuCoO_{5+\delta}$	cathode for proton-conducting solid-oxide fuel cells	–	–	[71]
PBCF, NBCF	$LnBaCoFeO_{5+\delta}$ (Ln = Pr and Nd)	intermediate-temperature solid-oxide fuel cell cathode	–	–	[72]
AMn					
LSCM	$La_{0.75}Sr_{0.25}Cr_{0.5}Mn_{0.5}O_{3-\delta}$	very good performance achieved for CH_4 oxidation	> 12000	–	[73]
mixed					
SMM	Sr_2MMoO_6 (M = Co, Ni)	proposed as anode materials in solid-oxide fuel cells (SOFC)	–	–	[74]
LCMC	$LaCaMnCoO_6$	sequential (redox) mode methane-coupling catalyst	–	–	[75, 76]

others

LCN	La_2CuNiO_6	ferromagnetic behavior, excellent methane catalytic combustion activity	–	–	[58]
PBCFC	$PrBaCo_{2/3}Fe_{2/3}Cu_{2/3}O_{5+\delta}$	intermediate-temperature solid- oxide fuel cell cathode	4800–12000	–	[77]

A summary of double perovskites is provided in Table 1-2. Most of the structures investigated to date are capable of oxygen capture and release and are in current use in SOFCs as anode and cathode materials. Methane combustion and oxidation are other processes where these materials were shown to be useful. Due to their oxygen-storage abilities, they have the potential for use in CLC but require further improvements since the substantial ordering of oxygen ions in their structure decreases their mobility and, consequently, their oxygen capture and release capacities [78].

Density functional theory studies

A density functional theory (DFT) study can be a relatively helpful tool to better justify and understand the behavior of oxygen carriers during the reaction on a molecular level. This theory has gained importance in facilitating an approach to interpreting the geometric and electronic structure of metal oxide interfaces. This knowledge will enhance understanding of atomic level properties and behaviors [79] such as ion conductivity behavior, structure-bonding, spectroscopic properties and many more [80, 81]. [82] used DFT to examine a double perovskite $GdBaCo_2O_{5+\delta}$ as cathode material for SOFCs. DFT was used to clarify the oxygen and vacancy arrangements and the mechanism of oxygen migration in the structure as functions of the material compositions and ambient temperature. The oxygen reduction reaction in perovskite oxides is indicative of the strength of the bond between the transition metal ion and oxygen. Consequently, it can represent the catalytic activity of the perovskite and its oxygen ion mobility. [83] studied the oxygen reduction reaction in $LaBO_3$ (B = Mn, Fe, Cr) and compared these three perovskite metal oxides catalytic activity using the DFT method. The double perovskite Ba_2MnMoO_6 was investigated by [84] using the DFT method to study the structural parameters associated with its magnetic properties. All the results from experiments on perovskites and double perovskites published in the literature, with a few of those above, reveal that using DFT could be a powerful tool to better understanding the behavior of these oxides and facilitates the approach to optimized oxygen carriers for CLC applications.

Reactors in chemical looping combustion

As stated previously, CLC can be carried out using solid, liquid or gaseous fuels. Different kinds of reactors can be used for this process; the choice of the most appropriate reactor can be made according to the fuel and operating conditions,. [85] proposed a design procedure for application in chemical looping combustion reactors (Figure 1-5).

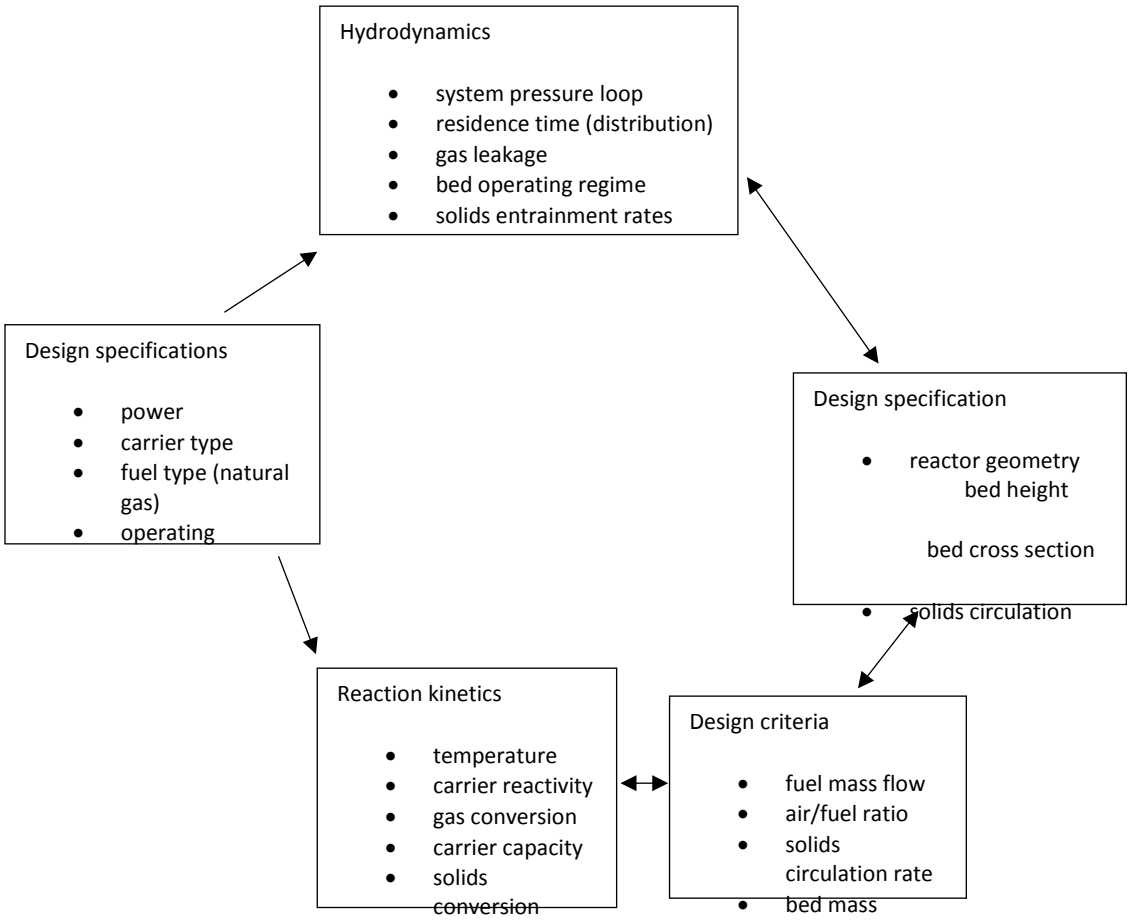

Figure 1-5 Design procedure for chemical looping combustor [85].

According to Kronberger et al. (2005), due to the heterogeneous nature of the CLC process, there is a need for oxygen carriers to be fluidized and be in maximal contact with both fuel and air streams to be more functional. A circulating fluidized-bed reactor (CFB), as shown in Figure 1-6, is preferred since good contact is achieved between the solid and the gas. Use of a fluidized-bed reactor is advantageous since all the oxygen carrier materials are in contact with

the same average gas atmosphere and, as a result, has the same amount of oxidation and reduction at a steady state [86, 87]. Using a fluidized-bed reactor also facilitates the continuous flow of solid materials between reactors [88]. Due to their applicability to industrial processes and commercial use (biomass pyrolysis and gasification [89, 90] and fluidized catalytic cracking [86]), these reactors have attracted more attention than other kinds of reactors [91]. The additional energy required for particle circulation and particle separation (using a cyclone) are downsides of this reactor system, which might result in higher costs. Particle attrition is also more likely to occur, which reduces the process efficiency [2]. Particle attrition will also result in the production of fine particles requiring removal.

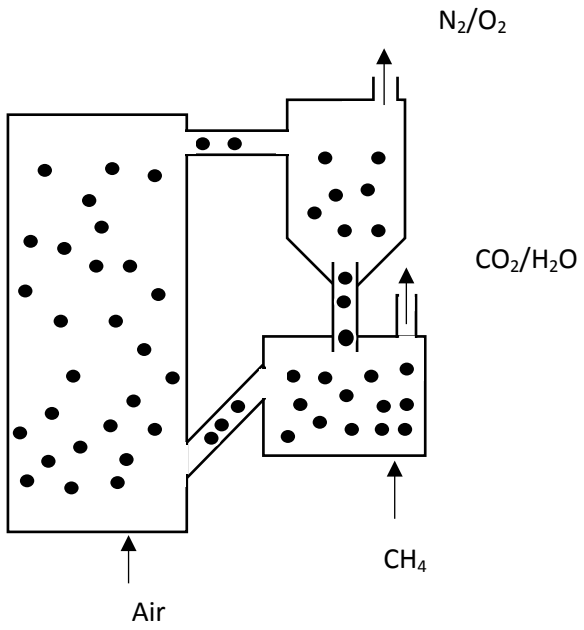

Figure 1-6 Scheme of fluidized-bed reactor for application to CLC [92].

Fluidized-bed reactors can have different configurations, such as riser and bubbling fluidized beds, two bubbling fluidized beds [93, 94] and dual circulating fluidized beds.

Figure 1-7 represents two interconnected fluidized beds with a high-velocity fluidized-air tank and a low-velocity bubbling fuel tank. In this system, the air reactor is approximately 10 times larger than the fuel tank. To maintain a reasonable size of the air tank, a high-velocity air-stream is required. The air-flow makes it possible for the oxygen carrier particles to move towards a cyclone which leads them to the fuel tank for reduction. The fuel tank is located at

sufficient height to enable the particles to move back to the air reactor by the force of gravity [95]. The outlet stream of the fuel tank undergoes a condensation step to separate the CO_2 and H_2O. The non-condensable gases which contain unreacted methane and N_2 are recycled. In these systems, a loop seal is usually used to separate the fuel and air gases during the process. This approach might incur high operational and installation costs.

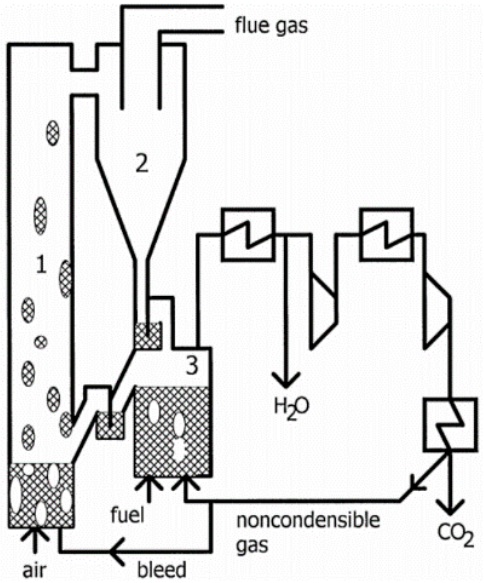

Figure 1-7 Diagram of CLC process including riser and bubbling bed, air tank (1), cyclone (2), fuel tank (3) [95]. Copyright permission was received.

Dual circulating fluidized beds (Figure 1-8), on the other hand, have low operational and installation costs. However, there is a good chance of the air and fuel streams leaking into the fuel and air tank, respectively, which may reduce the process efficiency. In these systems, there is a need for further caution for gas leakage prevention [2]. It is important to note that industrial chemical looping processes are carried out on a much higher scale than pilot plants, requiring several hundreds of megawatts. Accordingly, the bubbling fuel tank does not represent an economic option for two reasons. This system requires huge bed surfaces as well as a high gas-solid contact time; the interaction requires a turbulent and highly fluidized flow which is only achieved in a fuel tank with a fluidized stream [96].

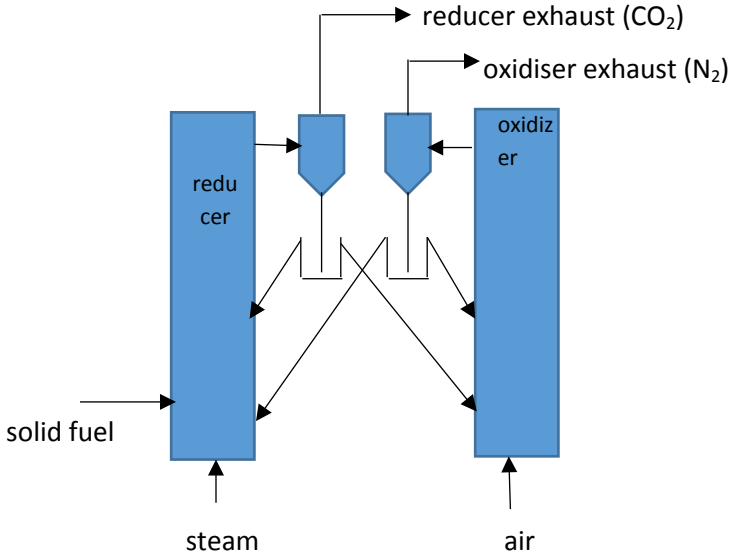

Figure 1-8 Diagram for a dual circulating fluidized-bed reactor for CLC process.

Packed-bed reactors (Figure 1-9) have also been investigated for CLC processes. Packed-bed reactors are single dynamically operated fixed-bed reactors in which oxygen carriers are located at a fixed position. There is a gas-switching system which affords the air and fuel entry to the reactor alternately and it can have two configurations, co-current and counter-current feeding [97]. In this kind of reactor, there is less probability of particle attrition nor need for the gas-solid separation process used in fluidized beds. In packed-bed reactors, for high-energy efficiency, a high-temperature gas stream supply to the downstream gas turbine is required. This can be achieved by having two parallel packed beds for operation. In packed beds, it is important to optimize the operating conditions to guarantee methane slip avoidance. This reactor operates in a non-continuous mode which can be of concern for CLC design. Operation at high temperatures and the high flow gas switching system requirements are major drawbacks of this system [92, 98, 99]. Another major problem with reactor systems with fixed beds is that they also have a low tolerance to particle volume changes during the process [100]. It is believed that this reactor's high sensitivity to chemical degradation is the most challenging problem in proposing this reactor type for CLC applications [86].

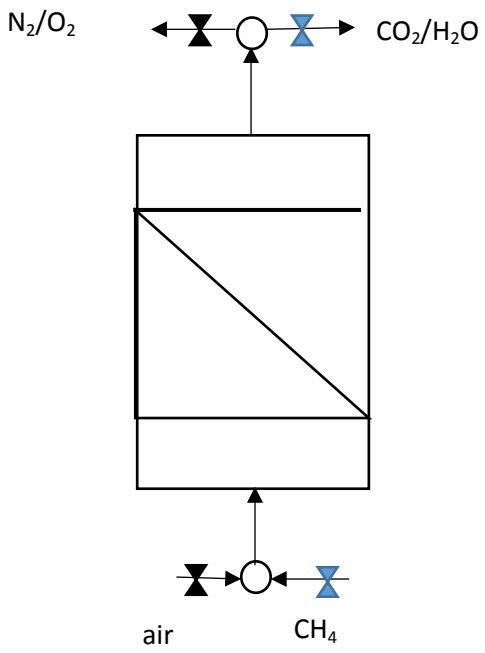

Figure 1-9 Scheme of packed-bed reactor used in CLC.

A rotating packed bed is another alternative as a chemical looping combustor. In this type of reactor, oxygen carriers are held in a doughnut-shaped fixed bed that rotates between different gas streams. Figure 1-10 shows the oxygen carriers in contact with different gas streams for certain amounts of time (depending on the rotation speed), thereby facilitating the oxidation and reduction reactions. The gas streams are: (i) fuel, (ii) inert gas and (iii) air which are blown radially outward. The steam sector is used to prevent the gases from mixing [100, 101]. The potential particle volume changes and fine formation remain a problem as this reactor comes within the packed-bed reactors category [100]. In rotary reactors, gas-solid separation is intrinsically unnecessary (as in fixed- bed reactors), the operation is in continuous mode and the design is compact and readily scaled up [102]. The major challenge in dealing with these reactors is intrinsic gas mixing. To avoid friction between the different parts, a space is required between them. The rotating bed holder and the shafts driving it are the moving parts of the reactor, while the inner axis containing the feeding sections and the housing is static. Sideways diffusion of the gases (inert gas, fuel and air) is possible along the inner and outer interfaces of the bed, leading to gas slippage. This gas slippage can result in gas mixing, resulting in reduced efficiency [101].

Figure 1-10 represents the front view of a rotary packed-bed reactor.

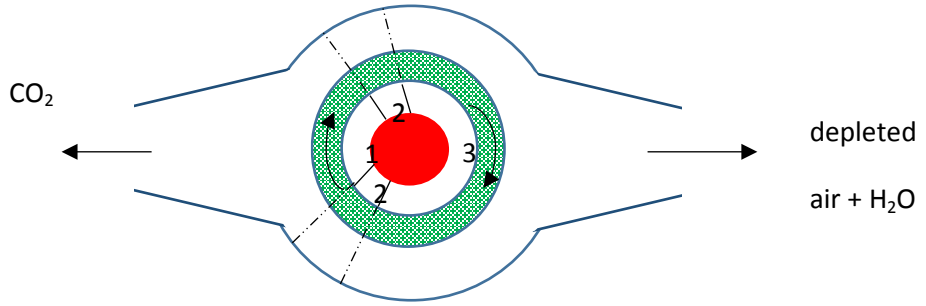

Figure 1- 10. Rotary packed-bed reactor from above with green section representing fixed oxygen carriers within the reactor. The thick solid lines are separation walls, while the dotted lines indicate the various sectors; 1 – fuel, 2 – inert gas, 3 – air.

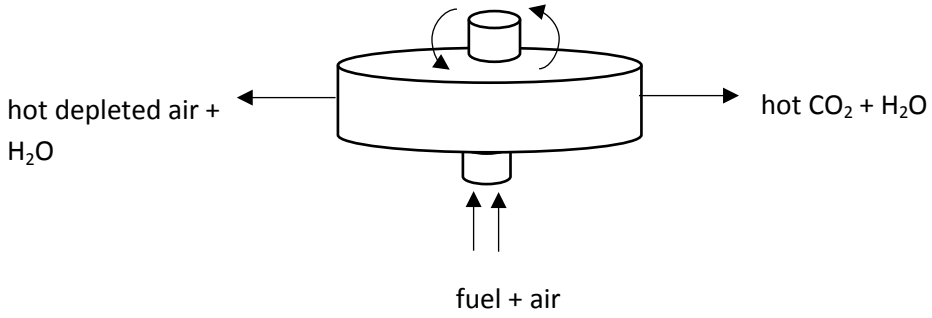

Figure 1-11 Front view of rotary packed-bed reactor.

Oxygen carriers can be positioned differently in a rotary bed. A rotary reactor design with micro channel structures was investigated by [102-104]. This reactor system operates in the same way as a packed-bed rotary reactor with one major difference. As is shown in Figure 1-12, the oxygen carriers in this reactor are located on the inner walls of micro channels within the rotary wheel. The oxygen carriers are sited on a bulk of dense ceramic layer with high thermal inertia and conductivity. This design is proposed as being compact, stable and associated with minimal energy penalty.

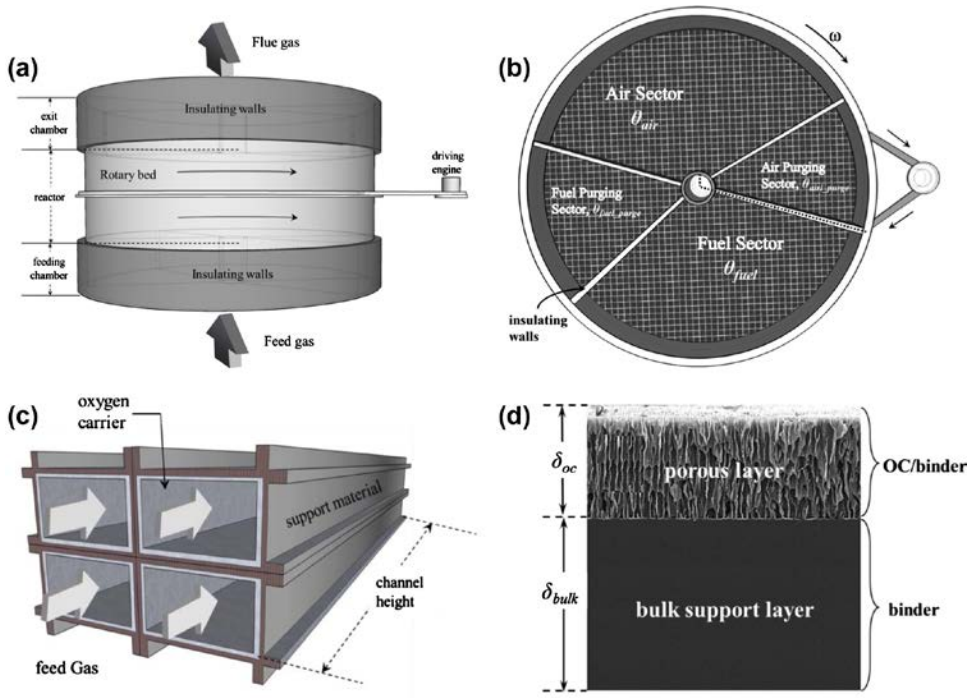

Figure 1-12 Rotary reactor with micro channels from different aspects; front view (a), bottom view (b), individual channel structure (c) and the oxygen carrier coated on the surface (d). Copyright permission received [104].

Moving-bed reactors [105, 106] can also be considered for application to chemical looping processes. Moving-bed reactors are reactors in which the oxygen carriers move through the reactor along with the fuel and air streams. They are open systems and operate in a steady state. [105] investigated the chemical looping gasification of syngas using both fluidized-bed and moving-bed reactors. It was shown that a moving bed of oxygen carriers with a counter-current gas–solid contact pattern can result in maximal conversion. Figure 1-13 shows the reduction tank with two inlet streams of syngas and oxygen carriers. Use of a counter-current pattern enables the fresh syngas stream to be in contact with oxygen carriers (Fe based) with lower oxidation states, while enabling contact between syngas stream with lower concentrations of H_2 and CO and fresh oxygen carriers. This approach is expected to provide maximal solid/gas contact and to maximize the conversion rate. The moving bed can also be used as an air tank.

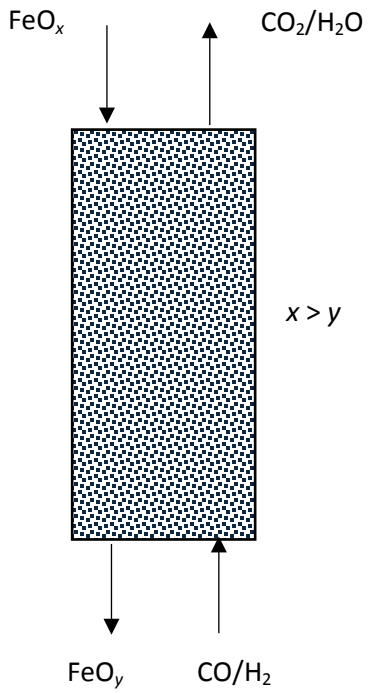

Figure 1-13 . Chemical looping gasification process in moving-bed reactor as reducer using Fe-based oxygen carrier.

Table 1-3 summarizes the advantages and disadvantages of each type of reactor for use in CLC processes. The operational conditions and fluidization regimes given in Table 1-4 present an average of the data given by different researchers and studies.

Table 1-2 Advantages and disadvantages of reactors applicable to CLC

Parameters	Reactor type			
	Fluidized beds	Packed bed	Rotating reactors	Moving-bed reactor
advantages	commercialized and industrialized, good gas–solid contact, continuous mode	no need for gas-solid separation, less particle-attrition potential	continuous mode, compact, stable and readily scaled up, no need for gas–solid separation	continuous mode, maximal conversion due to high gas–solid contact

disadvantages	gas–solid separation required, additional energy for particle circulation and gas-solid separation required, more potential for particle attrition	non-continuous mode, requires high temperature and high gas flow switching system, low tolerance to particle volume changes, high sensitivity to chemical degradation	intrinsic gaseous species mixing	gas–solid separation required, particle attrition potential
(m s^{-1})/fluid velocity	0.10–7.32 air > fuel	0.1–12	0.05–0.6	–
Pressure drop/kPa	2.5–20	0.7–100	1	–

As is shown in Table 1-3 and stated previously, different reactor types have been proposed and applied in different scales to chemical looping processes. The initial CLC reactor tests were carried out using single fixed-bed reactors [49, 51]. The reactor most commonly in use is the fluidized-bed reactor and other reactor types have been proposed to obviate the major drawbacks of these reactors.

CLC reactors have been operated in a temperature range of 400–1300 °C, depending on the oxygen carrier, operating conditions and reactor scale. The fuel and air velocity in the fuel and air tanks can vary according to many variables such as oxygen carrier size and density, temperature and pressure, reactor height, oxygen carrier type, its reactivity and many more. Clearly, no exact range for this parameter can be presented. However, an approximate range can be of advantage while studying different kinds of reactors. Several design parameters can be of use in designing a chemical looping combustor. However, due to the different variables, presenting a range for each and every one of these parameters does not appear to be effective in

designing a reactor since each reactor, taking into consideration its type, fuel type and oxygen carrier, might require specific reaction conditions.

The proposed reactor types have their own advantages and disadvantages, hence the need for further improvement. In general, a reactor which can provide an inlet gas pressure of above 20 bar, efficiency of 53 % and inlet temperature of 1200 °C is a reactor suitable for this purpose [107].

Conclusion

The information presented here summarizes what has been published in the literature. Recently introduced materials known as single perovskites, with the general formula of ABO_3, have been shown to be promising oxygen carriers for CLC processes. However, some of these introduced single perovskites were improved by doping on the A and B-sites with different materials. Some of them require further improvement for a more efficient CLC. The single perovskites investigated in the literature are divided into four categories: (i) $La_{1-x}Sr_xFe_{1-y-z}Co_yB_zO_3$, (ii) $La_{1-x}Ce_xBO_3$, (iii) $LaNiO_3$ and (iv) $AMnO_3$. Double perovskite structures with the general formula of $A_2BB'O_6$ have also been investigated for their oxygen capture and release abilities. All of them can be classed within five groups: (i) AMo, (ii) ACo, (iii) AMn, (iv) mixed and (v) others. They have been investigated as oxygen carriers in SOFC, used as anode and cathode materials and also for methane oxidation and combustion. They exhibited the ability to capture and release oxygen in oxidation and reduction atmospheres. Improvements were also introduced to some existing double perovskites and some require further improvements. There is also a need for these materials to be used as oxygen carriers for chemical looping purposes. DFT is a useful tool for a better understanding of the oxygen carrier behavior under different temperatures and with different compositions of materials which can be used for further improvement of the oxygen carriers and, consequently, the CLC process. Chemical looping reactors are also briefly discussed in the presented study. Different reactors can be used for CLC and CLOU. These reactors are fluidized-bed reactors, packed-bed reactors, rotating reactors and moving-bed reactors. All of these reactors have been investigated to compensate for the shortcomings of others; however, while each of them possesses distinct advantages over the others, they also have their own drawbacks and problems. Commonest of them all is the fluidized-bed reactor, since it has already been commercialized and industrialized.

1 Materials and Methods

1.1 C.1 Synthesis of doped perovskite-based oxygen carrierrs

The perovskite-based oxygen carrier particles were synthesized using solid-state reaction followed by mechanical extrusion. The preparation steps are as follows:

Powders with an average particle size of ~46 μm (325 mesh) were mixed in an appropriate weight ratio according to Table 2-1 to make 10-250 g batches of the final product in each case.

Each mixed batch was transferred to a 250 mL plastic drum with 33 g of water, which was placed in a rotary tumbler for one and a half hours. In accordance with the literature, 30 vol. % solid loading with 1 wt. % of the dispersant (ammonium polyacrylate, NH4PAA, dispersant) was used. The aqueous slurry was thoroughly mixed and homogenized in a rotary tumbler unit. The slurry was poured into a shallow pan (Pyrex) and dried at 150 °C in an air oven overnight. The dried soft mass was then crushed and ground to a homogeneous powder for each batch. Furthermore, the dried cake was pulverized and homogenized. This procedure is followed by extruding into rods.

In our case, the following components were used for preparing the extrusion paste: water both as binder/solvent, PVA as a binder (20 wt%. solution), water soluble starch as a pore former and binder, and ammonium hydroxide as peptizing agent. After obtaining a suitable viscosity of the blended materials, they were extruded using a simple manual extruder. Extrudates were dried on a stainless steel plate at 75°C overnight. The extrudes were transferred to high-density alumina crucibles and calcined in air for 6 hours at 1200°C in a programmable muffle furnace using the temperature−time profile shown in Figure 2-1.

The particles should have a specific size range for use as oxygen carriers. To achieve this objective, the calcined extrudates were sieved through stainless-steel screens to yield particles in the range of 125−250 μm. The resulting powders were washed and put through an ultrasound (50-60 Hz) for 5 min, each time for five times to remove the fine particles that may come from crushing stage.

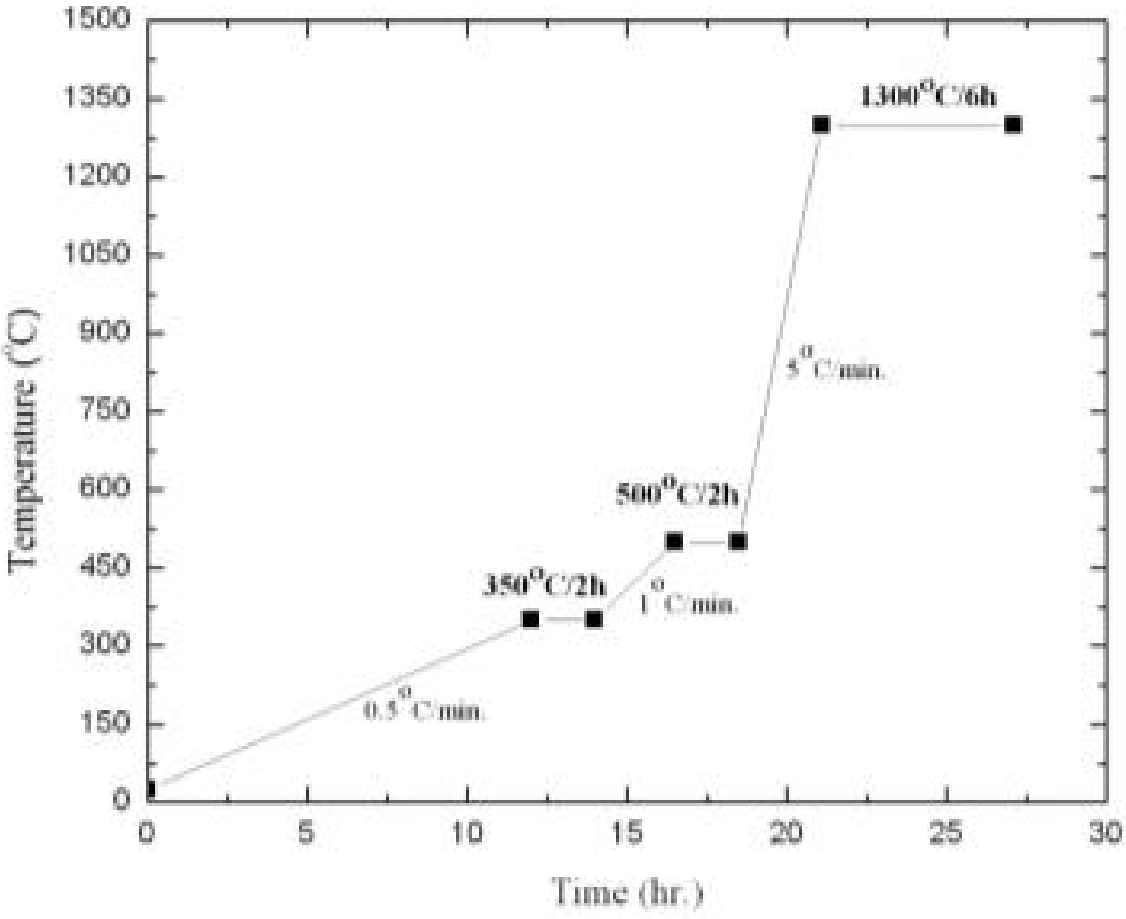

Figure 2-1 Temperature- time Schedules for the processing of carriers

Table 2-1 Perovskite formulations (mol ratio) investigated in this work.

Code	Ca	Mn	Fe	Ti	Ni	Zr	Al	Sr	La	Mo	Mg	Ba	Co
CM	1	1											
CLMF	0.9	0.9	0.1						0.1				
CLMT	0.9	0.9		0.1					0.1				
CLMNi	0.9	0.9			0.1				0.1				
CLMZ	0.9	0.9				0.1			0.1				
CLMA	0.9	0.9					0.1		0.1				
CLMF6491	0.6	0.9	0.1						0.4				
CLMF9164	0.9	0.6	0.4						0.1				
CLMF9110	0.9	1							0.1				
CLMF1091	1	0.9	0.1										
CSMF	0.9	0.9	0.1					0.1					
CSMZ	0.9	0.8				0.1		0.1					
SF			1					1					
SFMn21901		1.9	0.1					2					
SFMn21505		1.5	0.5					2					
SFMn21010		1	1					2					
SFMn201505		1.5	0.5					2					
SFMn2019		0.1	0.9					2					
CMA21010	2	1					1						
CMA21208	2	1.2					0.8						
CMA21307	2	1.3					0.7						
CMA21505	2	1.5					0.5						
CMA21901	2	1.9					0.1						
SMoCo								2		1			1
SFMo111			1					2					1
SFMo191			1.9					2		0.1			
SFMO21901			1.9					2		0.1			
SMMo		1						2		1			
SMgMo								2		1	1		
SMCoMo		1.8						2			0.1		0.1
CFMO	2		1							1			

CFMO191	2		1.9							0.1			
SMgMo								2		1	1		
LCMCo	0.35	0.3							0.7				0.7
BLF			3						1			2	
CMT													
CMF	2	1	1										
SMo								2		2			
SFA91			1.9			0.1		2					
SFCo91			1.9					2					0.1
SFM91		0.1	1.9					2					
SFT91			1.9	0.1				2					
SFM73		1.7	0.3					2					
SFM82		1.8	0.2					2					
SFM91		1.9	0.1					2					

1.2 C.2 Characterization of the oxygen carriers

In every case, the Brunauer− Emmett−Teller (BET) specific surface area was measured by N_2 adsorption (Micromeritics, TriStar 3000).

The crushing strength (force needed to fracture a single particle) was measured using a digital force gauge (Shimpo, FGN-5) for particles in the size range of 125− 250 μm. An average of 30 measurements was taken as the representative of the crushing strength.

Powder X-ray diffraction (XRD, PANalytical X'Pert Pro) with Cu Kα1 radiation was used for crystalline phase determination of the prepared oxygen carriers.

Scanning electron microscope (SEM) (Hitachi, S4800) was used for examining the morphology of the synthesized particles.

Oxygen capacity (RO) of the prepared materials was measured using a thermogravimetric analyzer (TA Instrument, TGA Q50). An approximate amount of a sample (~12 mg) was placed

inside a crucible, and the experiment was conducted by initiating the heating in an oxidizing ambient environment (20.8% O_2) with an inlet flow rate of 50 mL/min. The heating rate was a linear ramp of 45 °C/min, and after reaching 950 °C, the temperature was maintained constant for 35 min. While the temperature was kept constant, the sample was then in direct exposure to a stream of high-purity N_2 for 35 min with an inlet flow rate of 50 mL/min. These reduction−oxidation cycles were repeated 3 times. The thermo balance was calibrated with an empty platinum crucible under identical experimental conditions before each experiment.

Experiments for examining oxygen uncoupling and reactivity characteristics were performed in a quartz fluidized-bed reactor (designed in Chalmers University and fabricated in The University of Toledo), 870 mm high and 22 mm in inner diameter. A porous quartz plate is located at a height of 370 mm from the bottom, and the reactor temperature is measured with chromel-alumel (type K) thermocouples enclosed in inconel-600 in quartz shells located about 25 mm above and 5 mm below the plate. The experiments were performed at 800, 850, 900 and 950°C, as measured by the upper thermocouple.

To determine if the particles are fluidized or not, the pressure drop over the bed of particles and the quartz plate was recorded by using pressure transducers. In order to be able to preserve the temperature at the desired level over the progress of the experiment, the fluidized bed quartz reactor was placed inside an electric cylindrical furnace (Applied test system. INC).

The oven was insulated, and the openings through which the gases enter and exit the reactor were also insulated with a silica blanket type SB-2000 from Zicar refractory composites. In order to remove water and small solid particles generated during oxidation of the fuel, the exhaust gas stream from the reactor was led to a condenser (IMR 500 P). The composition of the dry gas was

measured by IMR 2800 P analyzer, which measures the concentrations (sensitivity of 0.001%) of O_2 through a paramagnetic channel and CO_2, CO, and CH_4 through infrared channels. The tubing and fittings were made from stainless steel and were made by Swagelok. In order to connect the tubing to the quartz reactor, graphite ferrules (GRACE, USA) were used. There are two advantages for using these ferrules; one is the high temperature resistivity (near 450 °C), and the other is the suitability for the glass fitting.

The CLOU properties of the particles were investigated by examining the oxygen release from the oxidized particles in nitrogen while fuel reactivity is examined by reaction with methane. The experiments were conducted in cyclic approach, in which a period of oxidation followed by a period of reduction constitute one cycle. Reduction was performed either with inert gas, in order to examine O_2 release, or with fuel in order to examine fuel reduction.

The oxidation is conducted with a flow of 900 mLN min-1 (normalized to 1 bar and 25°C) of N_2 with 8 % O_2. The fuel reduction is examined with a flow of 200 mLN min-1 of CH_4.

In order to control the flow rates, mass flow controls (Smart-Trak® 100 Series) were used. In addition a computer program was written using Visual C++.net to program the flow meters in the desired cyclic approach.

Batches of 30 g of oxygen carrier are used with a particle size of 125−250 μm. The composition of the reducing gas was 18 vol % CH_4 in N_2, and it was selected to avoid exceeding the terminal velocity of the particles due to the increase in gas velocity produced during the CH_4 conversion. A mixture of O_2 with N_2 was used during the oxidation with a low O_2 concentration (8 vol %). Since the reactor had no cooling system, to avoid a large temperature increase during the combustion reaction, 8% O_2 concentration was used instead of air. The reduction period was

20 s. The oxidation period necessary for the complete oxidation varies between 600 and 900 s. To avoid mixing of CH_4 and O_2, N_2 was introduced for 45 s after each reducing and oxidizing period. The tests were carried out at 800, 850, 900 and 950 °C. Extended operation CLC (100 cycles) was performed on selected oxygen carriers. According to the previous results, $CaMnO_3$ and $CaSrMnFeO_3$ were selected as oxygen carriers.

1.3 C.3 Establishment of experimental set up

Experiments for examining oxygen uncoupling and reactivity characteristics were performed in a quartz fluidized-bed reactor (designed in Chalmers University and fabricated in University of Toledo), 870 mm high and 22 mm in inner diameter. In Figure 2-2 the gaseous fuel reactor is shown.

Figure 2-2 Gaseous fuel reactor

The scheme of the experimental setup is shown in Figure 2-3. A porous quartz plate was located at a height of 370 mm from the bottom, and the reactor temperature was measured with chromel-alumel (type K) thermocouples enclosed in inconel-600 in quartz shells located about 25 mm above and 5 mm below the plate. The experiments are going to be performed at 850 – 1000 °C, as measured by the upper thermocouple.

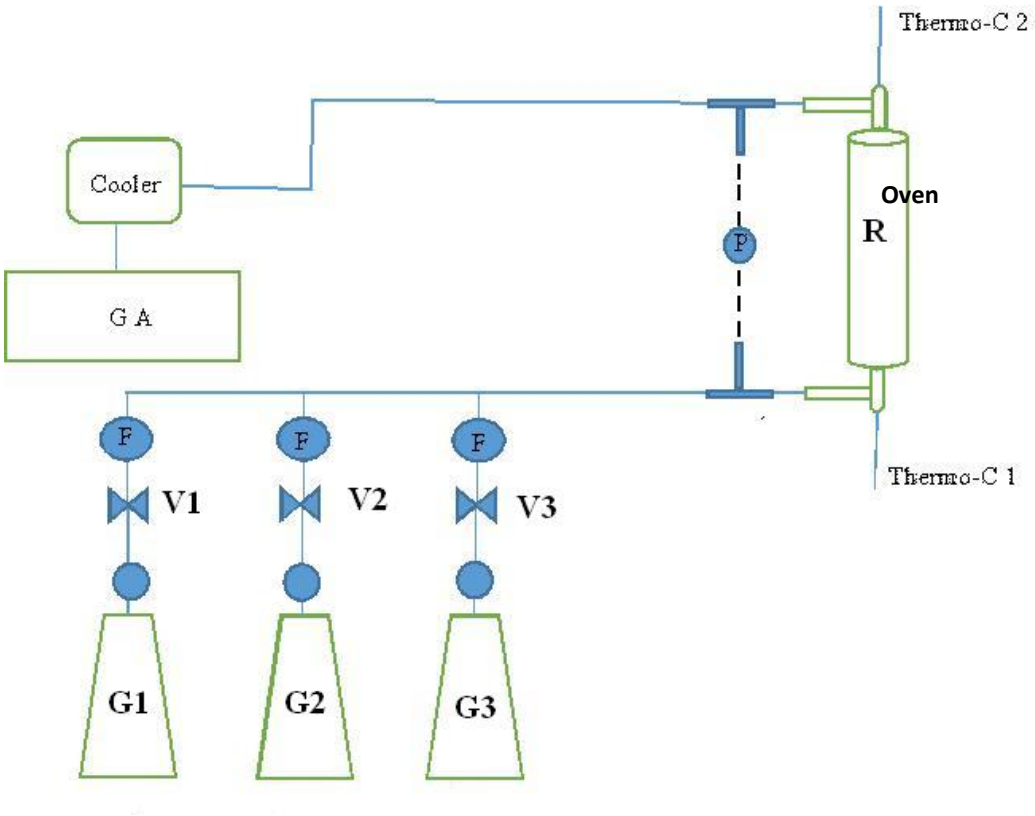

Figure 2-3 Experimental setup.P= pressure transducer, F=flow meters, GA=gas analyzer, V=valves, G1= N_2, G2=N_2-5%O_2 and G3=CH_4

To measure the pressure drop over the bed of particles and the quartz plate a pressure transducers (Figure 2-4 Honeywell-frequency of 20 Hz) is utilized. Fluctuations in the pressure drop make it possible to determine if the particles were fluidized or not.

Figure 2-4 Pressure transducers (Honeywell-frequency of 20 Hz)

In order to be able to preserve the temperature at the desired level over the progress of the experiment, the fluidized bed reactor of quartz is placed inside an electric cylindrical furnace

(Applied test system. INC). The oven was insulated and the openings through which the gases entered and exited the reactor were insulated with silica blanket type SB-2000 from Zicar refractory composites (Figure 2-5).

Figure 2-5 Silica blanket type SB-2000 from Zicar refractory composites

In order to remove water and small solid particles, which are generated during oxidation of the fuel, the exhaust gas stream from the reactor was led into a condenser (IMR 500 P-Figure 2-6).The composition of the dry gas was measured by a IMR 2800 P analyzer, which measured the concentrations (sensitivity of 0.001%) of O_2 through a paramagnetic channel, CO_2, CO, and CH_4 through infrared channels, and H_2 through the difference in thermal conductivity of H_2 and N_2.

Figure 2-6 IMR 500 P

The tubing and fittings are made from stainless steel and were made by Swagelok. In order to connect the tubing to the quartz reactor graphite ferrules (GRACE, USA Figure 2-7) are used. There are two advantages for using these ferrules; one is the high temperature resistivity (near 450 °C) and the other is the suitability for the glass fitting.

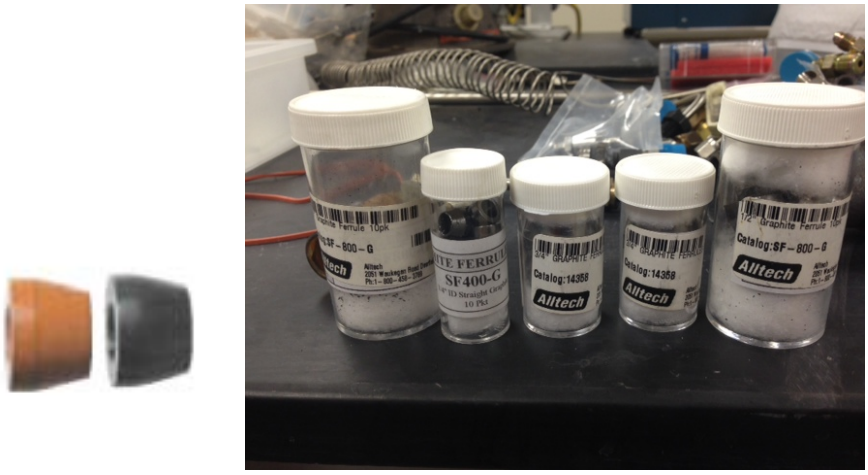

Figure 2-7 Graphite ferrules (GRACE, USA)

The CLOU properties of the different particles were investigated by examining the oxygen release from oxidized particles in nitrogen, while fuel reactivity was examined through reaction with methane. The experiments ran in cyclic approach, in which periods of oxidation

follow by a period of reduction constitute one cycle. Reduction was performed either with inert gas in order to examine O_2 release or with fuel in order to examine fuel oxidation. The oxidation was conducted with a flow of 900 mL_N min-1 (normalized to 1 bar and 25°C) of N2 with 5 % O_2. The fuel reduction was conducted with a flow of 450 mL_N min-1 of CH_4. In order to control the flow rates and these fashion approaches mass flow controls (Smart-Trak® 100 Series Figure 2-8) are used. In addition a computer program was written by Visual C++.net to program the flow meters in the desired cyclic approach.

Figure 2-8 Mass flow controls (Smart-Trak® 100 Series)

In Figure 2-9 the whole setup layout is shown.

Figure 2-9 The whole setup layout installed in University of Toledo

1.4 C.4 Activity Assessment

Prior to experiments a total of 15 g of the CLMF powder (particles in the range of 125−250 μm) was placed on the porous plate, and the reactor was heated to 850 °C in a 5% O_2−95% N_2 mixture to oxidize completely the oxygen carriers. In order to investigate the oxygen release a set of three inert gas (N_2) cycles were carried out at 850°C for 60 s before and after fuel cycles. Methane was used as fuel for 25 s during the reduction periods at 850 °C. Nitrogen was used as an inert purge for 20 s in between oxidation and reduction. Each cycle was repeated three times to find reproducibility of the experiment. Flow rates of 450, 600, and 900 mL_N/min were used during reduction, inert, and oxidation, respectively. These flow rates were chosen based on calculated superficial gas velocity, U, in the reactor. To reach this

velocity, a value of the approximately 4−7, 7−13, and 11−20 times higher than the calculated minimum fluidization gas velocity, U_{mf}, of the oxygen carrier particles during reduction (with methane), inert, and oxidation periods, is required respectively. By using the correlation given by Kunii and Levenspiel [108] the minimum fluidization velocity, U_{mf}, was calculated.

Figure 2-10 shows the oxygen release profiles during inert gas purge at 850 °C for the iron doped sample. As it can be seen, the perovskite formulation showed an oxygen uncoupling behavior. The oxygen release trend was a steady decay in the amount of released oxygen as a function of time. This is typical for the perovskite-type of materials, where the release or uptake of oxygen is a function of the oxygen partial pressure in the ambient, according to Equation .1 is believed to be involved. In this equation, AR is air reactor and FR stands for fuel reactor.

Equation .1 $$\boldsymbol{ABO_{(3-\delta)AR} \leftrightarrow ABO_{(3-\delta)FR} + \frac{1}{2}(\delta_{FR} - \delta_{AR})O_2}$$

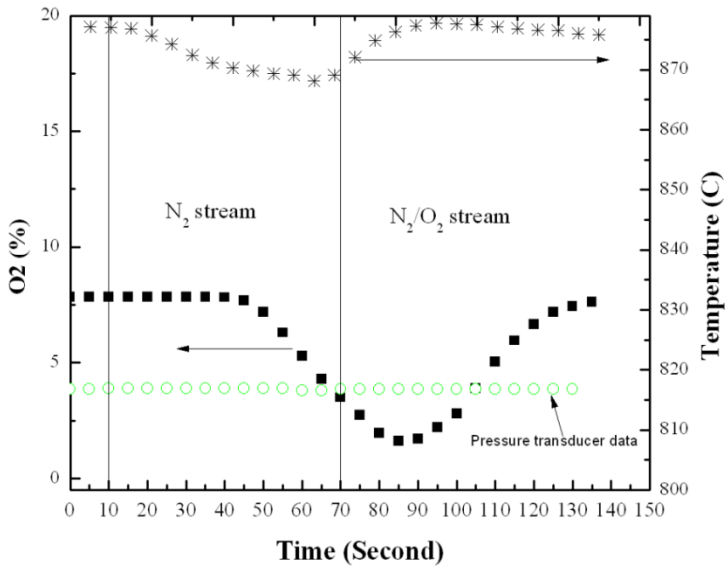

Figure 2-10 Oxygen release and uptake profile for iron carrier investigated in this work during inert gas purge for 60 s at 850 °C.

According to temperature profile shown in Figure 3.1 the oxygen uptake is an exothermic, while the oxygen release is an endothermic reaction.

15 g of particles in the bed was employed to investigate the reactivity of the particles with methane as fuel at 850 °C. A typical concentration profile during the reduction period for CLMF is shown in Figure 2-11. To start the experiment, the carrier was oxidized in 5% O_2, but when the oxidizing stream was replaced with pure nitrogen (inert), the oxygen concentration decreased steadily. Upon the addition of CH_4 the oxygen concentration decreased faster. After the reduction period, initially, the depleted oxygen carrier consumed all oxygen in the inlet stream for more than 120 s. After this time, oxygen broke through and increased steadily, finally approaching and leveling off at the inlet concentration (7%). The fact that no oxygen is seen during the initial stages of oxidation indicated that the carrier had undergone a high degree of reduction. Therefore, the oxygen partial pressure was rather low at that point, as the oxygen-depleted carrier consumed most of the oxygen in the early part of the oxidation period.

Based on pressure transducer data, there was no fluctuation in pressure during the test, which shows the particles were fully fluidized during the test.

The temperature profile of the gases displayed that the reduction in methane is exothermic, while the reduction in N_2 is endothermic.

A successful initialization of the reactor setup was achieved in University of Toledo and we will be able to investigate the CLC and CLOU of different particles, which are synthesized previously. In the next step, more careful analyzes will be performed on our new perovskite structures.

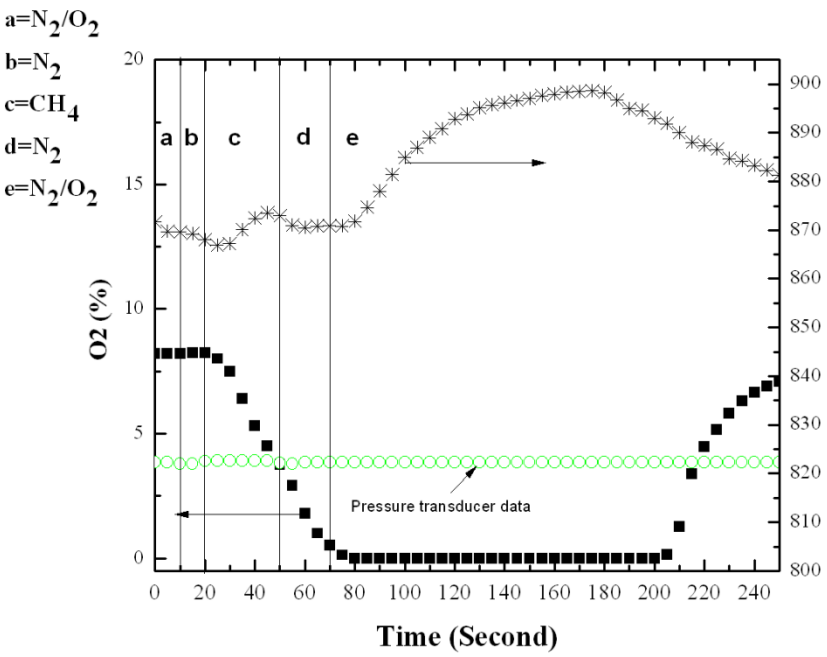

Figure 2-11 Concentration of Oxygen gas, gas The temperature profile and pressure transducer data during conversion of CH_4 at 850 °C for 20 s using CLMF (15 g of sample) followed by oxidation in 5% O_2.

2 Results and discussion

2.1 Oxygen Carrier Development: Subtask C.1 and C.2 Synthesize and Characterization of doped perovskite-based oxygen carriers Selection- synthesis-characterization

2.1.1 XRD diffraction analysis

The XRD analyses of fresh samples for CLMNi, CLMZ, CLMT, and CLMF which were heat treated at 1300°C for 6 hours are shown in Figure 3-1. The XRD results confirmed the formation of the perovskite phase at this temperature (Figure 3-1). A thorough analysis of the XRD signatures is difficult because of the superimposition of several diffraction peaks.

In the case of A- and B-site-doped particles (CLMT, CLMF, and CLMM), the XRD patterns looked very similar to each other in all cases without any evidence of other residual phase, indicating that the stoichiometry of the precursor was correct for the production of the perovskite structure.

Besides the ionic radii requirements, another condition to be fulfilled is electroneutrality, i.e., the sum of charges of A and B equals the total charge of oxygen anions. This is achieved by means of suitable charge distribution of the form $A^{1+}B^{5+}O_3$, $A^{2+}B^{4+}O_3$, or $A^{3+}B^{3+}O_3$. In addition to this, partial substitution of A and B ions is allowed, thus yielding a excess of compounds while preserving the perovskite structure. However, deficiencies of cations at the A- or B-sites or of oxygen anions are common, which results in defective perovskites. Oxygen vacancies are more common than those involving cationic vacancies [109]. In Figure 3-1-b the main peak shifts of the XRD pattern are shown. In reality, transition ions (Ni^{2+}, Zr^{4+}, Ti^{4+} and Fe^{3+}) instead of manganese ions (Mn^{4+}) incorporate into perovskite lattice and carry an excess or shortage of positive charge into the lattice which should be compensated. Compensation can be affected by formation of oxygen vacancies ($V_{[O}^{2+}{}_{]}$) or gaining oxygen ions. Formation of oxygen vacancies will expand the lattice and the lead to shifting the Bragg reflections to the left.

On the other side, replacing ions with different sizes will result in lattice expansion or contraction. The order of ionic size of ions which were used in this study is as follows: Mn^{4+} <Fe^{3+}< Ti^{4+} <Zr^{4+} <Ni^{2+}. As it can be seen nickel ions are bigger than the others which may result in higher lattice distortion with respect to others and lead to Bragg shift to the left as it can be seen in Figure 3-1-b.

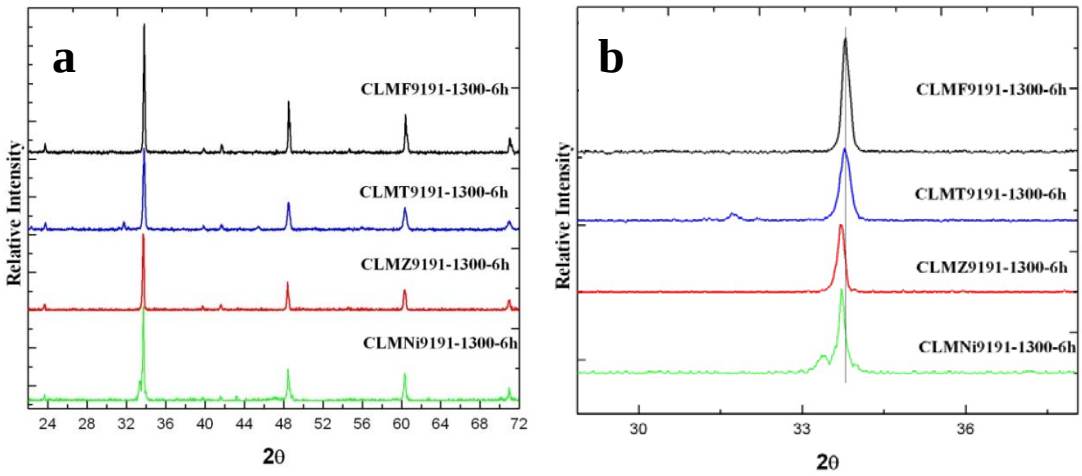

Figure 3-1 XRD patterns of fresh samples for CLMNi, CLMZ, CLMT, and CLMF soaked at 1300°C for 6 h (a). Zooming at main peak (b).

The XRD pattern of the CLMF9191 sample which is heat treated at three different temperatures is shown in Figure 3-2. Increasing the heat treatment temperature leads to shifting the Bragg reflections to the left, while the intensity of the peaks increases as well. There is no evidence of any second phase in the XRD spectra while the heat treatment temperature is increased, implying that the chemicals reacted well and formed a new perovskite phase. As it can be seen from Figure 3-2 the peaks are sharper which indicate the growth of the powders is caused by an increase in temperature.

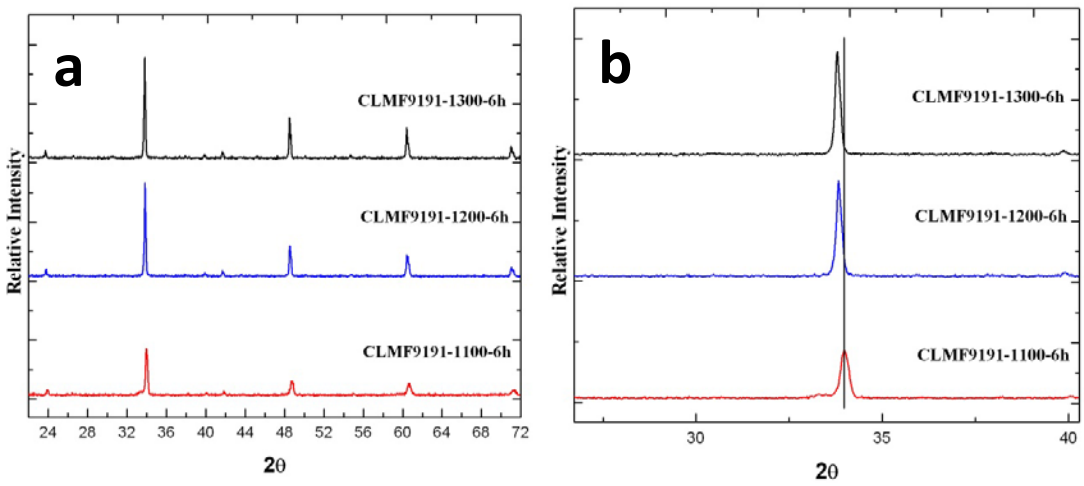

Figure 3-2 XRD patterns of CLMF soaked at 1100, 1200 and 1300°C for 6 h (a). Zooming at main peak (b).

In order to investigate the effect of doping on A- and B- site in perovskite structures individually, samples with only doped A or B site were fabricated. The XRD patterns of theses sample are shown in Figure 3-3. Again, all the samples are single phase and there is no evidence of the second phase. In the case of A-site doping, since La^{3+} and Ca^{2+} ions have similar ionic radii, no Bragg shift will occur due to size difference, but their charge difference should compensate by gaining oxygen or changing the Mn ion charge. More investigation is in progress in order to identify the Mn ion charge in the samples by using XPS analysis.

On the other hand, in B-site doping the Fe^{3+} ions are replacing Mn^{4+} ions and the shortage of positive charge which formed in the lattice should be compensated by formation of oxygen vacancies ($V_{[O}^{2+}{}_{]}$). This may result in shifting the Bragg peaks to the left.

Finally, in the sample with A- and B- site doping the two processes which are mentioned above occurred at the same time in the sample. Take in mind that some of the excess or shortage of positive charge can be compensated by two ions which are incorporated in to the lattice. For instance, La^{3+} is replacing Ca^{2+} ions and brings positive charge to the lattice while Fe^{3+} is

replacing Mn^{4+} ions and brings a shortage of positive charge to the same lattice. It may possible that theses shortage and excess of positive charge compensate each other.

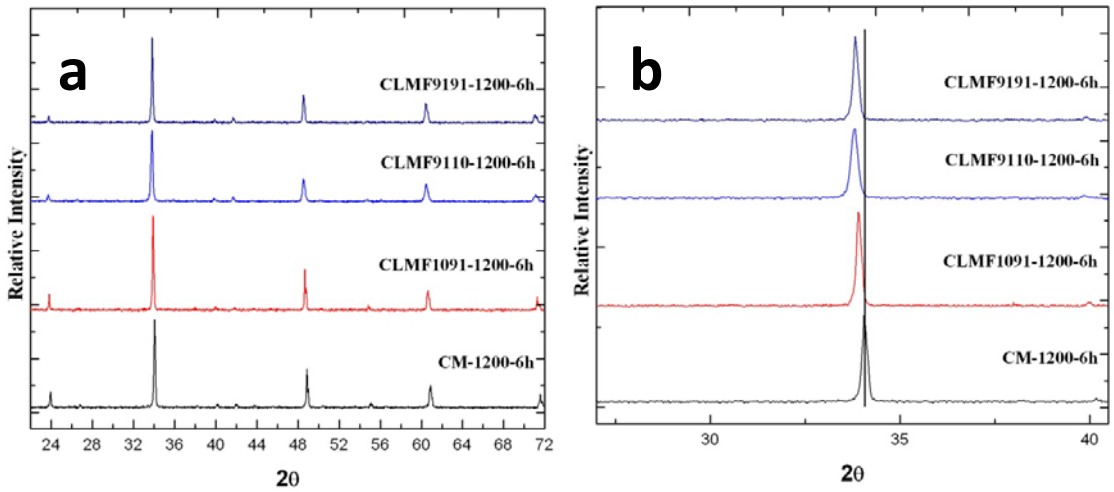

Figure 3-3 XRD patterns of CM, CLMF1091, CLMF9110 and CLMF9191 soaked at 1200°C for 6 h (a). Zooming at main peak (b).

As molybdenum oxide melts at 1100°C, it is not possible to heat treat the samples containing molybdenum oxide in their chemical formula at more than 1000°C. Therefore, the double perovskite samples are categorized in two main groups as follows: the first containing molybdenum and the second without molybdenum. The XRD patterns of fresh double perovskite samples for these two groups are shown in Figure 3-4. The molybdenum containing samples include SMgMo, CFMo, SFMo, and SMoCo soaked at 1000°C for 6 h, while the second group was heat treated at 1300°C for 6 hours. There is no evidence of any other residual phase, indicating that the stoichiometry of the precursor was correct for the production of the double perovskite structure in all cases.

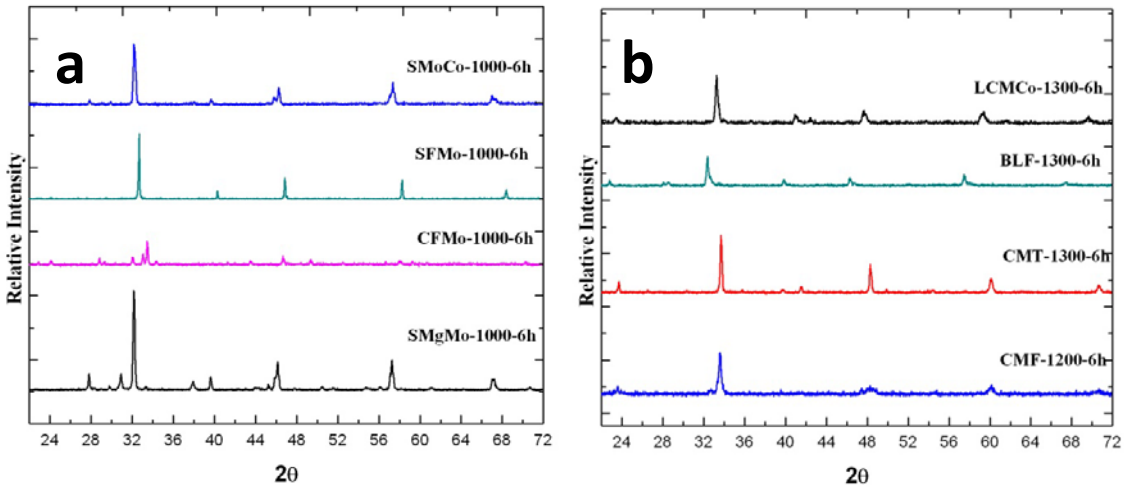

Figure 3-4 XRD patterns of fresh double perovskite samples for SMgMo, CFMo, SFMo, and SMoCo soaked at 1000°C for 6 h (a). Fresh double perovskite samples for CMF, CMT, BLF, and LCMCo soaked at 1300°C for 6 h (b).

2.1.2 TGA analysis

Figure 3-5 shows the oxygen capacity of the materials tests by a thermogravimetric analyzer, when cycled between air (20.8% O_2) and high-purity N_2. As seen, RO varies between 1.13 (for CLMT) and 2.17 (for CM). Doping at the A and B sites both obviously resulted in a decrease in oxygen capacity. Rormark et al.[110] have also reported a lower oxygen transfer capacity for $Ca0.9La0.1MnO_{3-\delta}$ compared to $CaMnO_{3-\delta}$.

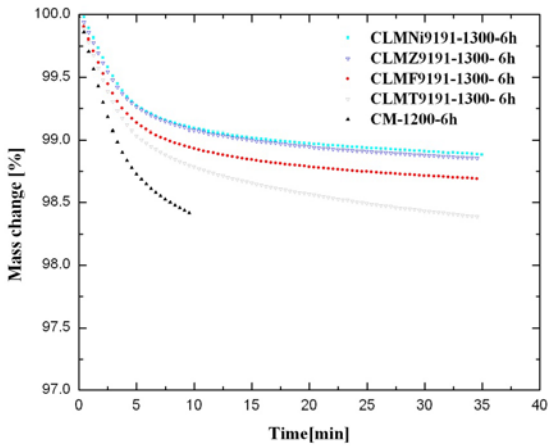

Figure 3-5 Oxygen capacity (RO) of the CLMNi, CLMZ, CLMT, and CLMF carriers during cycling between air (20.8% O_2) and high-purity inert gas (N_2) at 950 °C in a thermogravimetric analyzer.

Figure 3-6 shows the oxygen capacity of the materials for CLOU in samples which were doped on A and B sites individually. As it can be seen, doping the A site reduces the RO capacity of the perovskite more than does the doping of the B- site position. As discussed before in doping A- site case, there is an excess of positive charge that should be compensated either by gaining oxygen or changing the Mn ion valance charge. In the light of the first assumption the RO of the samples will decrease. As it can be seen in the sample with higher La content (CLMF6491) this decrease is obvious. On the other hand, when the B- site is substituted with high concentration of the Fe ions (CLMF9164) the RO decrease is significant. It seems the tendency of Mn ions to change their oxidation state from 4 to 2 is higher than Fe ions which change their oxidation state from 3 to 2. In this case, changing Mn ions with lower active ions such as iron will reduce the RO capacity of the samples (Figure 3-6).

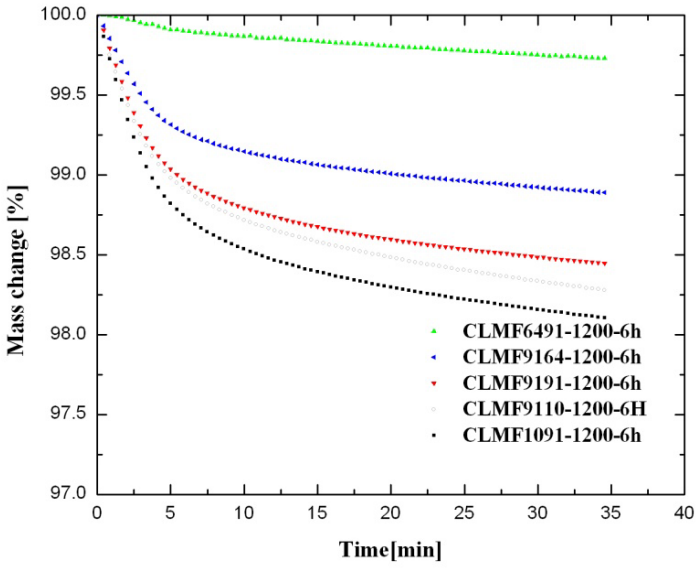

Figure 3-6 Oxygen capacity (RO) of the perovskite carriers investigated in this work during cycling between air (20.8% O_2) and high-purity inert gas (N_2) at 950 °C in a thermogravimetric analyzer.

Up to now, there are few reports on application of double perovskite material in chemical looping combustion. To the best of our knowledge, there is only one conference paper in 2012 [111] which uses this class of materials for chemical looping applications. They have claimed that the double perovskite $BaYMn_2O_{5+x}$ store and release oxygen rapidly and reversibly with unprecedented kinetics. Four double perovskite materials were synthesized and studied in the mentioned work, $BaLaFe_2O_{5+x}$, $BaLaCo_2O_{5+x}$, $BaYCo_2O_{5+x}$ and $BaYFe_2O_{5+x}$. Their result showed that Fe-containing compounds have proven to be the most interesting as they are stable for multiple adsorptions/desorption cycles with both nitrogen/air and hydrogen/air at multiple temperatures.

In order to select useful double perovskite materials for the CLOU process a screening process was performed. As discussed before, when double perovskite material is used either as an anode for solid oxide fuel cells or C_3H_8 combustion catalysis, the required properties for these applications are similar to properties which are needed for the materials that are used in chemical looping combustion. Several systems were chosen and listed in Table 3-1. The first step is to identify their capability to rapidly and reversibly store and release oxygen. For this reason all samples were tested with TGA analysis. The results are summarized in Figure 3-7. The results showed that only four groups of material can release and store oxygen in the desired way. These four systems are CMT, CMF, SFMo and BLF. It should be mentioned BLF was selected from the conference paper mentioned above using perovskite material for CLC application. The other three samples were chosen for mass production and further investigation, as they show higher RO numbers.

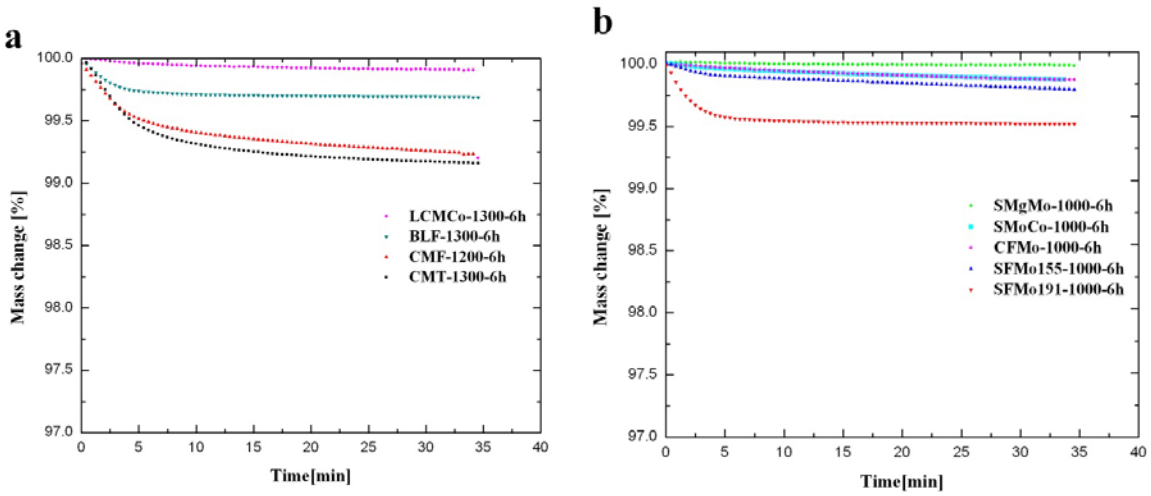

Figure 3-7 Oxygen capacity (RO) of the double perovskite carriers during cycling between air (20.8% O_2) and high-purity inert gas (N_2) at 950 °C in a thermogravimetric analyzer. first group containing molybdenum (a) and the second without molybdenum (b).

2.1.3 SEM images

The SEM images of the CLMF9191 fired at 1100, 1200 and 1300°C for 6 h are shown in Figure 3-8. A comparison between the three samples subjected to identical heat-treatment showed that the grain size increased as the heat treatment temperature rose to 1300°C. This was expected as increasing temperature led to an increase in the diffusion rate and as a result crystal growths of the samples took place.

Therefore, the surface area of the sample which was heat treated at higher temperature is less than the others and as a result this may affect the available surface area of the sample to the air or N_2 in TGA analysis. These could explain the decrease of RO in these samples (heat treated at 1300°C) in comparison with low temperature (1100°C) treated samples.

The SEM images of the CLMF9191 and CLMFT9191 soaked for 6 h at 1300°C are shown in Figure 3-9. The grain size of CLMFT9191 is lower than CLMF9191. Therefore, one reason for having lower RO could be the lower grain size in CLMT9191 samples.

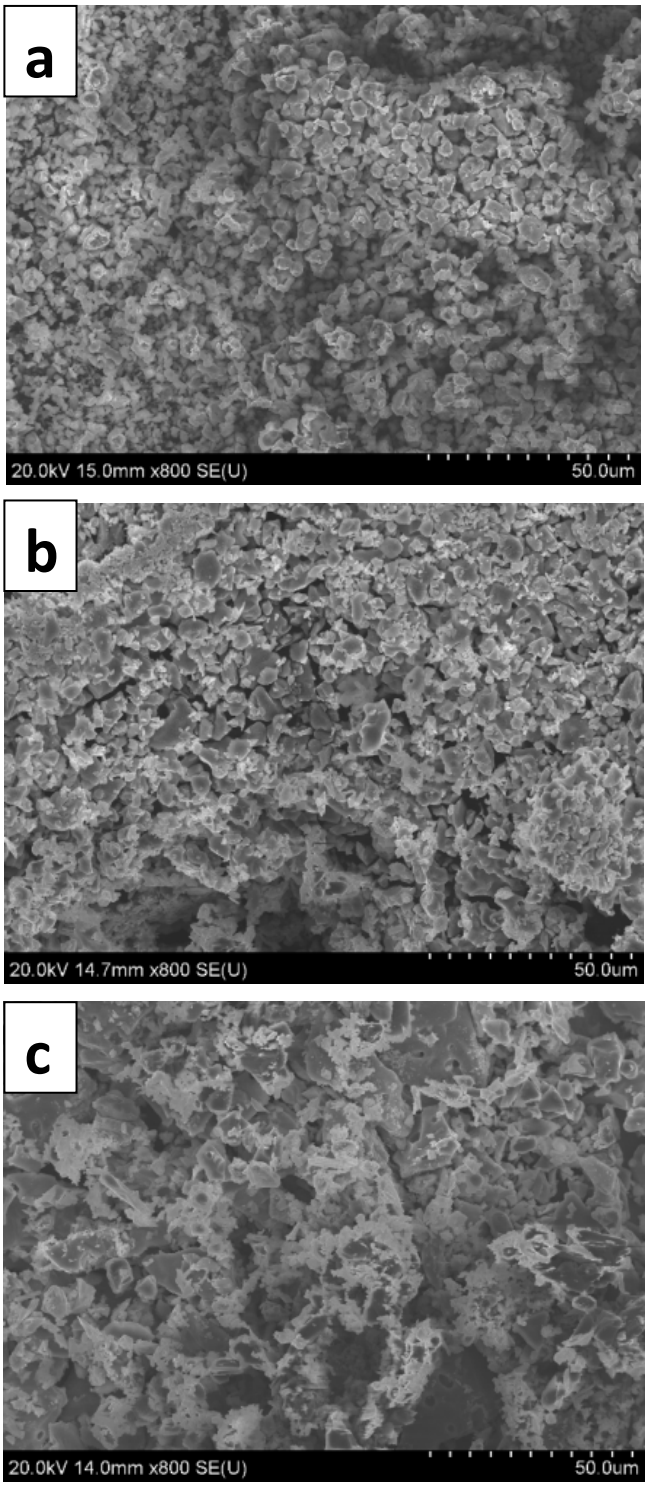

Figure 3-8 SEM images of the CLMF9191 soaked for 6 h at 1100(a), 1200(b) and 1300°C (c).

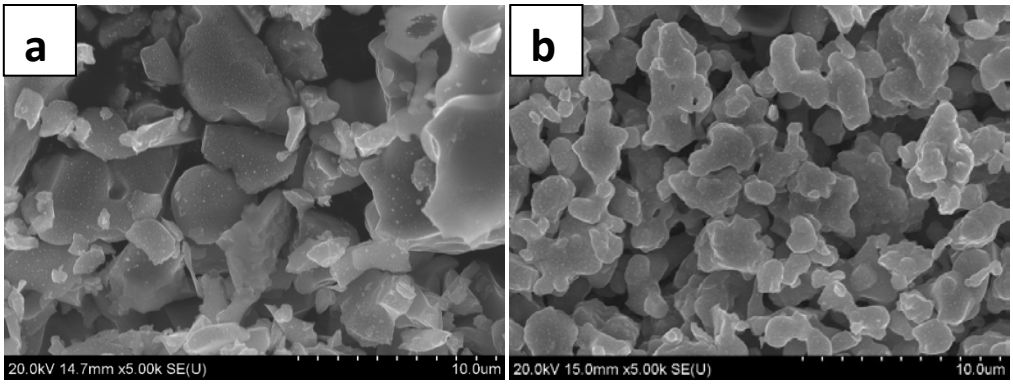

Figure 3-9 SEM images of the CLMF9191 (a) and CLMFT9191 (b) soaked for 6 h at 1300°C.

Figure 3-10 shows the SEM images of the samples which were on doped (a) or doped both on A and B sites simultaneously or on the A and B sites individually (c and d).

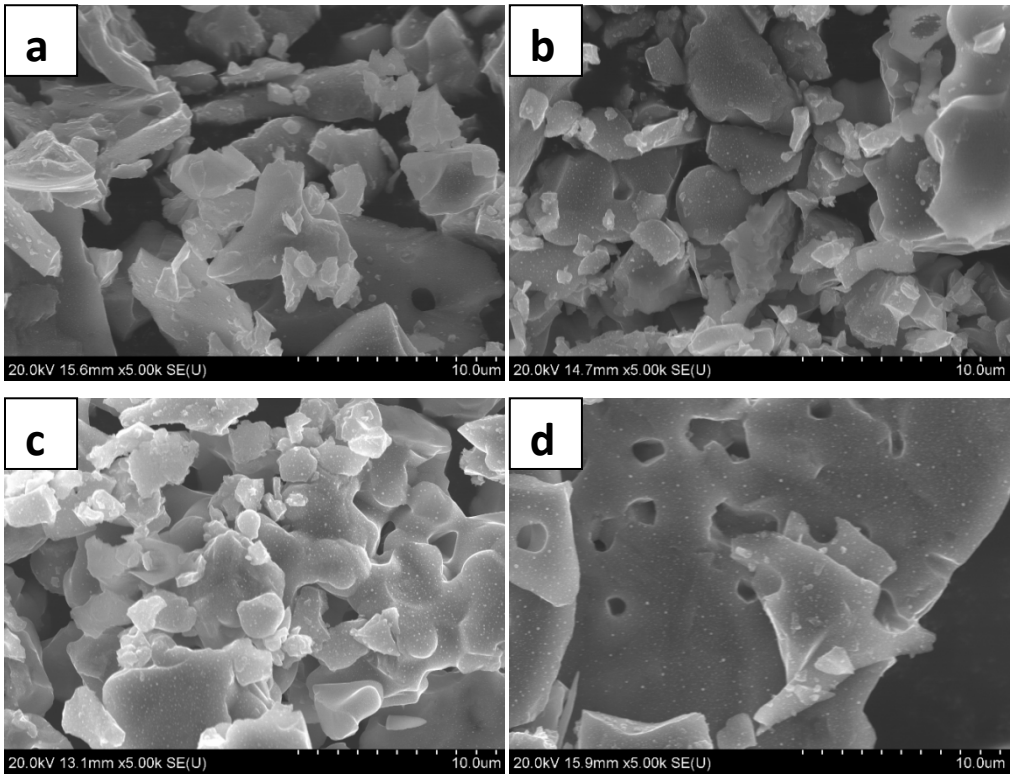

Figure 3-10 SEM images of the CM (a), CLMF9191 (b), CLMF9110 (c) and CLMF1091 (d) soaked for 6 h at 1200°C.

Except for the sample that was doped on B site, the grain size remained constant among the others. As iron oxide has a eutectoid with CaO and Mn_2O_3 individually, it seems the viscosity of the three mixtures decreased and grains started to join together to make bigger grains, as it can be seen from Figure 3-10-d. Introducing higher melting material like La_2O_3 to the mixture will decrease the viscosity and keep the samples grain size small (Figure 3-10-b and c)

EDS analyses of the samples were done after calibrating the detector with pure copper sample. The results are listed in Table 3-1, 3-2 and 3-3. The results are in agreement with the computational data, indicating that the stoichiometry of the precursor was correct for the production of the perovskite structure.

Table 3-1 EDS analysis of the samples (single perovskite) investigated in this work.

Sample ID	Element (Atomic %)							
	O K	Ca K	Mn K	La L	Fe K	Ti K	Zr L	Ni K
CM-1100-6h	72.23	13.87	13.9					
CM-1200-6h	71.31	14.51	14.18					
CLMF9191-1100-6h	59.49	18.36	18.22	1.77	2.16			
CLMF9191-1200-6h	49.03	22.11	23.48	2.24	3.14			
CLMF9191-1300-6h	59.91	18.13	18.13	1.68	2.15			
CLMT9191-1300-6h	66.12	16.16	14.49	0.92		2.3		
CLMZ9191-1300-6h	66.53	16.05	14.35	1.69			1.39	
CLNi9191-1300-6h	61.82	17.83	17.04	1.70				1.61

CLMF9110-1200-6h	66.39	15.87	16.32	1.42				
CLMF1091-1200-6h	55.69	21.93	20.1		2.27			
CLMF6491-1200-6h	63.09	11.27	16.57	7.06	2.02			
CLMF9164-1200-6h	60.96	17.98	11.67	1.75	7.64			

According to the single perovskite formula ($Ca_{0.9}La_{0.1}Mn_{0.9}B_{0.1}O_3$ where B is Fe, Ti, Zr or Ni) there should be at least 2 atomic% (at %) of the doping element in the samples. As it can be seen from Table 3-1 the atomic percent of these doping elements was near the expected values.

As discussed above in the case of A-site doping, as La^{3+} and Ca^{2+} ions have different charges the excess positive charge should be compensated by gaining oxygen or changing the Mn ions charge. Comparing the A- site (CLMF9110) and B- site (CLMF1091) doped samples in Table 3-1, it can be seen the oxygen amount in A- site doped sample is more than 10% of the B-site doped sample . As mentioned before, in the high iron concentration sample (CLMF9164), the excess of positive charge should be compensated by gaining oxygen. As a result, the oxygen content of the samples should be high which was confirmed by EDS analysis. Comparing CMLF9191-1300 and CLMT9191-1300 brings us to the point that the iron containing sample has lower oxygen content with respect to the Ti doped samples. This was expected, as the charge of Ti and Mn are the same, so there is no need to compensate the charges while in the iron doped sample compensation will be needed. Iron ions have 3+ charges while Mn ions have 4+. There is a shortage of positive charge that can be compensated by oxygen vacancy, which may result in a

decrease in oxygen content of the samples. It seems that a similar situation took place in the mentioned samples.

Table 3-2 EDS analysis of the samples (double perovskite Group 1) investigated in this work.

Sample ID	Element (Atomic %)							
	O K	Ca K	Mn K	Fe K	Sr L	Co K	Mg	Mo L
SFMo111	66.88			10.48	15.71			6.92
SFMo191	58.35			21.69	19.04			0.92
SMMo	76.33		7.45		12.47			3.75
SMgMoF	54.93			17.04	18.81		1.55	7.68
SMgMo	72.98				13.18		7.2	6.64
SMCoMo	63.36	-	9.99	-	17.55	9.10	-	
CFMo191	70.27	14.89		13.69				1.15

Table 3-3 EDS analysis of the samples (double perovskite Group 2) investigated in this work.

Sample ID	Element (Atomic %)							
	O K	Ca K	Mn K	La L	Fe K	Ti K	Ba L	Co K
CMF	71.7	14.38	4.30		9.61			
CMT	70.35	16.2	6.30			7.16		
BLF	48.79			10.34	29.35		11.53	
LCMCo	69.21	12.41	5.71	7.55				5.12

2.1.4 FT-IR

CM, CLMNi9191, CLMZ9191, CLMT9191 and CLMF9191 were also characterized by infrared spectroscopy (IR). The IR spectra of the products obtained from successive heat treated samples at 1200°C for 6 h are shown in Figure 3-11.

According to the literature, bands at ca. 600 and 400 cm^{-1} can be assigned to the M–O stretching and O–M–O deformation modes of $CaMnO_{3-\delta}$ [112].

Un-doped $CaMnO_3$ has two well resolved bands at 417 and 569 cm^{-1}. The former related to Mn-O vibration modes, while the latter correspond to O-Mn-O vibration modes. As it can be seen from the Figure 3-11, doping the B- site has a significant effect on the second vibration's mode. According to this figure, the peaks around 569 cm^{-1} subjected to change, while the $CaMnO_{3-\delta}$ doped with Ni, Zr, Fe and Ti ions, demonstrated successful doping process. This shift is more obvious in iron-doped samples, which may have resulted from more oxygen vacancies in this sample.

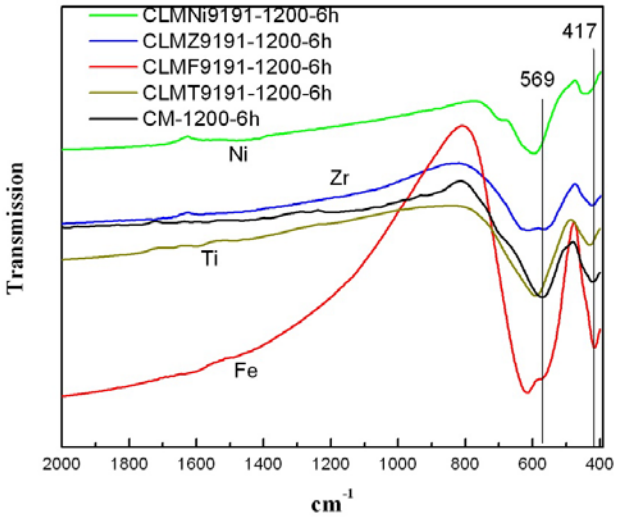

Figure 3-11 Infrared spectra of the products obtained from heat treated sample (CM, CLMT9191 and CLMF9191) soaked for 6 h at 1200°C.

In Figure 3-12 the IR spectra of the double and single perovskite of CMF and CMT, which obtained from successive heat treated samples at 1200°C for 6 h, are shown. In iron doped sample there is peak around 623, while in Ti doped sample the peak is around 587 cm^{-1}. There is no obvious change of the peak positions in single or double perovskite structure. This result was

expected as in single or double perovskite structure the vibration mode remains unchanged and as a result the FT-IR spectrum should remain constant.

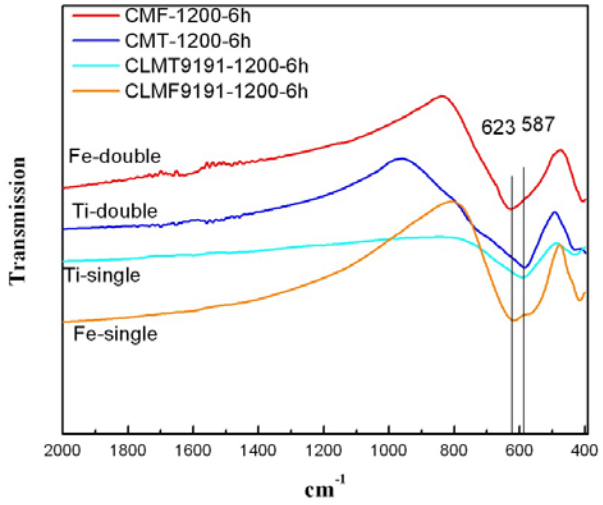

Figure 3-12 Infrared spectra of the products obtained from heat treated sample (CLMT9191, CLMF9191, CMF and CMT) soaked for 6 h at 1200°C.

2.2 Double perovskite

2.2.1 XRD diffraction analysis

As molybdenum oxide melts at 1100°C, it is not possible to heat treat the samples containing molybdenum oxide in their chemical formula at more than 1000°C. Therefore, the double perovskite samples are categorized in two main groups as follows: the first containing molybdenum and the second without molybdenum. The XRD patterns of fresh double perovskite samples for these two groups are shown in Figure 3-13. The molybdenum containing samples include SMgMo, CFMo, SFMo, and SMoCo soaked at 1000°C for 6 h, while the second group was heat treated at 1300°C for 6 hours. In Table 3-4 a summary of the phases and crystal structure data is presented.

In the second group, there is no evidence of any other residual phase, indicating that the stoichiometry of the precursor was correct for the production of the double perovskite structure in all cases.

On the other hand, in the first group, there is not a pure double perovskite structure and always there is a second phase formed inside the samples. This indicates that the reaction did not complete and as a result, a residual phase formed inside the samples. These could be due to two main reasons, first the reaction temperature is lower in this group and as result, and the diffusion process took place slower than the second group. Second, the reactivity of molybdenum oxide is lower than manganese oxide in solid reaction.

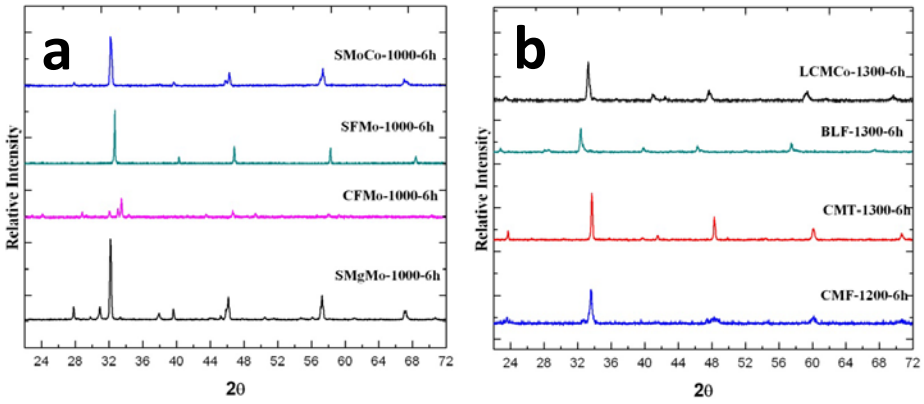

Figure 3-13 XRD patterns of fresh double perovskite samples for SMgMo, CFMo, SFMo, and SMoCo soaked at 1000°C for 6 h (a). Fresh double perovskite samples for CMF, CMT, BLF, and LCMCo soaked at 1300°C for 6 h (b).

Table 3-4 Summary of the phases and crystal structure data of double perovskite materials investigated in this work.

Group	code	Crystal phases	Symbol in graph	Wt%	Crystal Size (nm)	(Lattice constant)			Space group
						a	b	c	
One	SMoCo	$SrMoO_4$		12	41	5.39	5.39	12.02	tl41/a
		$Sr_2(CoMo)_6$		88	40	5.56	5.56	7.96	tl4/m
	SFMo21901	SrFeO2.75		100	93	10.96	7.75	5.48	ocmmm
	CFMo	$Ca_2(FeMo)O_6$		20	171	5.42	5.54	7.75	mp21/n
		MoO_3		80	171	7.76	7.39	10.65	mp21/c
	SMgMo	$Sr_2(MgMo)O_6$		86	41	5.57	5.57	7.93	tl4/m
		SrMoO4		14	40	5.39	5.39	12.05	tl41/a
Two	LCMCo	$(La_{0.65}Ca_{0.35})(Mn_{0.3}Co_{0.7})O_3$		100	30	5.4	7.64	5.43	opnma
	BLF	$(LaBa_2Fe_3O_{8.55})_{0.33}$		100	120	3.94	3.94	3.94	Cpm-3m
	CMT	$CaTi0.5Mn_{0.5}O_3$		100	57	5.35	7.55	5.33	opnma
	CMF	Ca_2FeMnO_5		100	33	5.35	15.04	5.48	opnma

2.2.2 TGA analysis

Figure 3-14 shows the oxygen capacity of the materials tests by a thermogravimetric analyzer, when cycled between air (20.8% O_2) and high-purity N_2. As seen, RO varies between 0.75 (for SFM) and 0.2 (for SFMo).

Up to now, there are few reports on application of double perovskite material in chemical looping combustion. To the best of our knowledge, there is only one conference paper in 2012 [111] which uses this class of materials for chemical looping applications. They have claimed that the double perovskite $BaYMn_2O_{5+x}$ store and release oxygen rapidly and reversibly with unprecedented kinetics. Four double perovskite materials were synthesized and studied in the mentioned work, $BaLaFe_2O_{5+x}$, $BaLaCo_2O_{5+x}$, $BaYCo_2O_{5+x}$ and $BaYFe_2O_{5+x}$. Their result showed that Fe-containing compounds have proven to be the most interesting as they are stable for multiple adsorptions/desorption cycles with both nitrogen/air and hydrogen/air at multiple temperatures.

In order to select useful double perovskite materials for the CLOU process a screening process was performed. As discussed before, when double perovskite material is used either as an anode for solid oxide fuel cells or C_3H_8 combustion catalysis, the required properties for these applications are similar to properties which are needed for the materials that are used in chemical looping combustion. Several systems were chosen and listed in Table 3-4. The first step is to identify their capability to rapidly and reversibly store and release oxygen. For this reason all samples were tested with TGA analysis. The results are summarized in Figure 3-14. The results showed that only four groups of material can release and store oxygen in the desired way. These four systems are CMT (XRD results showed that this system is single perovskite), CMF, SFMo and BLF. It should be mentioned BLF was selected from the conference paper mentioned above using perovskite material for CLC application.

Changing the crystal structure from single perovskite to double perovskite structure obviously resulted in a decrease in oxygen capacity. Although, in double perovskite structure there should be more oxygen in the structure as for phases showing brownmillerite, vacancy ordering long range magnetic order is always found[113]. It seems the structure cannot store/release rapidly a large amount of oxygen at moderate temperatures in a perfectly reversible manner. There few reports about double perovskite materials which have this capability [114-116].

In order to find double perovskite materials with higher oxygen capacity, three systems were chosen based on previous works and reports. These systems were Ca-Mn-Al-O, Sr (or Ca) - Fe-Mn-O and Sr-Fe-Mo-O. We have tried to modify these three groups by changing the composition, mainly the ratio between the two ions that goes in to B site position in double perovskite structure and the synthesis atmosphere.

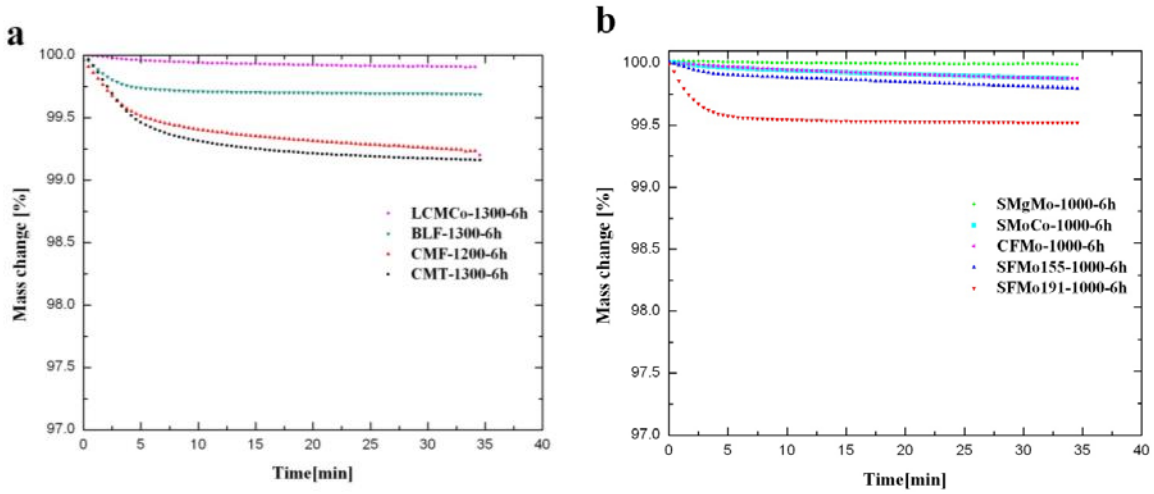

Figure 3-14 Oxygen capacity (RO) of the double perovskite carriers during cycling between air (20.8% O_2) and high-purity inert gas (N_2) at 950 °C in a thermogravimetric analyzer. First group containing molybdenum (a) and the second without molybdenum (b).

2.2.3 Sr-Fe-Mn-O

Ramezanipour et al.[117] synthesized Sr_2FeMnO_{5+y} under two different conditions, in air and in argon, both of which resulted in a cubic, Pm-3m, structure with no long-range ordering of

oxygen vacancies. The unit cell constants were reported to be a0 = 3.89328(1) Å for argon (y = 0.0) and a0 = 3.83075(3) Å for air (y = 0.5). Remarkably, $Sr_2FeMnO_{5.0}$ oxidizes spontaneously in air at room temperature. A neutron pair distribution function (NPDF) study of $Sr_2FeMnO_{5.0}$ (Ar) showed evidence for local, brownmillerite-like ordering of oxygen vacancies for short distances up to 5 Å. The L-edge XANES (L-edge X-ray absorption near-edge spectroscopy) study revealed that Mn is almost entirely in the 3+ state for $Sr_2FeMnO_{5.0}$(Ar), whereas Mn^{4+} is predominantly present for $Sr_2FeMnO_{5.5}$(air).

In addition, by comparing spectra for the reduced and oxidized forms they have mentioned, oxidation involves mainly conversion of Mn^{3+} to Mn^{4+} and not Fe^{3+} to Fe^{4+} [117].

The perovskite-based oxygen carrier particles, which were investigated in this group, are listed in Table 3-5. They were synthesized with the same procedure mentioned in Section 3.1. The calculation is to make 30 g batches of the final product in each case. The crystal size and RO capacity of the samples were also shown in this Table 3-5, which were calculated from XRD and TGA analysis respectively.

Table 3-5 Double perovskite formulations in Sr-Fe-Mn-O investigated in this work.

Sample **ID**	$SrCO_3$	Mn_2CO_3	Fe_2O_3	RO capacity	Crystal size (nm)
SF	10.50	-	19.50	0.50	-
SFMn-21901	9.90	0.8	19.3	0.38	-
SFMn-21505	7.6	3.6	18.8	0.60	-
SFMn-21010	4.9	7.1	18	0.75	304
SFMn-20515	2.35	10.2	17.45	0.60	114
SFMn-20119	0.46	17	12.54	0.60	170

Figure 3-15 shows the XRD pattern of the compositions listed in Table 3-5. As it can be seen from the figure, in all cases a single phase was formed. According to XRD data base, this phase was cubic structure of double perovskite $SrFeMnO_6$. According to the Bragg's law,

replacing iron with manganese results in shifting the Bragg's diffraction to the higher wavelength, as manganese ion size is smaller than iron. Shifting the Bragg diffraction to the right confirmed the formation of the solid solution between $SrMnO_3$ and $SrFeO_3$ oxides. As showed in the Figure 3-15-b, this shift is clearly observed, while the concentration of manganese oxide is increasing from 0 to 15 mol%.

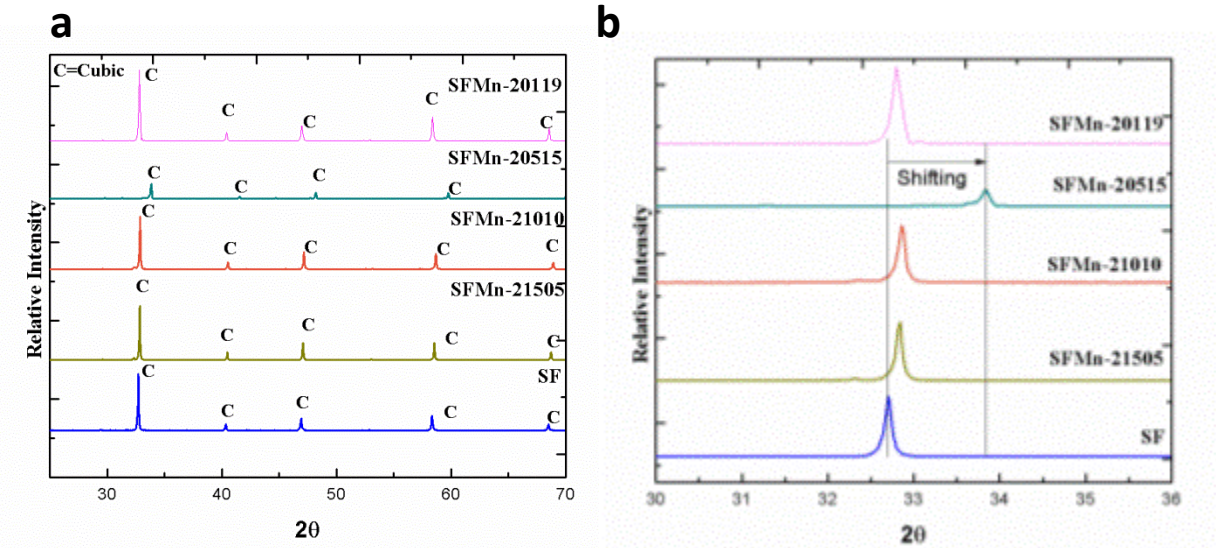

Figure 3-15 XRD patterns of fresh double perovskite samples for Sr-Fe-Mn-O system. , SF, SFMn-21505, SFMn-21010, SFMn-20515 and SFMn-20119 soaked at 1300°C for 6 h (a). Shifting the main XRD peak to the right as result of iron substitution (b).

The oxygen capacities of the materials for Sr-Fe-Mn-O samples were shown in Figure 3-16. As it can be seen, raising the manganese content to 10 mol. % will increase the RO capacity of the perovskite structure. It seems the mole ratio between Mn and Fe ions in the double perovskite structure plays an important role in the RO capacity of the perovskite structure and also has an optimum number in the RO capacity point of view. According to TGA analysis shown in Figure 3-16, the optimum ratio between Mn and Fe ions in double perovskite structure is one. This sample (SFMn-21010) has the highest RO capacity among the others which is 0.75.

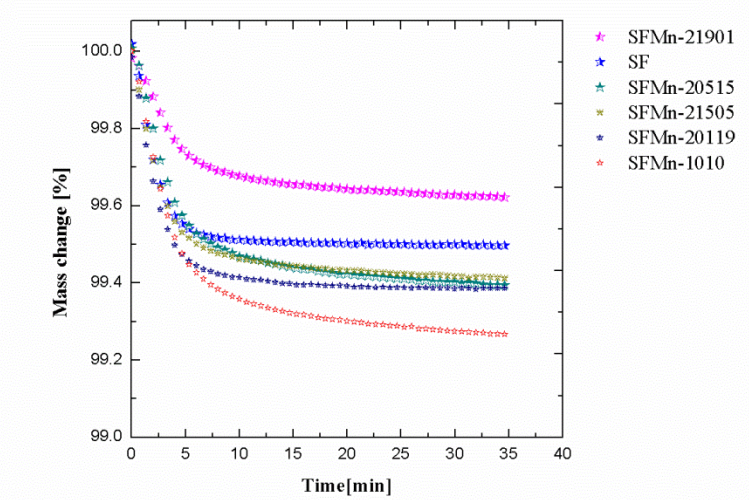

Figure 3-16 Oxygen capacity (RO) of the double perovskite carriers during cycling between air (20.8% O_2) and high-purity inert gas (N_2) at 950 °C in a thermogravimetric analyzer from samples in Sr-Fe-Mn-O system.

As Ramezani-pour et al. [117] mentioned, in a $Sr_2FeMnO_{5.5}$(air) Mn is almost entirely in the 4+ state for $Sr_2FeMnO_{5.5}$(air), whereas Fe^{3+} is predominantly present for this composition. In this case, reduction may convert Mn^{4+} to Mn^{3+} and not Fe^{3+} to Fe^{4+}, and the theoretical RO capacity will be 0.5.

However, if all of Fe^{3+} ions convert to Fe^{4+} during the reduction process, the theoretical RO capacity will be 1. Comparing these values with RO capacity of our samples, which are presented in Table 3-5, it can be concluded that in all cases this value is less than one. Therefore, the majority of Fe ions remain in Fe3+ during the reduction which is consistent with Ramezani pour et al. results.

2.2.4 Sr-Fe-Mo-O

The order perovskite structure can be represented as $A_2B'B''O_6$, in which the B' and B'' cations are alternately ordered in a rock-salt lattice, partly due to a large difference that they have in their charges or ionic radii. Sr2FeMoO6 is known to form in evacuated silica capsules or in a reducing atmosphere [118].

The formal valence states of Fe and Mo in SFMO are also not well known. The combined oxidation state for "Fe + Mo" is +8, and this could arise from a combination of $Fe^{2+}(3d^6)/Mo^{6+}(4d^0)$, or of $Fe^{3+}(3d)/Mo^{5+}(4d^1)$, or a mixture of these two. In the framework of a double exchange mechanism, there is the formation of a hybridized Fe–O–Mo band and electron itinerancy. The mechanism prevents a formal valence being ascribed to the Fe and Mo ions at any point in time. However, the average valences of the separate Mo and Fe ions will have a unique value. So far, it has not been possible to directly measure the values, although using a combination of X-ray absorption and photoemission spectroscopies, a ground state closer to $Fe^{3+}(3d^5)/Mo^{5+}(4d^1)$ than $Fe^{2+}(3d^6)/Mo^{6+}(4d^0)$ has been proposed by Moreno et al. In addition, Mossbauer data have suggested an $Fe^{2.5+}$ charge state.[119]

The double perovskite powders composition in Sr-Fe-Mo-O system are listed in Table 3-6. Again, they were prepared with same method mentioned in Section 3.1. The calculation was based on making 30g batches of the final product in each case. The crystal size and RO capacity of the samples were also shown in this table, which were calculated from XRD and TGA analysis respectively.

Table 3-6 Double perovskite formulations in Sr-Fe-Mn-O investigated in this work.

Sample **ID**	$SrCO_3$	MoO_3	Fe_2O_3	RO capacity	Crystal size (nm)
SF	10.50	-	19.50	0.50	
SMo	15.20	14.80	-	0.01	
SFMo-21010	17.10	8.3	4.6	0.21	100
SFMo-21901	19.20	0.90	9.90	0.46	

Figure 3-17 shows the formation of different phases such as $SrFeO_3$ (S), $SrMoO_4$ (SM) and $SrFeO_{3-x}$ (Sm where Mo dissolved in $SrFeO_3$) from the mixture of $SrCO_3$, Fe_2O_3, and MoO_3 at 1000°C in air. The diffraction angles of peaks of $SrFeO_{3-x}$ seem to shift to higher angles when molybdenum was added to the samples (SFMo-21901).

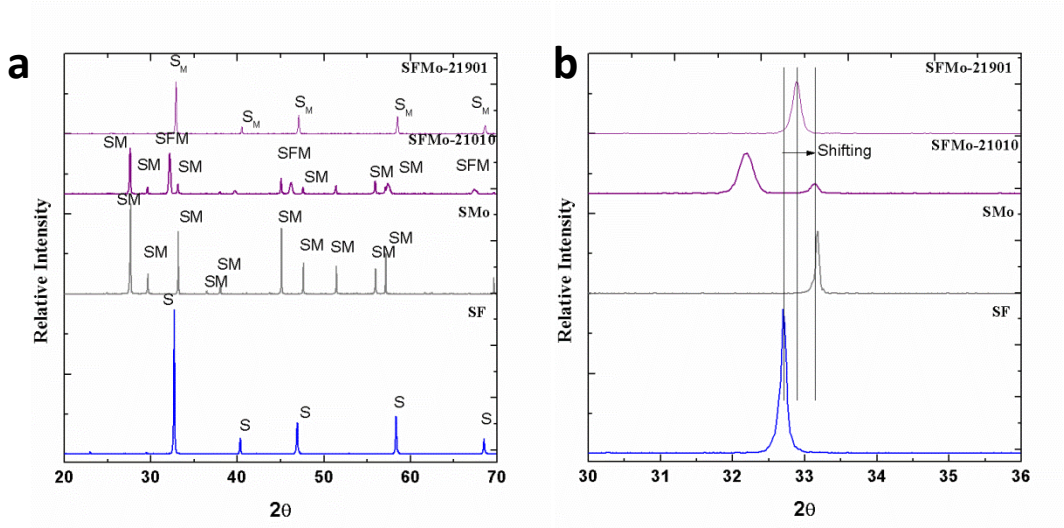

Figure 3-17 XRD patterns of fresh double perovskite samples for Sr-Fe-Mo-O system. , SF, SMo, SFMo-21010 and SFMo-21901 soaked at 1000°C for 6 h (a). Shifting the main XRD peak to the right as result of iron substitution (b).

There is a puzzling question existing in this formation scheme. If the Mo has diffused in the $SrFeO_{3-x}$, the diffraction angles of peaks of this new phase should shift to lower angles while interestingly they have shifted to higher angles[118]. This shift shows the substitution of Fe^{3+} (78.5 pm) by Mo^{5+} (75.0 pm) and indicates the formation of $SrFe_{1-x}Mo_xO_3$ phase. In this case, the Mo5+ ions are smaller than Fe^{3+} (78.5 pm) ions, and as a result the lattice will shrink and the Bragg diffractions shift to the higher wavelength. Increasing the molybdenum content lead to formation of another new phase called SFM ($Sr_2Fe_{1.5}Mo_{0.5}O_6$). In all cases, there is no sign of double perovskite compound which we are looking for. The reason for this is based on a fact that, in Sr_2FeMoO_6 the lattice would be distorted, when Mo was substituted for Fe in $Sr_2Fe_2O_{6-x}$.

However, if some oxygen could be removed, it would help Mo to dissolve in the lattice and form the Sr_2FeMoO_6, which explains why preparation of Sr_2FeMoO_6 needs to be in a reducing atmosphere [118].The oxygen capacities of the materials for Sr-Fe-Mo-O samples were shown in Figure 3-18. As it can be seen, increasing the molybdenum content to 10 and 50 mol.% decrease RO capacity of the perovskite structure.

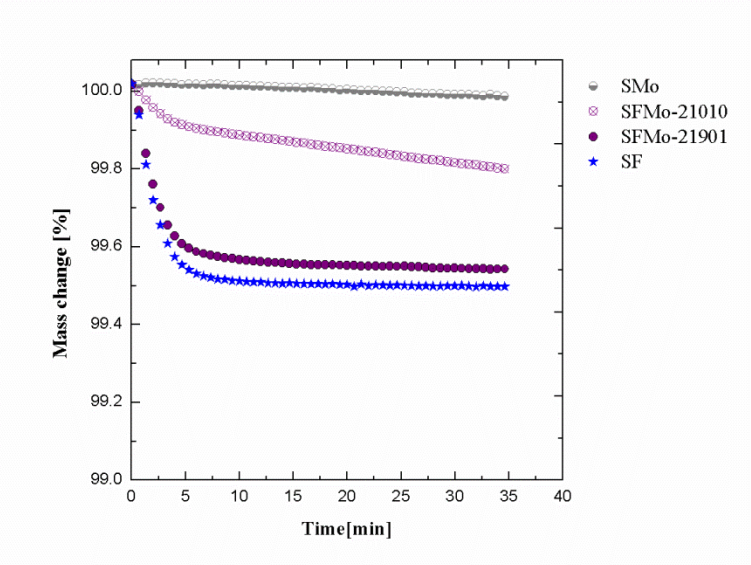

Figure 3-18 Oxygen capacity (RO) of the double perovskite carriers during cycling between air (20.8% O_2) and high-purity inert gas (N_2) at 950 °C in a thermogravimetric analyzer from samples in Sr-Fe-Mo-O system.

2.2.5 Ca-Mn-Al-O

The aim of this section was focused on an oxygen-deficient B-site ordered perovskite, Ca_2AlMnO_5. This oxide crystallizes in a Brownmillerite (BM) type with a general formula of $A_2B_2O_5$, in which tetrahedral BO_4 and octahedral BO_6 layers alternately stack with each other. In Ca_2AlMnO_5, divalent Ca is located at the perovskite A site, while trivalent Al and Mn at the B-site with a preferential formation of AlO_4 and MnO_6 polyhedral. The phase relation study on $Ca_2(Al_xMn_{1-x})2O_5$ showed a solid solution with respect to the Al/Mn ratio ranging $0.50 \leq x \leq 0.67$ in this oxide system [120]. The post annealing effect on oxygen nonstoichiometric was examined for Ca_2AlMnO_5 (i.e., x = 0.50) it appeared that the sample absorbs excess oxygen at 600 °C under a 30 MPa oxygen pressure to form $Ca_2AlMnO_{5.5}$ involving oxidation of Mn^{3+} to Mn^{4+}. Note that this result implies that oxygen storage capacity (OSC; the amount of excess oxygen being stored in the crystal lattice) of this oxide reaches 3.3 wt %, being even larger than the maximum value for the conventional OSM, CZ (2.8 wt %)[121]. Motohashi et al.[115] reported the oxygen storage capability of BM-type Ca_2 $(Al_xMn_{1-x})_2O_{5+\delta}$ $(0.50 \leq x \leq 0.67)$. They

have shown this oxide can store/ release a large amount of excess oxygen (OSC ~ 3.0 wt %) in response to small variations in temperature and the surrounding atmosphere in a highly reversible manner. The capacity and response of oxygen storage are found to be remarkable only in the vicinity of x = 0.50, that is, $Ca_2AlMnO_{5+\delta}$, and rapidly get worse as the Al content increases [115].

The double perovskite powders composition in Ca-Mn-Al-O system which were prepared with same method mentioned in Section 3.1 are listed in Table 3-7. The calculation was based on making 30g batches of the final product in each case. The crystal size and RO capacity of the samples were also shown in this table, which were calculated from XRD and TGA analysis respectively.

Table 3-7 Double perovskite formulations in Ca-Mn-Al-O investigated in this work.

Sample **ID**	$Ca(OH)_2$	$MnCO_3$	Al_2O_3	RO capacity	Crystal size (nm)
CMA-21010	14.15	11.00	4.85	0.17	231
CMA-21208	13.60	12.65	3.75	0.62	98
CMA-21307	13.34	13.34	3.22	0.81	69
CMA-21505	12.85	14.95	2.20	1.25	151
CMA-21901	12.00	17.60	0.40	1.60	500

With respect to the XRD result shown in Figure 3-19, the main phase after the heat treatment process in the samples having less than 0.45 mol. % Al_2O_3 in their composition is CaMnO3. As it can be seen from Figure 3-19-b, increasing the alumina content from 0.11 mol. % (CMA21901) to 0.45 mol% (CMA21505) results in shifting the main diffraction peak to the higher wavelength. This will confirm that the Mn ions are replaced by Al ions in the perovskite structure. As the sizes of Al ions are smaller than Mn ions, this replacement will shrink the lattice and the diffraction peaks will shift to the right due to the Bragg Law. In the samples with higher than 0.77 mol% alumina content in their composition beside $CaMnO_3$, a new phase called

Ca_2MnAlO_5 was crystallized. Finally, in the sample having equal amount of (mol %) Al_2O_3 and Mn_2O_3 in its composition (CMA21010) $Ca_2MnAlO_{5.5}$ was also formed during the heat treatment process.

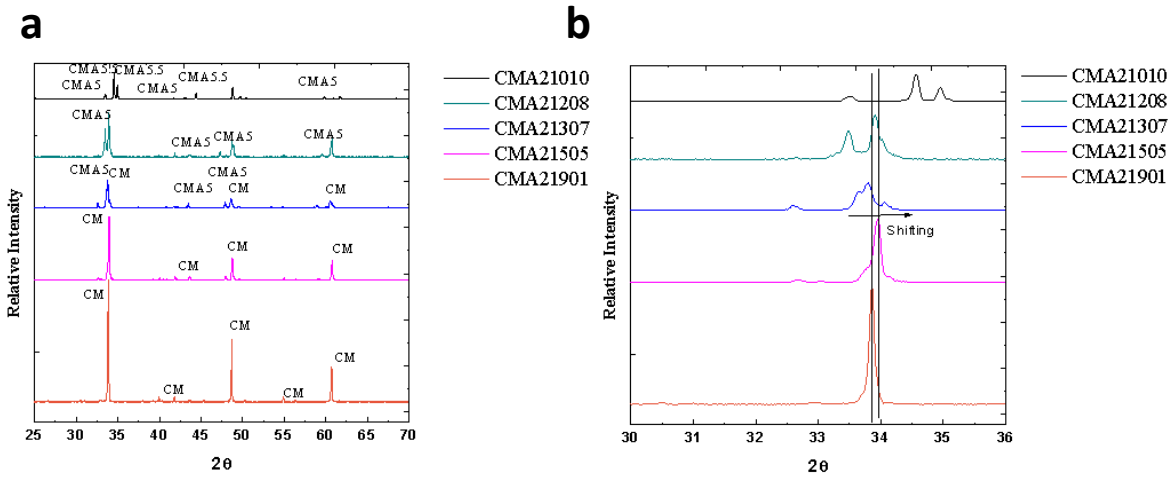

Figure 3-19 XRD patterns of fresh double perovskite samples for Ca-Mn-Al-O system. , CMA-21901, CMA-21505, CMA-21307, CMA-21208 and CMA-21010 soaked at 1300°C for 6 h (a). Shifting the main XRD peak to the right as result of manganese substitution (b).

The oxygen capacities of the materials for Ca-Mn-Al-O samples were plotted Figure 3-20. As it can be seen, increasing the Alumina content decreases the RO capacity of the perovskite structure from 1.60 to 0.17. According to XRD results, increasing the alumina content converts the $CaMnO_3$ phase to high alumina content phases such as $Ca_2MnAlO_{5.5}$ and Ca2MnAlO5. This decrease leads to a reduction in the RO capacity. Based on the intensity of the XRD results, it seems the amount of the perovskite phase is decreased as well. This was not surprising, as the samples were heat treated in air, and as a result the formation of double perovskite structure is hindered by way of discussed above.

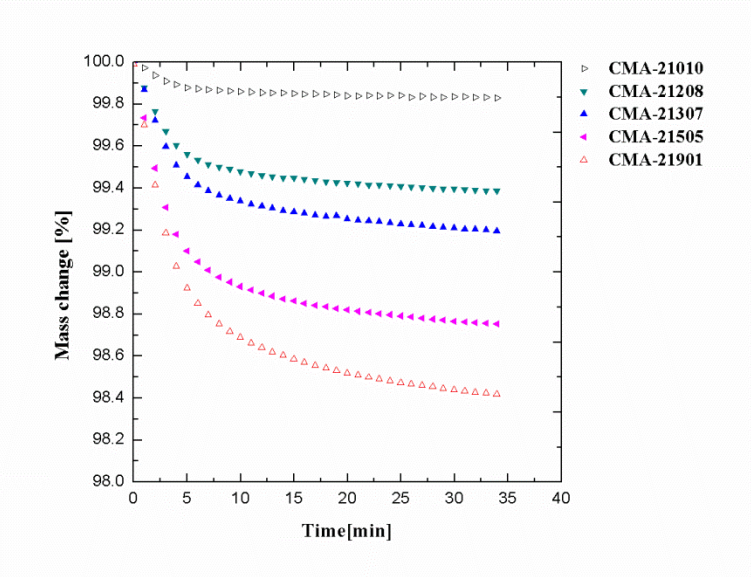

Figure 3-20 Oxygen capacity (RO) of the double perovskite carriers during cycling between air (20.8% O_2) and high-purity inert gas (N_2) at 950 °C in a thermogravimetric analyzer from samples in Ca-Mn-Al-O system.

2.2.6 SEM images

The SEM images of the SFMo-21901, SFMo-21010, CFMo and CMA-21010 are shown in Figure 3-21. A comparison between the three molybdenum samples showed that the grain size and shape is almost same. This was expected as all samples heat treated in the same temperature and with same procedure. The grain size for CMA-21010 is bigger than the others because this sample was heat treated at higher temperature (1300°C) and this a fact that increasing temperature led to an increase in the diffusion rate and as a result crystal growths of the samples.

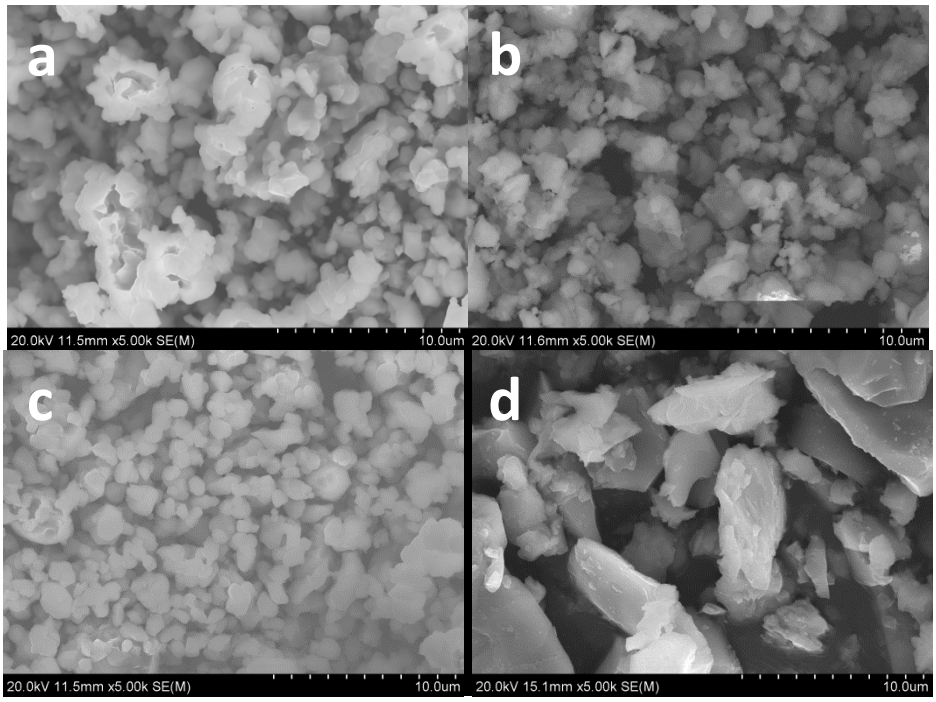

Figure 3-21 SEM images of the SFMo-21901 (a), SFMo-21010 (b), CFMo (c) and CMA-21010 (d).

EDS analyses of the samples were done after calibrating the detector with pure copper sample. The results are listed in Table 3-8 and 3-9. The results are in agreement with the computational data, indicating that the stoichiometry of the precursor was correct for the production of the perovskite structure.

Table 3-8 EDS analysis of the samples (double perovskite Group 1) investigated in this work.

Sample ID	Element (Atomic %)							
	O K	Ca K	Mn K	Fe K	Sr L	Co K	Mg	Mo L
SFMo111	66.88			10.48	15.71			6.92
SFMo191	58.35			21.69	19.04			0.92
SMMo	76.33		7.45		12.47			3.75
SMgMoF	54.93			17.04	18.81		1.55	7.68
SMgMo	72.98				13.18		7.2	6.64
SMCoMo	63.36	-	9.99	-	17.55	9.10	-	
CFMo191	70.27	14.89		13.69				1.15

Table 3-9 EDS analysis of the samples (double perovskite Group 2) investigated in this work.

Sample ID	Element (Atomic %)							
	O K	Ca K	Mn K	La L	Fe K	Ti K	Ba L	Co K
CMF	71.7	14.38	4.30		9.61			
CMT	70.35	16.2	6.30			7.16		
BLF	48.79			10.34	29.35		11.53	
LCMCo	69.21	12.41	5.71	7.55				5.12

2.2.7 FT-IR

In Figure 3-22 the IR spectra of the double and single perovskite of CMF and CMT, which obtained from successive heat treated samples at 1200°C for 6 h, are shown. In iron doped sample there is peak around 623, while in Ti doped sample the peak is around 587 cm-1.

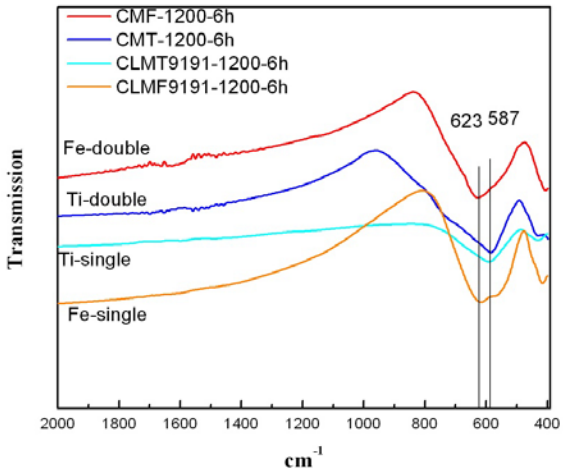

Figure 3-22 Infrared spectra of the products obtained from heat treated sample (CLMT9191, CLMF9191, CMF and CMT) soaked for 6 h at 1200°C.

There is no obvious change of the peak positions in single or double perovskite structure. This result was expected as in single or double perovskite structure the vibration mode remains unchanged and as a result the FT-IR spectrum should remain constant.

2.3 Process the powder to endow proper rheology followed by net-shaping by extrusion (Optimizing the synthesis condition-Part 1)

In order to define the synthesis conditions (choice of precursor, pH, mixing time and dispersant concentration), sets of experiments were employed. The optimum condition for pH, ball milling time and dispersant concentration were established by zeta potential, TGA and XRD pattern of the samples.

The effect of ball milling on Zeta potential is shown in Figure 3-23.

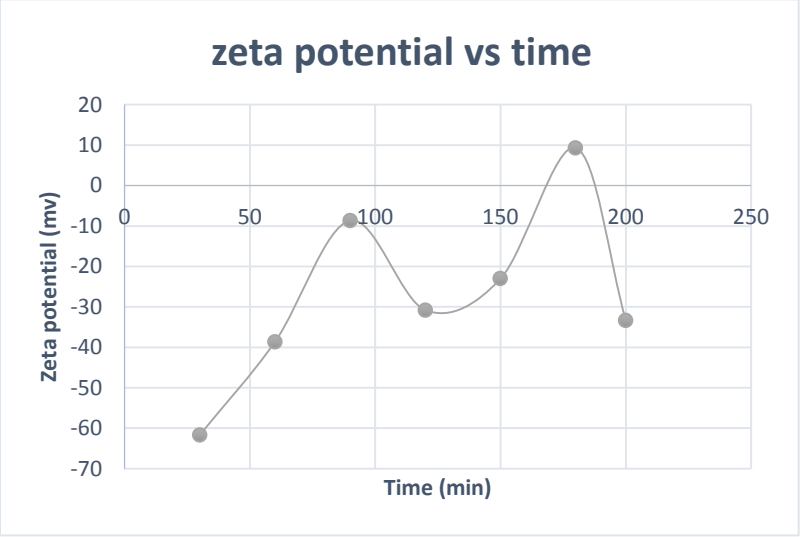

Figure 3-23 Diagram showing effect of time on zeta potential

At first, particles in the slurry have started the wetting stage. In this stage, forces between particles start to break down. The next step is the separation of the particles and the last stage is stabilization. The aim here is to make the particles as disperse as possible in the mixture.

Second, sets of experiments were conducted to evaluate the effect of pH on dispersion of the particles. The slurry was mixed for 3 hours and then a sample was taken out for pH measurement. The primary pH of the mixture was basic (pH=12). Since we have $Ca(OH)_2$ in the mixture, OH- will be released, and as a result the environment will become basic. So citric acid was added to the slurry for understanding the effect of pH on dispersion of particles and zeta

potential of the slurry. Each time that a specific amount of citric acid was added to the mixture, 20 minute intervals were given to the slurry to be mixed on the jar mill. The results are shown in Figure 3-24.

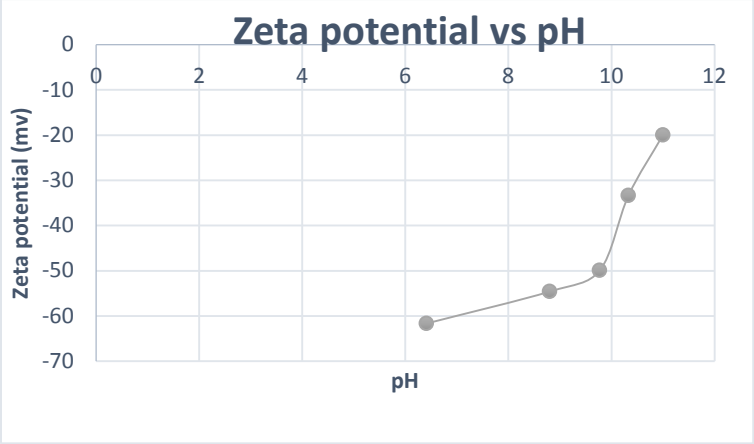

Figure 3-24 Effect of pH on zeta potential on mixed slurry

In a basic environment, because the zeta potential is negative, adding an acid to the mixture will neutralize the negative charges to a point where surface charges are neutralized. Then, adding additional acid will make surface charge positive, and zeta potential will become positive as well [122].

Electrostatic stabilization exists between particles which have sufficient surface charge and repel one another. For achieving a better dispersion, a polymer often will be introduced to the system as a dispersant. In the next step, steric stabilization occurs as a result of adsorption of the polymer to the particles surface. When both surface charge and adsorbed polymer coexist, the mechanism is referred to as electrosteric which is a better stabilization mechanism. As a result, by adding a dispersant one must achieve a better dispersion of particles in the slurry [123].

Another set of conducted experiments were done to evaluate the effect of dispersant on dispersion of particles. In the next step, ammonium polycarbonate (NH_4PAA) was added to the

slurry in different intervals (every half an hour). In intervals 0.05g, 0.3g, 2g of dispersant was added to the slurry respectively. The pH of the mixture was set to 7 after adding specific amounts of dispersant. The results are shown in Figure 3-25.

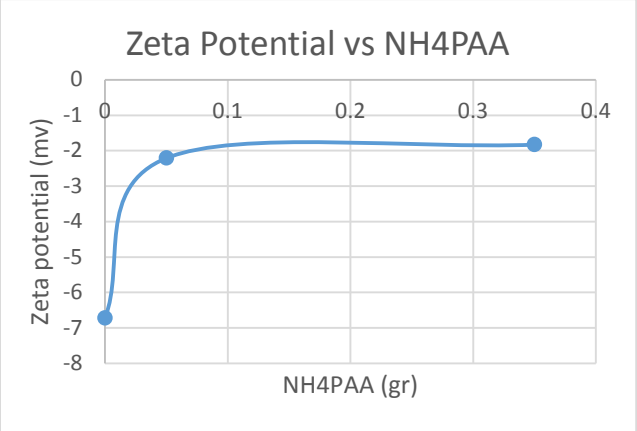

Figure 3-25 Changes of zeta potential with change in the amount of dispersant. Dispersant was added in amounts of 0.05gr, 0.3gr and 2 g to the slurry

A visual inspection also was done considering pH and dispersant as changing factors. Samples were taken in basic and acidic environments with varying amounts of dispersant. Some pictures were taken from the samples which are shown in Figures 3-26 and 3-27.

(a)

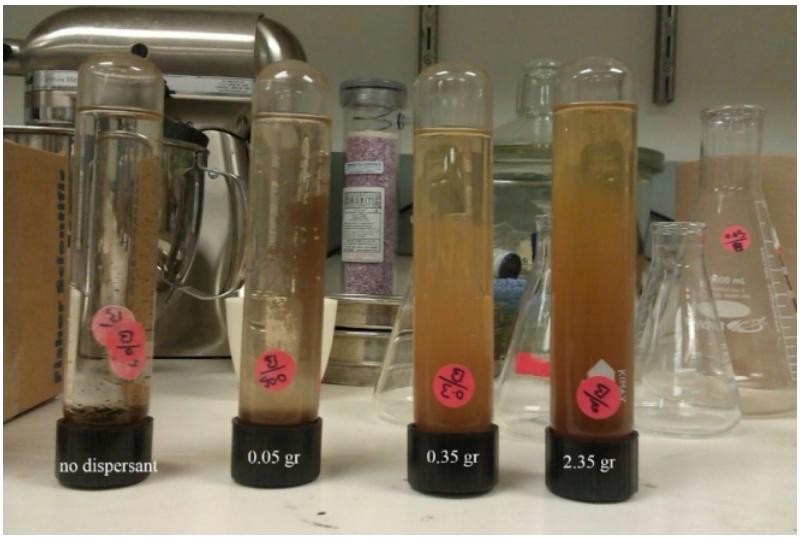

(b)

Figure 3-26 samples taken from the slurry in basic environment, amount of NH_4PAA is increasing from left to right 0 g, 0.05 g, 0.35 g, and 2.35 g respectively (a) shortly after measuring zeta potential, (b) after 2 days

(a)

(b)

Figure 3-27 samples taken from slurry in acidic environment, the amount of dispersant is increasing from left to right0 g, 0.05 g, 0.35 g, and 2.35 g respectively, (a) shortly after measuring zeta potential, (b) after 2 days

As it can be seen from the figures above, the basic environment is a better environment for particles to be dispersed. It can clearly be seen that the acidic environment cannot be a stable environment since almost all particles in the slurry settled down after two days, while samples in the basic environment and especially the ones with higher amounts of dispersant (CLMF9191-NH4PAA.2%) only settled down in small amounts.

In order to investigate the effect of precursor size on the perovskite oxygen capacity and structure, Iron (III) oxide, industrial, NanoArc® from Alfa Aesar was used as a precursor (CLMF9191-nano iron) in comparison with iron macro powders (CLMF9191) that have been used previously.

As it can be seen from Figure 3-28, the main crystal phase for the three samples from CLMF family remains unchanged. The only difference is the diffraction intensity, which is related to the crystallinity of the samples. The crystallinity of the nano iron containing sample is higher than the others, this is due to the higher surface area in the iron nano containing samples

which then led to better reactivity of the powders, and as a result higher crystallinity was achieved.

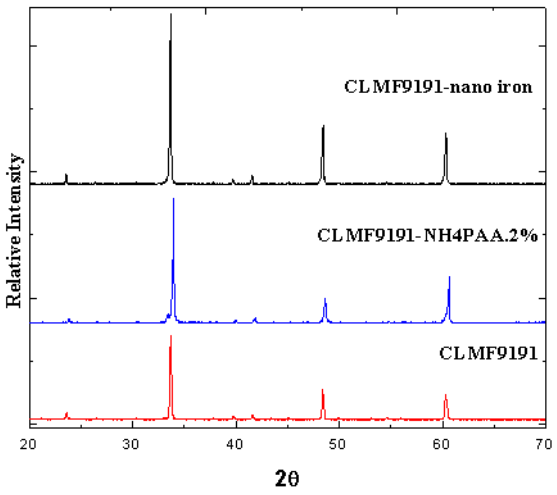

Figure 3-28 XRD patterns of fresh double perovskite samples for CLMF9191, CLMF9191-NH_4PAA and CLMF9191-nano iron soaked at 1300°C for 6 h

In Figure 3-29, the RO of the three samples discussed above is shown. The RO capacity did not change noticeably. This behavior was expected as the main phase remains unchanged with respect to the XRD result.

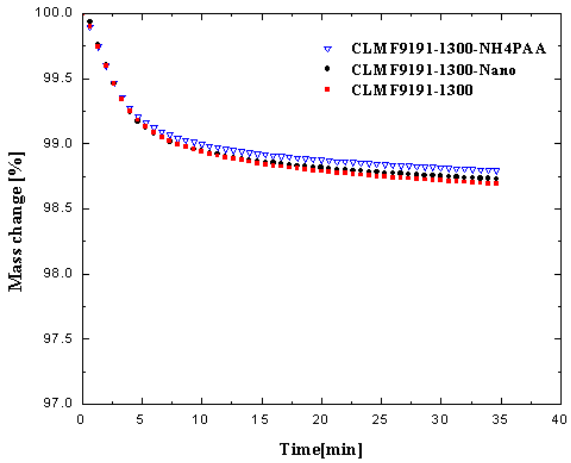

Figure 3-29 Oxygen capacity (RO) of the double perovskite carriers during cycling between air (20.8% O_2) and high-purity inert gas (N_2) at 950 °C in a thermogravimetric analyzer from samples in CLMF9191 system.

The results indicate that using nano material as a precursor could increases the crystallinity of the samples. In addition, while using 2 wt% dispersant (NH_4PAA) did not change the crystallinity and RO capacity of the samples intensely. We will suggest to use dispersant when large scale slurries are in mind.

2.4 Process the powder to endow proper rheology followed by net-shaping by extrusion (Optimizing the synthesis condition-Part 2)

2.4.1 X-ray diffraction analysis (XRD):

Figure 3-30 and Figure 3-31 show the XRD pattern of the compositions listed in Table 2-1. As it can be seen from the figures, in all cases, a single phase was formed. According to XRD database, this phase has calcium manganate ($CaMnO_3$) perovskite structure which is doped with lanthanum at A site and iron, titanium, aluminum, or zirconium ions at B site.

In Figure 3-30, the XRD pattern of CLMF composition which was prepared with different extrusion condition according to Table 2-1 is shown. As expected, all the patterns looked very similar to each other without any evidence of another residual phase. There is a slight shift in the ext-0 sample which is due to its high oxygen stoichiometry difference respect to other samples.

In the case of A- and B-site-doped particles (CLMT, CLMF, and CLMZ), the XRD patterns looked very similar to each other in all cases, without any evidence of another residual phase, indicating that the stoichiometry of the precursor was correct for the production of the perovskite structure.

Besides the ionic radii requirements, another condition to be fulfilled is electroneutrality, that is the sum of charges of A and B equals the total charge of oxygen anions. This is achieved by means of suitable charge distribution of the form $A^{1+}B^{5+}O_3$, $A^{2+}B^{4+}O_3$, or $A^{3+}B^{3+}O_3$. In addition to this, partial substitution of A and B ions is allowed, thus yielding an excess of compounds while preserving the perovskite structure. However, deficiencies of cations at the A-

or B-sites or of oxygen anions are common, which results in defective perovskites. Oxygen vacancies are more common than those involving cationic vacancies[109]. In Figure 3-30-b, the main peak shifts of the XRD patterns are shown. In reality instead of manganese ions (Mn^{4+}), iron or aluminum ions (Fe^{3+}, Al^{3+}) incorporate into perovskite lattice and carry a shortage of positive charge into the lattice and this should be compensated. Compensation can be affected by formation of oxygen vacancies ($V[O^{2+}]$). Formation of oxygen vacancies will expand the lattice and then lead to shifting the Bragg reflections to the left.

On the other side, replacing ions with different sizes will result in lattice expansion or contraction. The order of ionic size of ions which were used in this study is as follows: Mn^{4+} <Fe^{3+}< Al^{3+} <Ti^{4+} <Zr^{4+}. As it can be seen, zirconium ions are bigger than the others which may result in higher lattice distortion with respect to the others and lead to Bragg shift to the left as it can be seen in Figure 3-30-b.

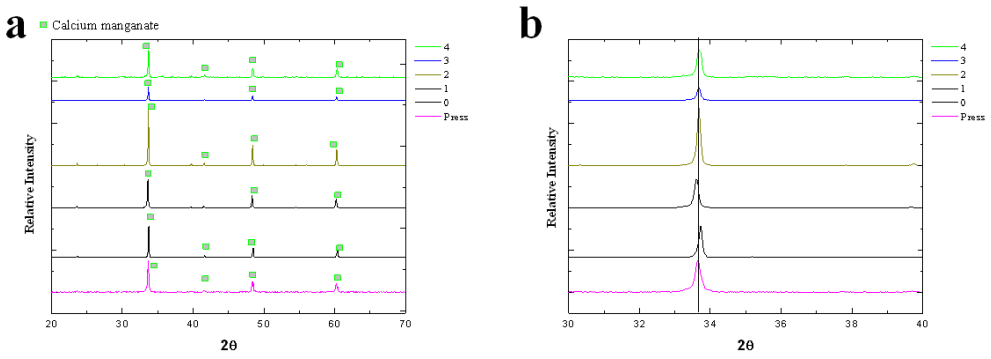

Figure 3-30 XRD patterns of fresh samples for CLMF with different starch content according to Table 2-1 soaked at 1300°C for 6 h (a). Zooming at main peak (b).

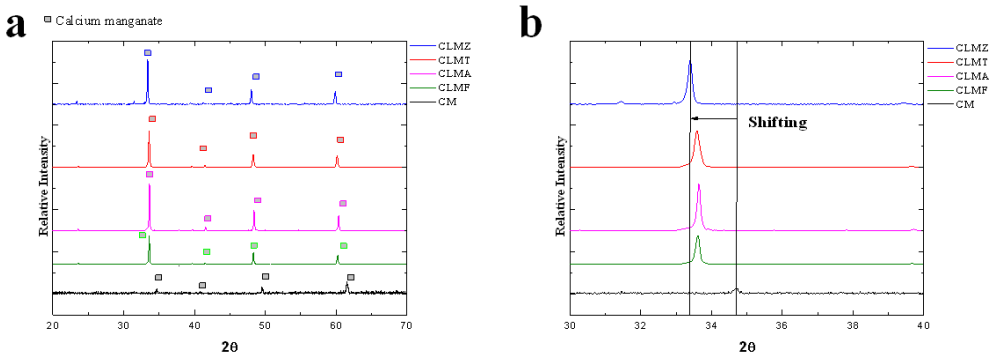

Figure 3-31 XRD patterns of fresh samples for CM, CLMF, CLMA, CLMT, and CLMZ soaked at 1300°C for 6 h (a). Zooming at main peak (b).

2.4.2 Scanning electron microscope analysis (SEM):

The SEM images of CLMF fired at 1300°C for 6 h with different extrude conditions (See Table 2-2) shown in Figure 3-32. A comparison between the six samples subjected to identical extrusion condition showed that the starch amount plays an important role in the porosity of the samples. Comparing the sample that had not any starch in its composition with the others indicates that starch acts as a pore-forming agent successfully.

According to the SEM images, the amount of starch in the paste composition has an optimum value. As it can be seen from Figure 3-32 and d, above 2.4 wt % starch in the composition results in pores closing inside the structure. This is due to the exothermic reaction of burnout process of starch.

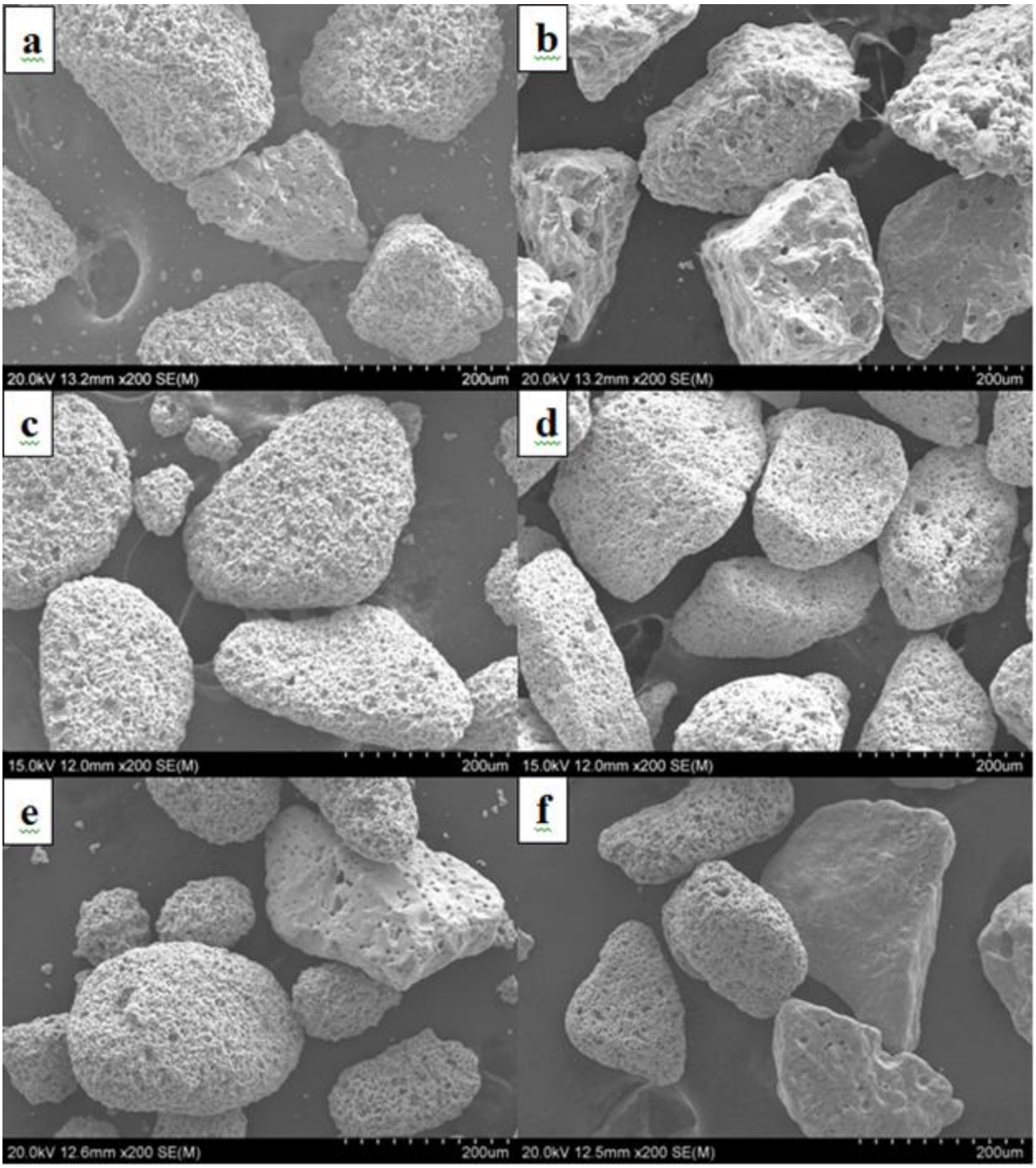

Figure 3-32 SEM images of the CLMF with different starch content according to Table 2-2 soaked for 6 h at 1300 press (a), 0 (b), 1 (c), 2 (d), 3 (e) and 4 (f).

As the amount of starch increases in the samples, the total energy that will be released during the burn out process will increase. As a result, the samples may reach their surface melting point and melt locally. This will close the pores that are already formed during the

burnout process (Figure 3-32-e and f). Therefore, the surface area of the sample which has a higher starch amount in its composition is less than the other samples. As a result, this may affect the available surface area of the sample to the air or N_2 in TGA analysis. This could explain the decrease of oxygen capacity (RO) in these samples (heat treated at 1300°C) in comparison with low containing starch samples.

The SEM images of the CLMF with optimum amount of starch (1.2 %wt.) soaked for 6 h at 1300°C is shown in Figure 3-33. As it can be seen, a well porous structure was formed.

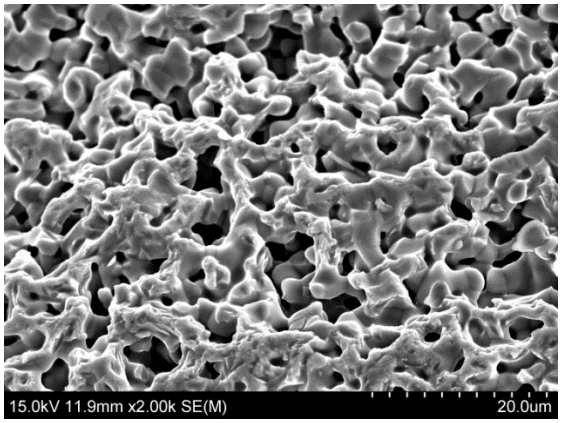

Figure 3-33 SEM images of the CLMF (optimum extrusion condition) soaked for 6 h at 1300°C.

In order to check the proposed slurry formula for other doping systems, a paste series of doped perovskite-type oxygen carrier particles ($Ca_xLa_{1-x}Mn_{1-y}B_yO_{3-\delta}$ (B_{site} = Ti, Al, or Zr) were prepared with the optimized formula. The SEM images (Figure 3-34) revealed that the microstructure remains unchanged in the five systems. This indicates that the formulation was suitable for the other four systems as well.

EDS analyses of the samples were done after calibrating the detector with a pure copper sample. The results are listed in Table 3-10. The results are in agreement with the computational data, indicating that the stoichiometry of the precursor was correct for the production of the perovskite structure. According to the single perovskite formula ($Ca_{0.9}La_{0.1}Mn_{0.9}B_{0.1}O_3$ where B

is Fe, Ti, Zr or Al), there should be at least 2 at% of the doping element in the samples. As it can be seen from Table 3-10, the atomic percent of these doping elements was near the expected values.

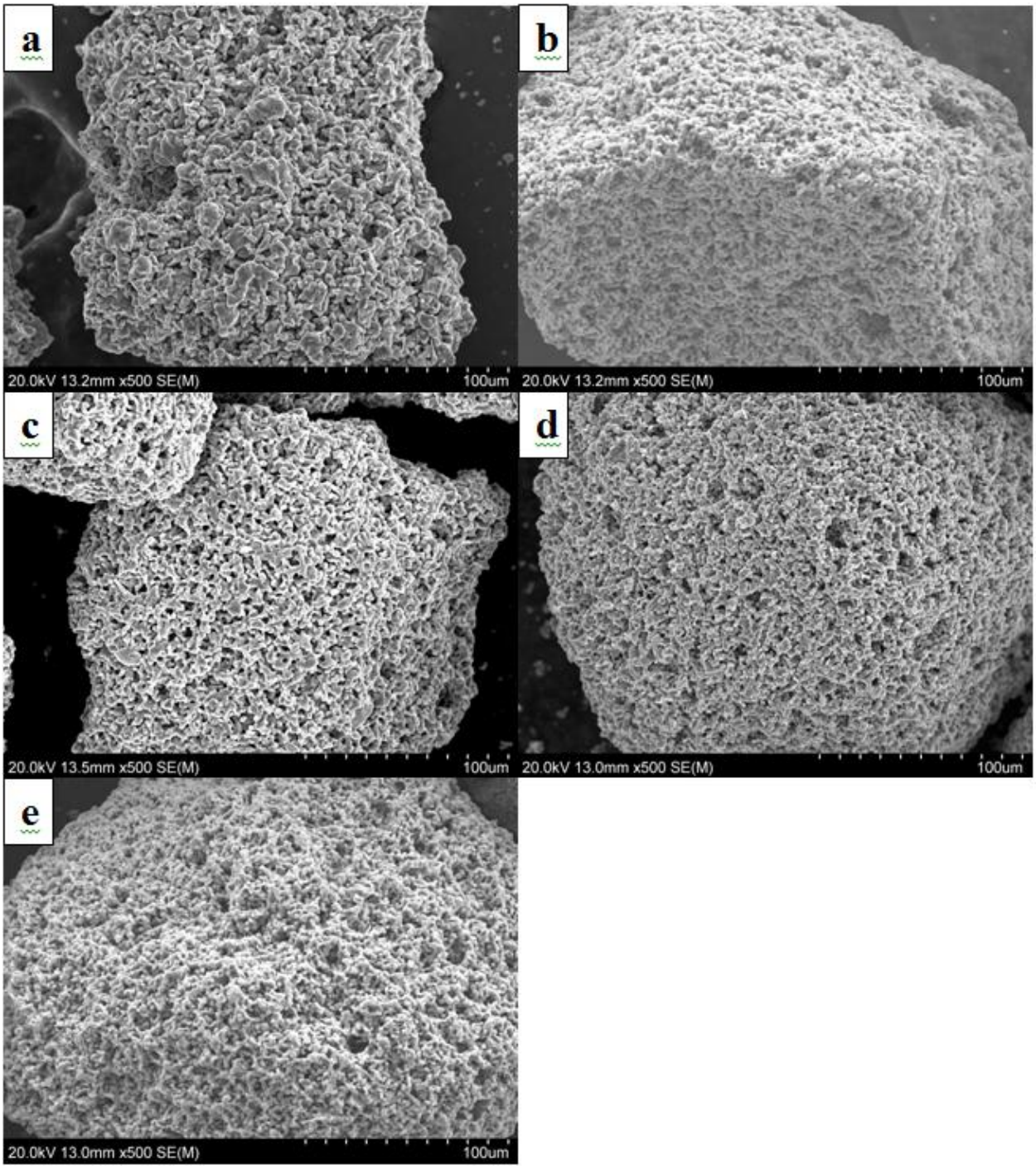

Figure 3-34 SEM images of undoped $CaMnO_{3-\delta}$ soaked for 6 h at 1200 a) and the $(Ca_xLa_{1-x}Mn1-yByO_{3-\delta}$ (Bsite = Fe (b), Ti(c), Al(d), or Zr(e)) soaked for 6 h at 1300°C.

Table 3-10 EDS analysis of the samples (single perovskite) investigated in this work.

element	CM	CLMF	CLMT	CLMA	CLMZ	computational data
Ca	21.64	16.63	18.73	17.60	16.94	18
Mn	19.99	15.74	17.74	16.75	17.03	18
O	58.38	63.84	59.35	61.16	62.20	60
La	-	1.91	2.13	2.05	1.95	2
Fe	-	1.88	-	-	-	2
Ti	-	-	2.05	-	-	2
Al	-	-	-	2.44	-	2
Zr	-	-	-	-	1.87	2

2.4.3 Brunauer– Emmett–Teller (BET) and crushing strength

The Brunauer– Emmett–Teller (BET) specific surface area that was measured by N_2 adsorption is shown in Figure 3-35.

As it can be seen, the BET surface area started to increase while the starch amount was increasing from 0 to 1.2 wt. %. After that, the surface area decreased sharply to 0.19 m^2/g when the starch amount was 12 wt. % in the composition. These results confirmed the SEM results and proved the starch pore forming ability.

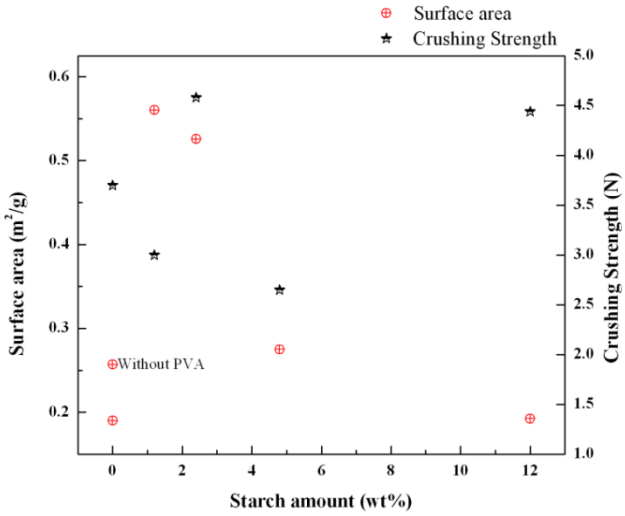

Figure 3-35 BET surface area (m^2/g) and crushing strength (N) of the samples in Table 3-10.

In addition, the crushing strength of the particles were measured and plotted in Figure 3-35. This was to insure that the mechanical properties of the samples did not affect by the porosity so much. All the samples had a crushing strength higher than 1 N. This crushing strength was reasonable enough to give the materials a suitable mechanical strength for CLC application.

2.4.4 Thermogravimetric analysis (TGA)

Figure 3-36 shows the oxygen capacity of the materials tests by a thermogravimetric analyzer when cycled between air (20.8% O_2) and high-purity N_2. As seen, RO varies between 1.02 and 1.48 among the CLMF single perovskites. As shown before, the composition and crystal phase was similar in all of the samples from this group. The only difference was the microstructure of the powders. It seems the porosity of the samples affects the RO capacity as shown in the Figure 3-36-a. Higher porosity gives a material capability to store and release more oxygen compared to samples with lower or near zero porosity. As shown previously, the sample that had 1.2 wt. % starch in its composition had the highest surface area among the others. As a result, it should have the highest RO capacity as well. Comparing the RO capacity of the samples from Figure 3-36-a it can be concluded the samples with suitable amount of starch (1.2 wt. %) and high surface area has the highest RO capacity among the others.

On the other hand, Figure 3-36-b shows the oxygen capacity of the materials for CLOU in samples which were doped on A and B sites simultaneously. As it can be seen, doping the A and B sites reduces the RO capacity of the perovskite. As shown previously, all samples have the same surface area since they were prepared by the optimized extrusion composition. Therefore, the difference in RO capacity comes from the B side elements which were used to dope the perovskite structure.

Doping at the A and B sites both obviously resulted in a decrease in oxygen capacity. Rormark et al.[110] have also reported a lower oxygen transfer capacity for $Ca_{0.9}La_{0.1}MnO_{3-\delta}$ compared to $CaMnO_{3-\delta}$. In our case, the RO capacities of the single perovskite materials decreased from 1.66 (for CM) to 1.22 in the case of CLMT and CLMZ powders.

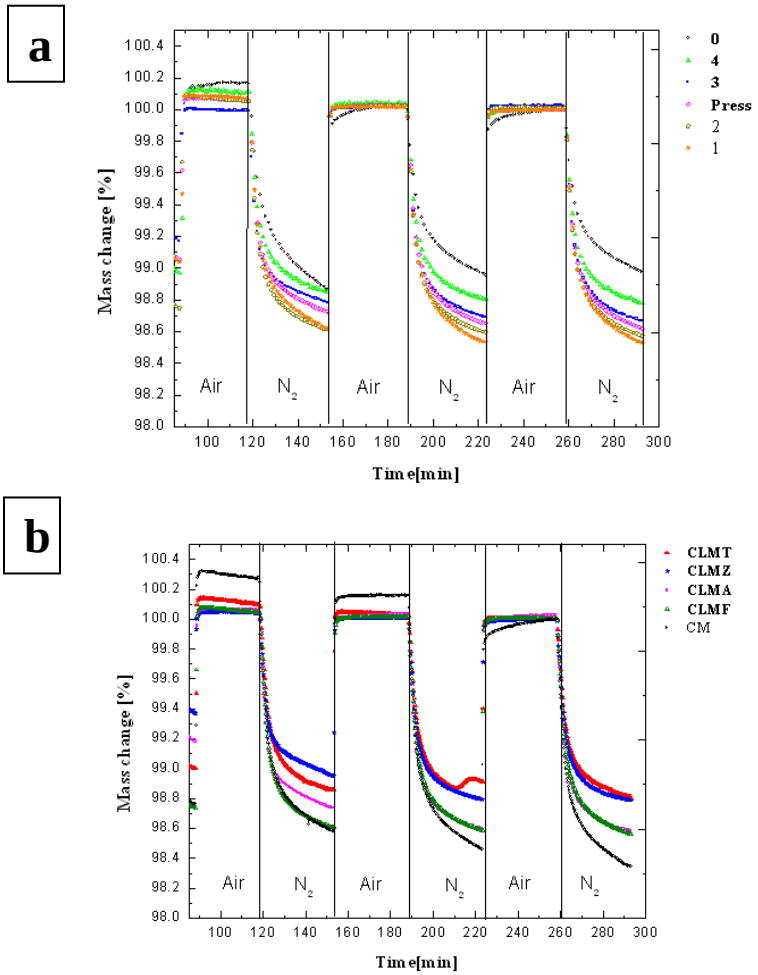

Figure 3-36 (a) Oxygen capacity (RO) of the CLMF composition which was prepared with different extrusion condition (b) Oxygen capacity (RO) of carriers the CM, CLMF, CLMA, CLMT, and CLMZ prepared with optimum extrusion condition during cycling between air (20.8% O_2) and high-purity inert gas (N_2) at 950 °C in a thermogravimetric analyzer.

Arjmand et al. showed that in the case of A- and B-site-doped particles (CLMT, CLMF, and CLMM), the doubly doped compounds are less prone to phase separation, as opposed to their undoped and singly doped analogues. The same behavior was expected here as it can be seen from Figure 3-36-b the RO capacity of the undoped calcium manganese (CM) started to

decrease from 1.7 in cycle one to 1.6 in cycle 3 while in double doped single perovskite the RO value changed only slightly.

2.4.5 Thermogravimetric analysis (TGA)

Figure 3-37 shows the oxygen capacity of the materials tests by a thermogravimetric analyzer when cycled between air (20.8% O_2) and high-purity N_2. In Figure 3-37, RO varies between 1.2 (CLMZ) and 1.75 (CSMF) among the single perovskites which were prepared in this study. Comparing the oxygen capacity of all prepared perovskites in this study in the Figure 3-37 (the experiment was in a cyclic fashion in order to stabilize the data, therefore the last cycle is more reliable), except CSMF, the oxygen capacity has been decreased by doping the A- and B-site of calcium manganese.

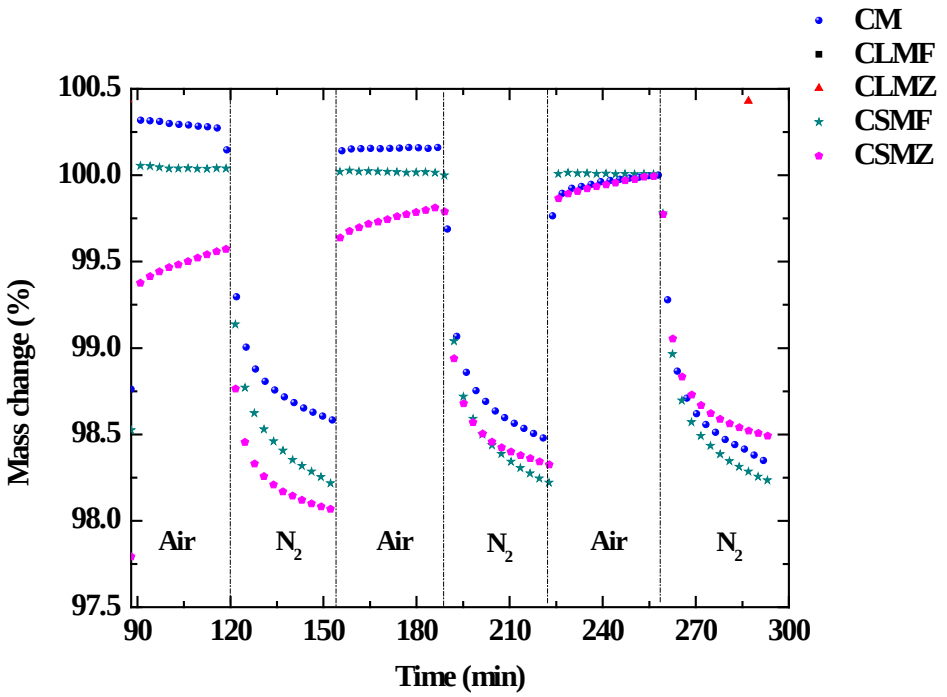

Figure 3-37 Oxygen capacity (RO) of the perovskites which were prepared in this study cycling between air (20.8% O_2) and high-purity inert gas (N_2) at 950 °C in a thermogravimetric analyzer.

2.4.6 Scanning electron microscope analysis (SEM)

The SEM images of prepared perovskites are shown in Figure 3-38. As it can be seen starch acts as a pore-forming agent successfully and all samples have a porous structure.

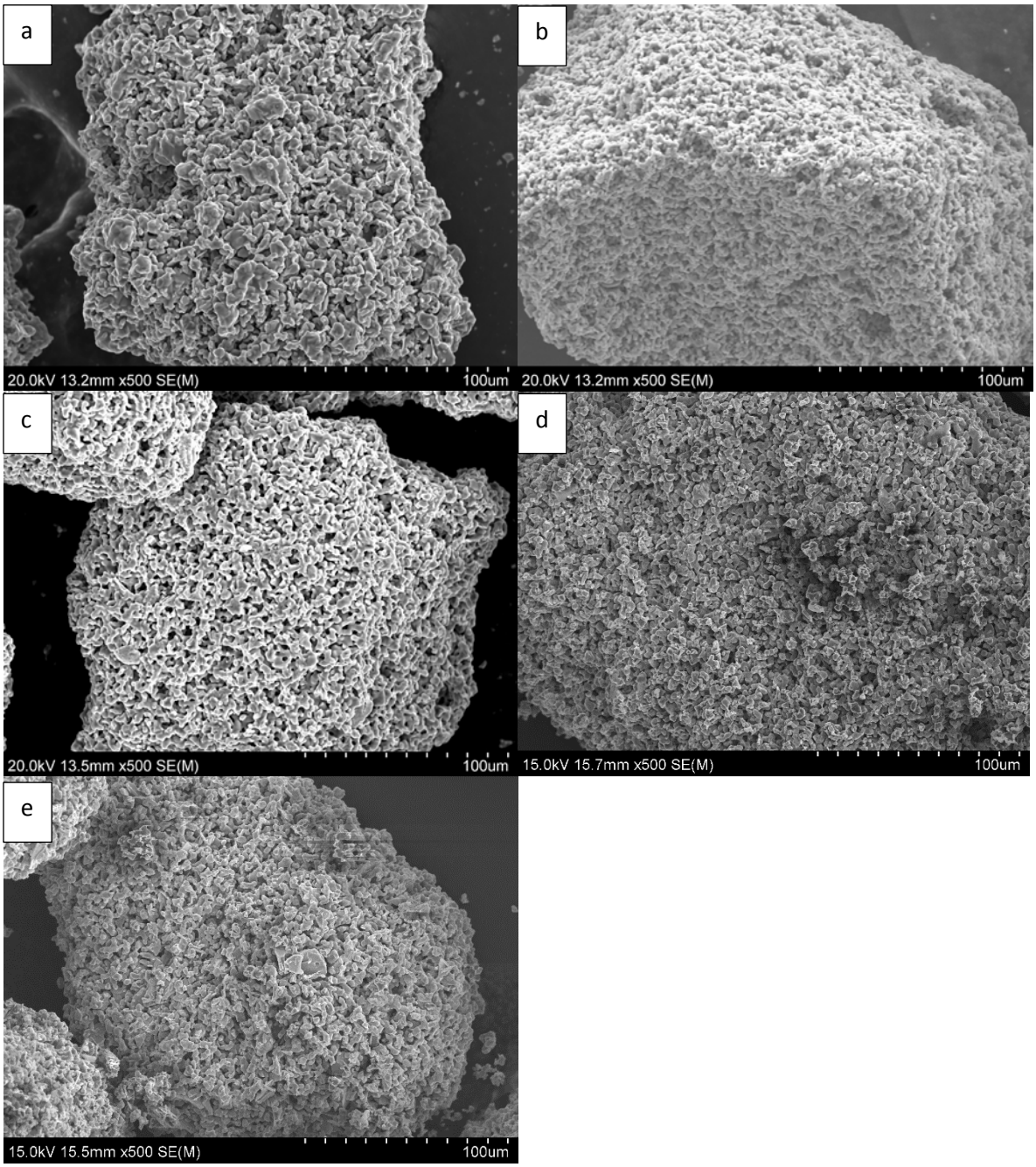

Figure 3-38 SEM images of different perovskites which were studied CM (a), CLMF (b), CLMZ (c), CSMF (d) and CSMZ (e).

EDS (Energy Dispersive Spectroscopy) analyses of the samples were done after calibrating the detector with a pure copper sample. The results are listed at Table 3-11. The results are in agreement with the computational data, indicating that the stoichiometry of the precursors was correct for the production of the perovskite structure. According to the single perovskite formula ($Ca_{0.9}A_{0.1}Mn_{0.9}B_{0.1}O_3$ where A is Sr or La, and B is Fe or Zr), there should be at least 2 at % of the doping element in the samples. As it can be seen from Table 3-11, the atomic percent of these doping elements was near the expected values.

Table 3-11 EDS analysis of the samples (single perovskite) investigated in this work.

element	CM	CLMF	CLMZ	CSMF	CSMZ	computational data
Ca	18.63	16.63	16.94	16.12	17.67	18
Mn	18.75	15.74	17.03	15.30	17.57	18
O	62.62	63.84	62.20	65.10	61.43	60
La	-	1.91	1.95	-	-	2
Fe	-	1.88	-	1.91	-	2
Sr	-	-	-	1.57	1.64	2
Zr	-	-	1.87	-	1.68	2

2.4.7 X-ray diffraction analysis (XRD)

Initial identification phase was made using the PDF-4 Database (Organics database that contains a highly targeted collection, with special focus on materials used in commercial and regulatory fields) and it confirmed the presence of the $CaMnO_{3-\delta}$ perovskite phase (Figure 3-39). In some cases, also additional distorted $CaMnO_{3-\delta}$ phases could be present in the samples but in a very small percentage. Rietveld refinements were carried out using FULLPROF program.

According to XRD database (PDF-4 Release 2013), this phase was distorted calcium manganate ($CaMnO_{3\pm\delta}$) perovskite structure which was doped with lanthanum or strontium at A site and iron or zirconium at B site.

Besides the ionic radii requirements, another condition to be fulfilled is electroneutrality, that is the sum of charges of A and B equals the total charge of oxygen anions. This is achieved by means of suitable charge distribution of the form $A^{1+}B^{5+}O_3$, $A^{2+}B^{4+}O_3$, or $A^{3+}B^{3+}O_3$. In addition to this, partial substitution of A and B ions is allowed, thus yielding an excess of compounds while preserving the perovskite structure. However, deficiencies of cations at the A- or B-sites or of oxygen anions are common, which results in defective perovskites. Oxygen vacancies are more common than those involving cationic vacancies [109].

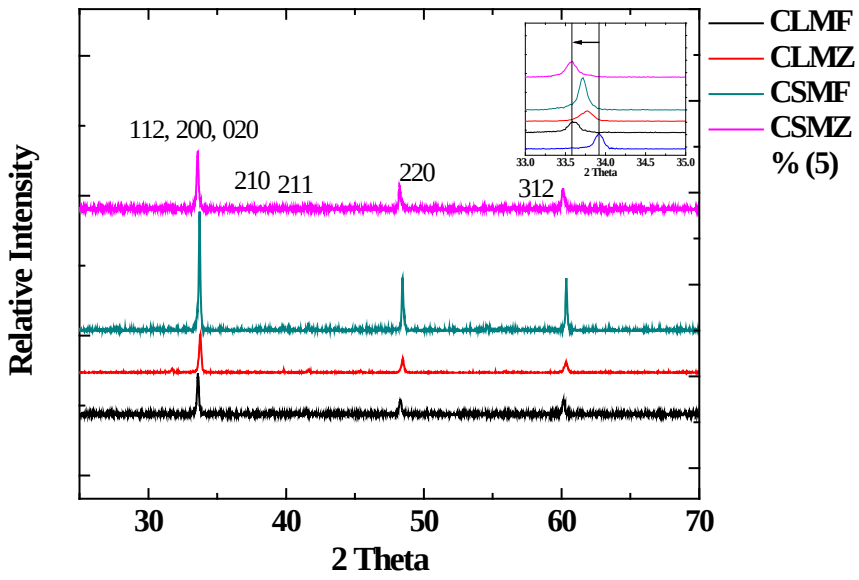

Figure 3-39 XRD patterns of fresh (after synthesis) perovskite family prepared in this study.

In the insets of Figure 3-39 the main peak shifts of the XRD pattern are shown. Replacing ions with different sizes will result in lattice expansion or contraction. The order of ionic size of

ions which were used in this study is as follows: For the B site $Mn^{4+} < Fe^{3+} < Mn^{3+} < Zr^{4+}$ and for the A site $La^{3+} < Ca^{2+} < Sr^{2+}$. As it can be seen, zirconium in the B site and strontium ions in the A site are bigger than the others which may result in higher lattice distortion with respect to the others and lead to Bragg shift to the left as it can be seen in Figure 3-39. In other words, as the ionic radius of all stated ions is larger than that of the Mn^{4+} ion, the increase in the lattice constants is expected. All the lattice constants increased in the same order, showing the expansion of the structure (see Figure 3-39).

2.4.8 Oxygen Uncoupling of the Carriers

Figure 3-40 shows the oxygen release profiles during inert gas purge at four different temperatures for the samples. As it can be seen, all perovskite formulation showed oxygen uncoupling behavior.

A steady decay in the amount of released oxygen as a function of time was seen for the samples heated at 950 °C temperatures and this is quite similar for other three temperatures. This phenomena is typical for the perovskite-type materials and was reported in several papers, where two mechanisms are assumed to be involved: (a) the oxygen non-stoichiometry is an object of defect chemistry, and (b) the release or uptake of oxygen as a function of the oxygen partial pressure in the ambient [124, 125].

The temperature did not show significant effect on oxygen release profile of the samples. It only decreases the rate of oxygen uptake and release in all systems. The CLOU experiments were repeated several times to establish the reproducibility of the observed behavior; there was slight difference from cycle to cycle, specifying that these oxygen carriers were stable and were not deactivated during several cycles.

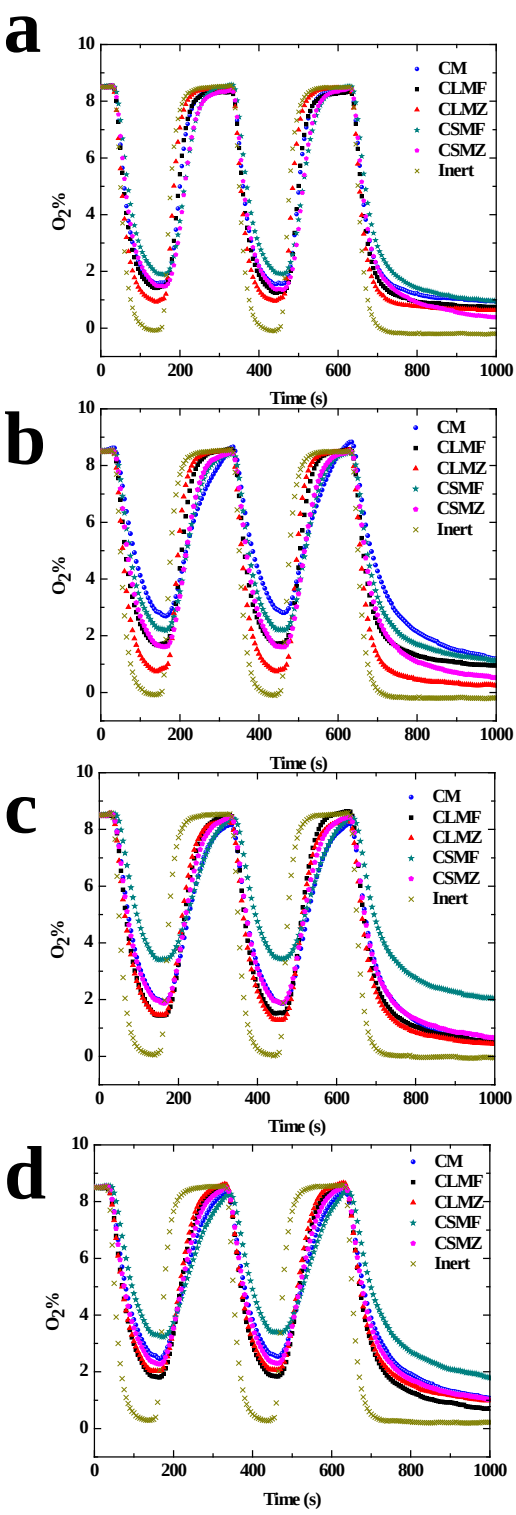

Figure 3-40 Oxygen release profiles for perovskites during cycling between air (20.8% O_2) and high-purity inert gas (N_2) inert gas at 800 (a), 850 (b), 900 (c) and 950 °C (d).

2.4.9 Iodometric titrations

In order to investigate the effect of manganese charge variation in nitrogen and oxygen atmospheres, Iodometric titration was employed on the samples after air and nitrogen treatment at 950 °C for 3 hr. The results are summarized in Table 3-12. The number of oxygen atoms that exists in the compound was calculated based on the amount of Mn^{3+} and Mn^{4+}. The final calculations presented that there could be a mixed valence Mn^{3+} /Mn^{4+} in the system [126]. Iodometric titration analysis revealed that the Mn^{3+} /Mn^{4+} ratio changed in the samples. As it can be seen, in all cases Mn^{3+} formed inside the structure as a result of nitrogen treatment. In other word, manganese ions change their electron valance to lower state while exposed to nitrogen atmosphere. Thus, some part of oxygen ions can release from the lattice to compensate the charge balance. In case of undoped $CaMnO_3$, more than 70 % of Mn^{4+} ions converted to Mn^{3+}, while in doped samples is between 20 to 50 %. This can explain the consistency of the doped samples. As the conversion percent of Mn^{4+} ions to Mn^{3+} is lower in doped samples the structure did not go through extreme contraction or expansion and will remain steady. On the other hand, in undoped samples the structure experiences severe contraction and expansion due to formation of oxygen vacancies and changing the size of manganese ions 53 (Mn^{4+}) to 58(Mn^{3+}) pm. In this way the structure has high potential for segregation [127].

According to the literature, Mn^{4+} ions in $CaMnO_3$ are substituted with Zr^{4+} ions. Similar behavior took place in analyzed samples. More than 60 % of Mn^{4+} reduced to Mn^{3+} in zirconium doped samples. As only 20 % Mn^{4+} remains inside the samples, the oxygen capacity of material will decrease as it can be seen from the TGA analysis.

In iron doped samples the amount of Mn^{4+} did not decrease so much and more than 45 % of Mn ions remain in 4^+ coordination state. As Iodometric titration results shows in iron doped samples,

more than 30 and 50 % conversion for Mn^{4+} to Mn^{3+} is detected. This was expected as the TGA analysis of theses samples, shows higher oxygen capacity for these samples compared to zirconia doped samples.

Surprisingly, in strontium doped sample (CSMF) the amount of Mn^{4+} did not decrease so much and even is 20% higher than the same lanthanum doped sample (CLMF). This is the main reason for high oxygen capacity of strontium doped samples. When some of the Ca^{2+} ions are replaced by, say, La^{3+} ions, it is necessary that a corresponding number of Mn^{4+} ions be replaced by Mn^{3+} ions. So, in all lanthanum doped samples (CLMF and CLMZ) a decrease in oxygen capacity could be expected.

Table 3-12 Determination of Mn^{3+}, Mn^{4+} and oxygen non stoichiometry quantity in doped $CaMnO_3$ by Iodometric titration

Compound	**O**	**δ**	**Mn^{3+}**	**Mn^{4+}**	Oxygen difference
CM	2.91	0.09	0.19	0.81	0.36
CM-N_2	2.55	0.45	0.9	0.1	
CLMF	2.64	0.36	0.47	0.43	0.17
CLMF-N_2	2.47	0.53	0.77	0.13	
CLMZ	2.55	0.45	0.7	0.2	0.09
CLMZ-N_2	2.46	0.54	0.89	0.01	
CSMF	2.83	0.17	0.24	0.66	0.25
CSMF-N2	2.58	0.42	0.74	0.16	

$CaMnO_3$ has octahedral deformation phenomenon, and this indicates that there is some amount of the Mn^{3+} in the structure and some amount of oxygen vacancies as well. Therefore, it is better to observe $CaMnO_3$ as nonstoichiometric phase $CaMnO_{3-\delta}$. The Mn atoms can have two valences, i.e. Mn^{3+} and Mn^{4+}. Different structures of the MnO_6 octahedron is expected, as the ionic sizes of Mn^{3+} and Mn^{4+} are different and the Mn^{3+} ion is the Jahn-Teller active ion (character of Mn^{3+} ,$t_{2g}^3 e_g^1$, with a single eg electron with orbital degeneracy).

Substitution of A- or B- site ions with different ions which have different charge or size provokes reduction of equivalent amount Mn^{4+} into Mn^{3+} [6]. As, the reactivity is, likely, associated with the capacity of manganese to form various oxidation states, e.g., redox reaction of Mn^{2+}/Mn^{3+} or Mn^{3+}/Mn^{4+}, and ‘‘oxygen mobility’’ in the oxide lattice [128] decreasing the manganese valance from four to three will decrease the oxygen capacity of the perovskite structure.

When some of the Ca^{2+} ions are replaced by, say, La^{3+} ions, it is necessary that a corresponding number of Mn^{4+} ions be replaced by Mn^{3+} ions. So, in all lanthanum doped samples (CLMF and CLMZ) a decrease in oxygen capacity could be expected.

On the other hand, in strontium doped sample there is no charge difference between calcium and strontium, as a result the majority of manganese ions remain at higher oxidation state and the oxygen capacity of these groups (CSMF and CSMZ) is higher than the lanthanum doped samples.

The ionic motion in fluorite based systems is the deep-rooted vacancy based mechanism, where one vacancy changing its position with a neighboring oxygen ion in a normal lattice position. The easiest jump is along the edge of the cube formed by eight oxygen ions/vacancies. In the case of perovskites, the most obvious pathway for oxygen ion hopping is through a

triangle formed by two large A-cations and one small B-cation. The circle defined by this triangle was identified as the bottleneck for ionic transport. To optimize the size of the above mentioned bottleneck, simple relations between cation sizes and lattice parameters can be assumed [129, 130].

Having bigger atoms at A- or B-site make the oxygen path bigger, this will lead to higher ion transition rate and oxygen capacity.

2.4.10 Reactivity of the Oxygen Carriers-Part A

The reactivity experiments were done in four different temperatures 800, 850, 900 and 950 °C using methane as fuel and 30 g of particles in the bed. The concentration profile of O_2 and CH_4 plus CO_2 during the combustion period for oxygen carriers investigated in this work are shown in Figure 3-41 and 3-42 respectively. Initially, the carriers are oxidized in 8% O_2. In the next step when the oxidizing stream is switched with pure nitrogen (inert), the oxygen concentration decreases gradually corresponding to the way that it was shown in the Figure 3-41. When methane purged to the reactor, CO_2 is developed as a result of methane conversion; no CH_4 or CO was identified. The oxygen concentration decreases to zero simultaneously. Some uncombusted methane could be detected in the reactor outlet, after complete conversion of methane in the initial part of reduction. Therefore, it is seems that the reduction of perovskite carrier by methane involves of a mixture of two reactions: (1) direct reaction of solid particles with the methane (via CLC) and (2) indirect reaction of methane with the gaseous oxygen released from the carrier (via CLOU) [131, 132].

The oxygen concentration profiles during oxidation (in 8% O_2) at four different temperatures were shown in Figure 3-41. Initially, all of the oxygen in the inlet stream was consumed by the particles that have been reduced severely. This is due to the combustion

process. At the end of the oxidation period, the oxygen concentration rapidly increased until 8 vol %. The temperature of the bed increased only 10-20 °C in the whole oxidation period due to the diluted oxygen concentration used for the experiments. After about 2 min, oxygen increases steadily, approaching the inlet concentration (8%). High degree of reduction seems to be the reason that no oxygen is detected during the initial stages of oxidation. Accordingly, the oxygen partial pressure is relatively low at that time, as the oxygen-depleted carrier taking most of the oxygen in the early part of the oxidation period.

The amount of uncombusted CH_4 is increasing by decreasing the temperature of the bed. All samples that have been tested at temperature lower than 950 °C have more than 10% uncombusted CH_4 in the outlet. The experiments carried out in the fluidized bed reactor allow us to know the behavior of the carriers during successive reduction-oxidation cycles. Moreover, the chemical and structural changes due to the chemical reaction and the attrition phenomena existing in the fluidized beds can be investigated. Table 3-13 shows the bulk density of the fresh and used samples. The bulk density did not change considerably; small changes could be due to measurement uncertainties. All samples have crushing strength more than 1 N, which is suggested for the CLC application. There is no huge weight loss among the samples which can indicates they have enough strength for withstanding erosion and high temperature reactions during the tests.

Comparing the BET surface area of the sample with inert sample which is Quartz frits without any pore indicates that the starch plays an important role in increasing the surface area of the samples. An increase between 5 to 10 times in surface area support this phenomenon.

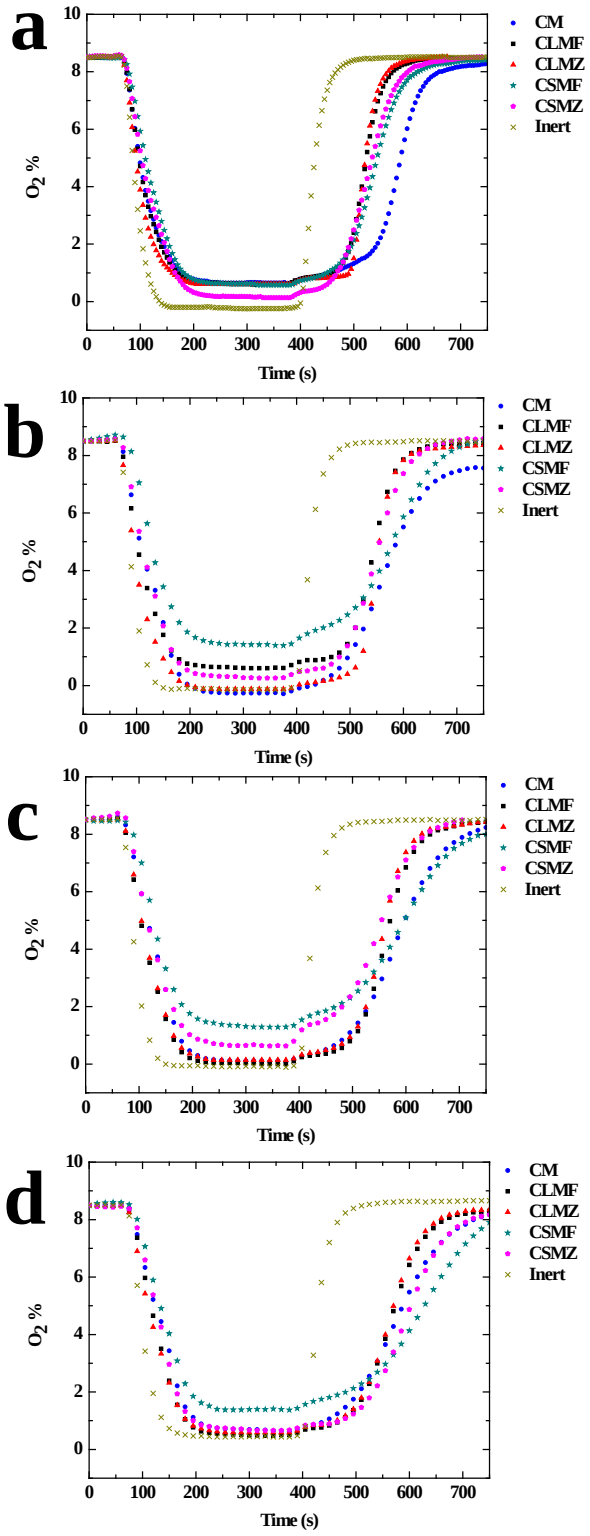

Figure 3-41 Concentration of O_2 during conversion of CH_4 at 800-a, 850-b, 900-c and 950 °C-d for 20 s using 30 g of samples.

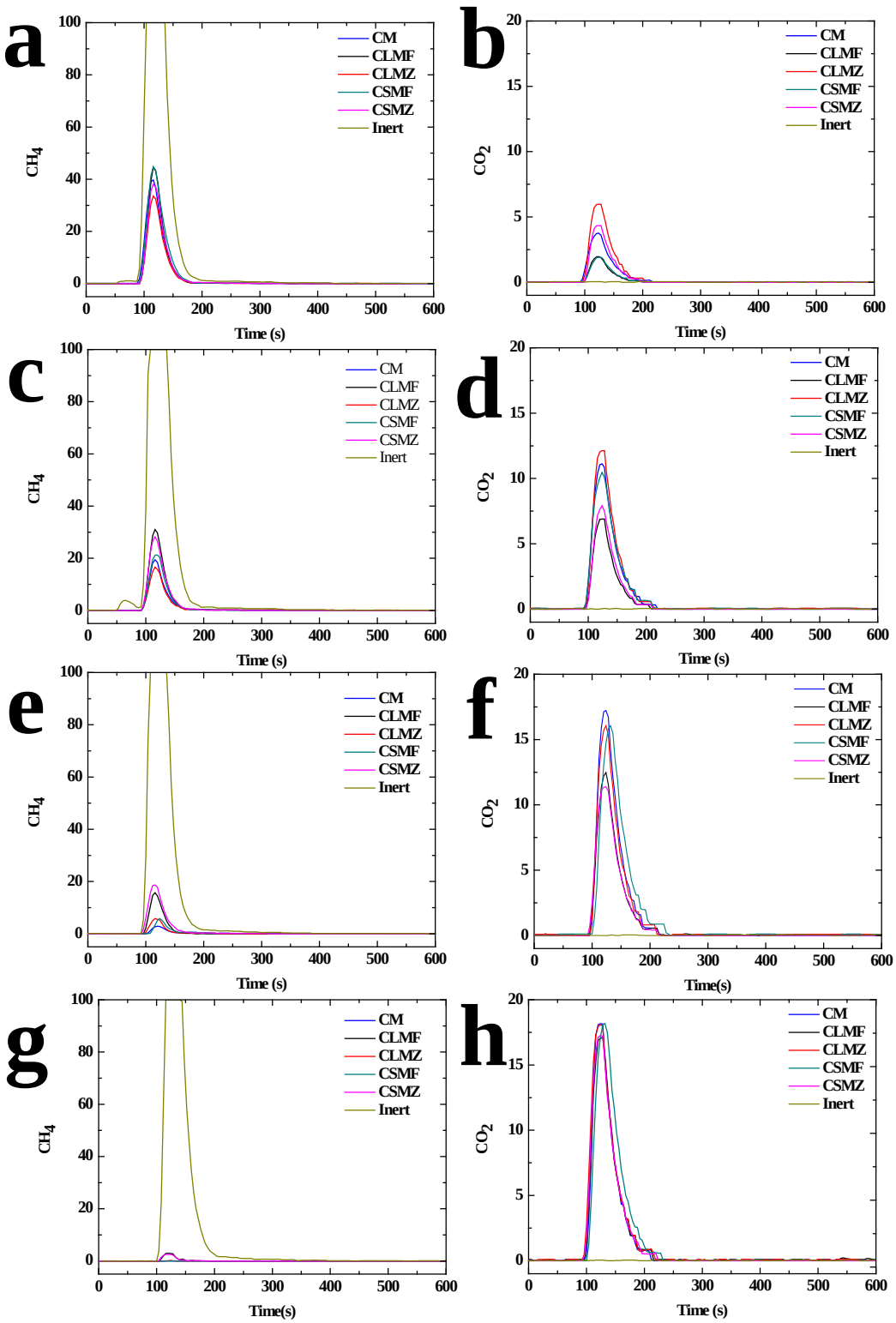

Figure 3-42 Concentration of various gaseous species CO_2 and CH_4 during conversion of CH_4 at 800-a and b, 850-c and d, 900-e and f and 950 °C –g and h for 20 s using 30 g of sample followed by oxidation in 8% O_2.

Table 3-13 Bulk density (g/cm^3), sample weight before and after the reactor test, BET and crushing strength of the Oxygen Carriers before and after the Reactivity Test (±0.001 error)

Sample ID	Bulk density (gr/cm^3) before reactor test	Bulk density (gr/cm^3) after reactor test	Sample weight (gr) before reactor test	Sample weight (gr) after reactor test	BET(m^2/gr) before test	Crushing Strength N
CM	4.49	4.56	30	29.47	0.95	2.19±0.7
CLMF	4.68	4.71	30.019	29.45	0.56	3.12±0.9
CLMZ	4.76	4.83	30.005	29.47	0.82	1.67±0.4
CSMF	4.66	4.59	30.027	29.66	0.42	2.3±0.7
CSMZ	4.69	4.61	30	28.57	0.74	1.5±0.5
Inert	2.22	2.21	30	29.99	0.09	-

2.4.11 Reactivity of the Oxygen Carriers (CLC)-Part B

The reactivity experiments are conducted at four different temperatures: 800, 850, 900 and 950 °C, using methane as the fuel and 30 grams of the prepared particles in the reactor bed. For a more thorough understanding of the obtained CLC results, a new variable, mass-based conversion of the oxygen carrier (ω), should be introduced. ω is calculated via the following formula (Eq.6) in which m is the actual mass of the prepared carriers.

$$\omega = \frac{m}{m_{ox}} \tag{6}$$

During the CLC process, the mass-based conversion of the oxygen carriers throughout the reduction reaction can be calculated using the following equation (Eq.7) in which y_i represents the concentration (vol %) of the respective gas:

$$\omega_i = \omega_{i-1} - \int_{t_0}^{t_1} \frac{\dot{n}_{out} M_O}{m_{ox}} \left(4y_{CO_2} + 3y_{CO} + 2y_{O_2} - y_{H_2}\right) \tag{7}$$

ω_i = Instantaneous mass-based conversion at time i

ω_{i-1} =Mass-based conversion in the preceding instant

t_0 = Initial time of measurement

t_1 = Final time of measurement

$\dot{n}_{out}$ = Molar flow rate of the dry gas at the reactor outlet

M_O = Molar mass of oxygen

Figure 3-43 shows the variation of mass-based conversion, ω, with time for reduction with methane at four different temperatures. The ω profiles are a combination of the direct reaction of methane with the solid carrier either via CLC or gaseous oxygen via CLOU. As it can be seen, ω starts to decrease faster by increasing the temperature.

Gas yield is another defining parameter in evaluating the performance of the oxygen carriers in CLC processes. This parameter is usually evaluated in fluidized bed reactors and can be measured using the following equation (Eg.8):

$$\gamma_{CH_4} = \frac{y_{CO_2}}{y_{CO_2}+y_{CH_4}+y_{CO}} \quad (8)$$

Figure 3-44 shows the gas yield, γ_{CH4}, over the mass-based conversion, ω, for methane exposure period for all of the investigated carriers. As it can be seen from Figure 3-44, CM, CSMF and CLMZ show gas yield of 100%, while the other two compositions show lower gas yields but still high enough (more than 85%) during the entire reduction period. Comparing the results with other similar works [125], indicates that the fabricated oxygen carriers in this study can be promising candidates for CLC applications since they have shown the highest gas yields and have resulted in complete combustion of methane over the entire reduction period.

Doping the A and B sites seems to be an important controlling factor in governing the combustion mechanism of perovskite oxides in CLC and CLOU reactions. It has two major roles in determining the oxygen capacity of the perovskites. First, it can change the $Mn^{4+}/Mn^{3+}/Mn^{2+}$ ratio in the system and change the oxygen capacity of the carriers consequently. Moreover, as

discussed earlier, the oxygen migration path through the perovskite crystal is controlled by the size of A- and B- atoms. B- atoms specifically play a more crucial role in this case as the critical radius of bottleneck, r_c, is defined by two B- and one A- atom.

Thermodynamic and kinetic parameters also affect the CLC and CLOU reactions. The thermodynamic factor is defined by partial pressure of oxygen, which is set by the temperature of the reaction, whereas the kinetic factor is controlled by diffusion parameters (temperature and time) and crystallographic limitations of the oxygen carriers. One important feature of CLC which distinguishes it from CLOU is the necessity of combustion reaction or oxygen concentration gradient on the surface of oxygen carriers in CLC process. In other words, if there is no combustion or fuel on the surface of the particles, CLC does not occur. However, the CLOU process can continue its progress until the reaction reaches the equilibrium partial pressure of oxygen on the surface of the oxygen carriers. Both mechanisms are controlled by diffusion of oxygen atoms. Therefore, temperature and time play an important role in them. In the case of CLOU, the partial pressure of oxygen on the surface which is set by the temperature is also involved in the reaction. If the partial pressure of oxygen in a specific temperature is low, the CLOU process will stop due to thermodynamic limitations. Whereas, CLC can occur if sufficient fuel exists on the surface.

The oxygen capacities of the materials evaluated by the thermogravimetric analyzer and oxygen release profiles during inert gas purge are good indications of CLOU process taking place at different temperatures and with different samples, whereas the mass-based conversion shows the contribution of both.

As it is observed in Figure 3-43, all of the prepared samples have similar oxygen release profiles at 800 ^{o}C, whereas increasing the temperature has noticeable increase on the oxygen release profile of CSMF at different temperatures. However, other samples do not show evident changes in oxygen release profiles by increasing the temperature. These results are also confirmed by thermogravimetric analyzer evaluating the oxygen capacity of the materials. Among the prepared samples, CSMF has shown the highest RO capacity among the others at 950 ^{o}C. The main reason for this occurrence is the existence of kinetic barriers in different doping systems. The reaction temperature is fixed for all of the samples and based on thermodynamic properties all samples are expected to release the same amount of oxygen or at least show the same trends for same temperatures based on their $Mn^{4+}/Mn^{3+}/Mn^{2+}$ ratios. Since CSMF shows a completely different trend of oxygen release by increasing temperature, it seem this sample has a better crystallographic structure with respect to the others. Looking in more depth in the structural properties can reveal the reason behind this unexpected trend. This sample has strontium partially substituted at its A- site and as a result have been more distorted and spaced than Lanthanum doped or undoped samples. This can facilitate the oxidation and reduction reaction for the perovskite system undergoing extreme contractions and expansions. First, Mn ions have more freedom to change their valance as the radius of Mn changes almost 22% when it changes its valance from 4+ to 3+. Second, there will be more space for oxygen diffusion in the structure as discussed earlier. All these parameters can support the reason for high oxygen uncoupling behavior (CLOU) of CSMF.

The fluidized bed temperature increases during the oxidation period is in the range of 10-20 °C and this low increase in temperature is due to the diluted oxygen stream (low oxygen concentration) used for conducting the experiments. The amount of uncombusted CH_4 is

increased by decreasing the temperature of the bed. All tested samples at temperatures lower than 950 °C have shown more than 10% uncombusted CH_4 in the reactor outlet stream.

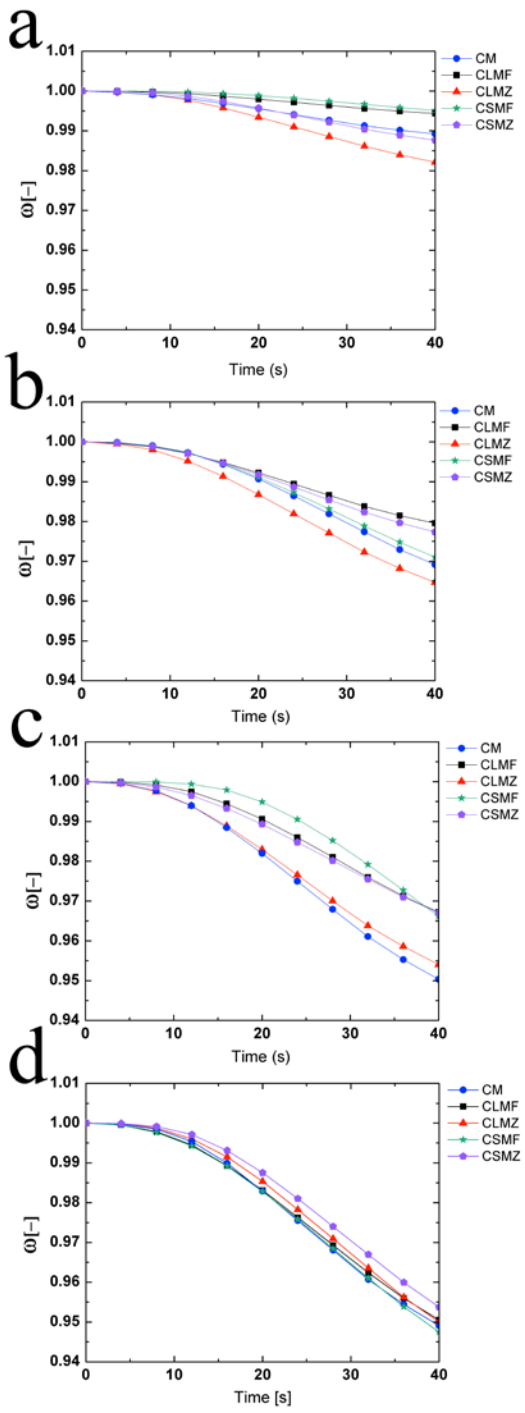

Figure 3-43 Variation of the mass-based conversion, ω, of the oxygen carriers with time for reduction with methane (for 20 s) at 800 (a), 850 (b), 900 (c) and 950 °C (d).

The experiments carried out in the fluidized bed reactor allow us to understand the behavior of the carriers during reduction-oxidation cycles. Moreover, the chemical and structural changes can be investigated due to the existence of chemical reaction and the attrition phenomena in the fluidized beds. The data represented in Table 3-13 demonstrates the bulk density of the fresh and used samples. The bulk density as observed does not change considerably and the slight changes could be due to measurement uncertainties.

All of the samples have a crushing strength more than 1 N, which is suggested to be the suitable quantity for an oxygen career used in CLC applications.

No huge weight loss is detected for the samples, which indicates their appropriate strength for withstanding erosion and high temperature reactions during the tests.

By comparing the surface areas of the prepared samples with the inert sample (Quartz frits, with no surface porosity) using BET analysis, it can be concluded that the starch plays an important role in increasing the surface area (between 5 to 10 times) of the samples. This claim is also supported by comparing the surface area obtained for CLMF and CM perovskites in the literature and current work. The surface areas observed for CLMF and CM samples, are near 0.6 and 1 (m^2/g) respectively, which are three times higher than the reported quantities in the literature using the same preparation method (solid state reaction) and this is due to the optimization process [125, 133].

Although the surface area of the samples, synthesized by the solid state reaction, is much lower than the samples fabricated by reactive grinding or other expensive techniques (in the range of 25-50 m^2/g) [45, 134] there should always be a balance between the preparation cost and physical properties of the materials under investigation. Mostly in commercial applications,

cost and simplicity are two major factors that play important roles for choosing the right preparation techniques.

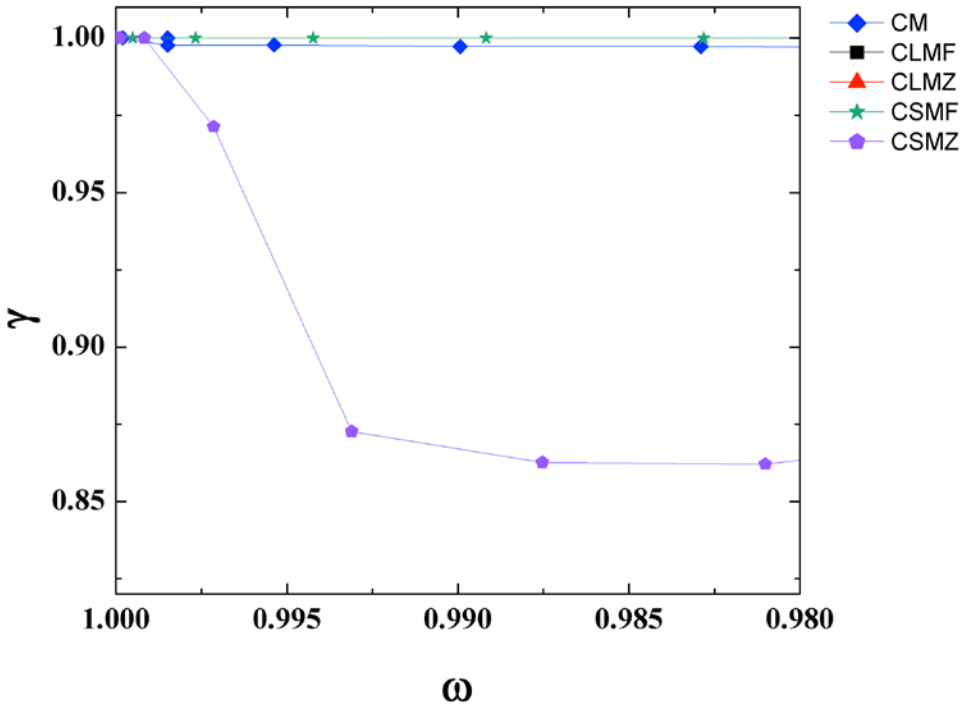

Figure 3-44 Variation of gas yield, γ CH_4, with mass-based conversion, ω, for different oxygen carriers during conversion of CH_4 for 20 s at 950 °C.

2.5 Characterization: physicochemical, surface area, porosity, structural and microstructural evaluation

2.5.1 TGA and Iodometric titration

If simply assumed that all the Mn^{4+} inside the sample will be converted to Mn^{2+} during the heating in the inert gas the loss should be 20 mol% according to Eq.9 One mole of oxygen out of five mole atoms in $CaMnO_3$ will released which is 20 mol % and equal to approximately 11.2 wt. %.

$$CaMnO_3 \rightarrow CaMnO_2 + 1/2O_2 \quad (9)$$

Figure 3-45 shows the oxygen capacity of the materials tested by a thermogravimetric analyzer, when cycled between air (20.8% O_2) and high-purity N_2. As seen, the loss percent is about 3 % after 250 minutes, which is considerable lower than the expected value.

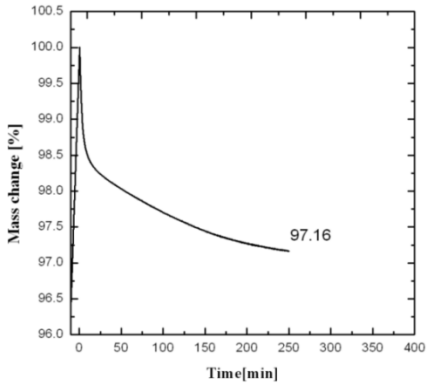

Figure 3-45 Oxygen capacity (RO) of the $CaMnO_3$ carriers during cycling between air (20.8% O_2) and high-purity inert gas (N_2) at 950 °C in a thermogravimetric analyzer.

2.5.2 Iodometric titration

Iodometric titration for identification of average oxidation state of manganese in mixed oxides was employed. The number of oxygen atoms that exists in the compound was calculated based on the amount of Mn^{3+} and Mn^{4+}. The final calculations presented the actual $CaMnO_3$ formula, which is $CaMn_{0.19}{}^{3+}Mn_{0.81}{}^{4+}O_{2.9}$. So it appears that there could be a mixed valence Mn^{3+} /Mn^{4+} in the system [126]. As mentioned previously, to investigate the effect of heat treatment in N_2 atmospheric samples were heat treated at 950 °C for 3 hours in N_2 atmosphere. The samples were cooled down to room temperature while they were exposed to N_2. Iodometric titration analysis revealed that the Mn^{3+} /Mn^{4+} ratio changed in the samples. The new ratios are 90% Mn^{3+} and 10% Mn^{4+}. Therefore, it seems the majority of the Mn^{4+} is converted to Mn^{3+}.

Recently, doped $CaMnO_3$ received special attention due to several properties which are improved via doping. First, doubly doped compounds are less likely to phase separation, as opposed to their undoped and singly doped correspondents [125].

Second, as mentioned before, one way of preventing ordering in perovskite structure is doping the A- or B- site with different valance states. This will improve the oxygen carrying capacity of the materials and finally, increasing the reactivity and performance of the perovskite in specific application.

Figure 3-46 shows the oxygen capacity of the materials for CLOU in samples which were doped on A and B sites simultaneously. As it can be seen, doping the A and B sites reduces the RO capacity of the perovskite. All samples have the same surface area since they were prepared by the optimized extrusion composition. Therefore, the difference in RO capacity comes from the B side elements which were used to dope the perovskite structure.

Doping at the A and B sites both obviously resulted in a decrease in oxygen capacity. Rormark et al.[110] have also reported a lower oxygen transfer capacity for $Ca_{0.9}La_{0.1}MnO_{3-\delta}$ compared to $CaMnO_{3-\delta}$. In our case, the RO capacities of the single perovskite materials decreased from 1.66 (for CM) to 1.22 in the case of CLMT and CLMZ powders.

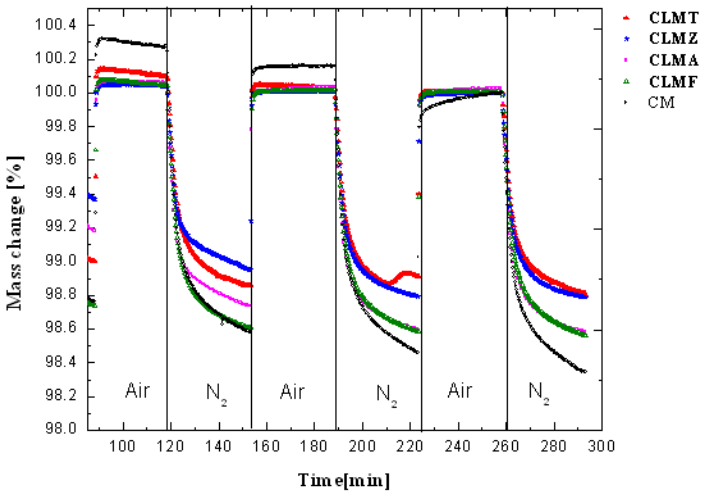

Figure 3-46 Oxygen capacity (RO) of carriers the CM, CLMF, CLMA, CLMT, and CLMZ prepared with optimum extrusion condition during cycling between air (20.8% O_2) and high-purity inert gas (N_2) at 950 °C in a thermogravimetric analyzer.

Arjmand et al. showed that in the case of A- and B-site-doped particles (CLMT, CLMF, and CLMM), the doubly doped compounds are less prone to phase separation, as opposed to their undoped and singly doped analogues.

As stated above, Mn^{3+} and Mn^{4+} exist simultaneously, and that their ratio can be adjusted chemically by doping at the A and B sites. The doped electrons or holes appear to remain essentially localized on Mn sites leading to isolated Mn^{3+} or Mn^{4+} ions which coexist inside the structure [11, 12].

Iodometric titration was employed on doped samples after air and nitrogen treatment at 950 °C for 3 hr. The results are summarized in Table 3-14.

Table 3-14 Determination of Mn^{3+}, Mn^{4+} and oxygen non stoichiometry quantity in doped $CaMnO_3$ by Iodometric titration

Compound	**O**	**δ**	**Mn^{3+}**	**Mn^{4+}**	
CM	2.91	0.09	0.19	0.81	0.36
CM-N_2	2.55	0.45	0.9	0.1	
CLMA	2.91	0.09	0.19	0.71	0.21
CLMA-N_2	2.7	0.3	0. 59	0.31	
CLMF	2.88	0.12	0.25	0.65	0.25
CLMF-N_2	2.63	0.37	0.63	0.27	
CLMT	2.88	0.12	0.34	0.56	0.03
CLMT-N_2	2.85	0.15	0.39	0.51	
CLMZ	2.77	0.23	0.56	0.34	0.10
CLMZ-N_2	2.67	0.33	0.77	0.13	

As it can be seen, in all cases Mn^{3+} formed inside the structure as a result of nitrogen treatment. In other words, manganese ions change their electron valance to lower state while they exposed to nitrogen atmosphere. Thus, some part of oxygen ions can release from the lattice to compensate the charge balance. In the case of undoped $CaMnO_3$, more than 70 % of Mn^{4+} ions converted to Mn^{3+}, while in doped samples it is between 20 to 35 %. This can explain the consistency of the doped samples. As the conversion percent of Mn^{4+} ions to Mn^{3+} is lower in doped samples the structure did not experience extreme contraction or expansion and will remain steady. On the other hand, in undoped samples the structure receive severe contraction and expansion due to formation of oxygen vacancies and changing the size of manganese ions 53 (Mn^{4+}) to 58(Mn^{3+}) pm. In this way the structure has high potential for segregation.

Ionic radius of Ti^{4+} ion is known to be in between the ionic radii of Mn^{4+} and Mn^{3+}. Therefore, there is a distinct possibility that a fraction of Ti^{4+} ions can occupy Mn^{3+} sites in addition to the Mn^{4+} sites. The available literature on Ti substitution in manganites indicates that Ti^{4+} ions occupy the isovalent Mn sites in these materials. Recent reports have shown that though it prefers to occupy Mn^{4+} sites, at high doping levels it also occupies Mn^{3+} sites. [127].

As it can be seen, from the Iodometric titration result in Ti doped samples the amount of Mn^{4+} inside the samples is decreased. It seems the Ti^{4+} prefers to occupy the Mn^{4+}/Mn^{3+} inside the samples and reduce some part of Mn^{4+} ions to Mn^{3+}. Ti^{4+} prefers to occupy the octahedral position in a crystal lattice according to its size and charge. Therefore, the amount of Mn^{4+} and Mn^{3+} in heat treated samples in N_2 did not show significant change. In this case, it seems the structure pinned to its position and the majority of Mn^{4+} ions remain unchanged. As a result, the oxygen capacity of material will decrease, as it can be seen from the TGA analysis. According to the literature Mn^{4+} ions in $CaMnO_3$ are substituted with Zr^{4+} ions. Similar behavior took place in

analyzed samples. More than 60 % of Mn^{4+} reduced to Mn^{3+} in zirconium doped samples. As only 20 % Mn^{4+} remains inside the samples, the oxygen capacity of material will decrease as it can be seen from the TGA analysis.

In iron and aluminum doped samples the amount of Mn^{4+} did not decrease so much and more than 45 % of Mn ions remain in 4+ coordination state. As Iodometric titration results show, in aluminum and iron doped samples, more than 30 % conversion for Mn^{4+} to Mn^{3+} is detected. This was expected as the TGA analysis of theses samples, shows higher oxygen capacity for these samples compare to zirconia and titanium doped samples.

2.5.3 XPS spectroscopy

The XPS spectra in the region of the Mn 2p level are shown in Figure 3-47. A usual $2p_{1/2}$ and $2p_{3/2}$ spin-orbit doublet can be seen in all the spectra. The Mn (2p) peaks, in agreement with previous studies, are broad and asymmetrical towards high binding energy side [135, 136].

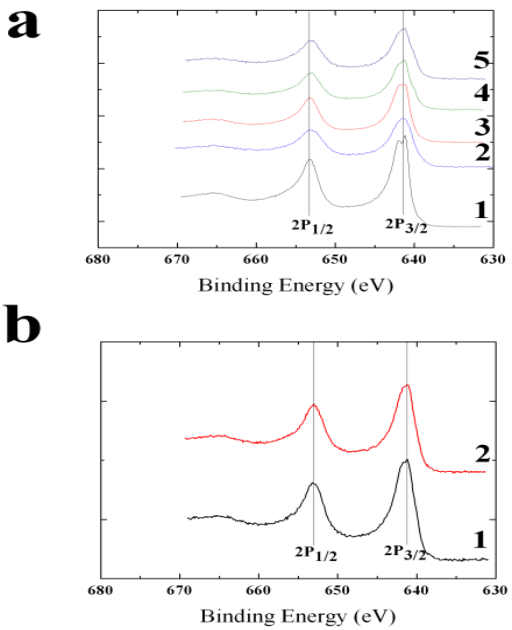

Figure 3-47 Mn(2p) electron spectra of (a) heat treated at air: 1-CM 2-CLMF 3-CLMA 4-CLMT 5-CLMZ, (b) heat treated at N_2: 1-CM, 2-CLMF

As it can be seen the $2p_{1/2}$ peak appears at the same energy ~653.1 eV in all the compounds. However, the $2p_{3/2}$ peak does show a chemical shift of 0.5-0.8 eV to higher binding energies. A small hump appears around 642 eV which is believed to be related to Mn^{4+} valence state.

Table 3-15 Binding energies (eV) of Mn 2p and Ca 2p electrons in calcium manganites.

Sample	**Mn**		**Ca**	
	$2p_{3/2}$	**$2p_{1/2}$**	**$2p_{3/2}$**	**$2p_{1/2}$**
CM	641.2 642	653.1	344.8	348.4
CM-N_2	641.2	653	345	348.6
CLMF	641.2 642.7	653.1	345.1	348.7
CLMF-N_2	641.2	653.1	345.2	348.7
CLMA	641.2 641.9	653.3	344.9	348.4
CLMT	641.2 641.8	653.3	345	348.5
CLMZ	641.2 641.7	653.2	345	348.5

As the higher binding energy of Mn $2p_{3/2}$ electrons in air sintered $CaMnO_3$ suggests Mn to be in +4 valence state, occupying sites with octahedral coordination. As confirmed previously with iodometric titration tests, all samples contains Mn^{3+} and Mn^{4+} ions. Therefore, having two peaks in the $2p_{3/2}$ energy level is expected. As the Mn^{4+} concentration is high in CM sample according to iodometric titration results, the peak around 642 ev is sharper than the others. The N_2 treatment of $CaMnO_3$ involves introduction of O vacancies and conversion of Mn^{4+} ions into lower oxidation states. The lower binding energy in $CaMnO_{3-\delta}$ is indicative of this process.

As it can be seen the hump is disappeared after heat treating the CM and CLMF samples in N_2 atmosphere (see Figure 3-47-b). Again, these are in good agreement with iodometric titration results and indicated that in CM and CLMF samples the majority of Mn ions oxidation states convert to lower sate 3+ after heat treating in N_2 atmosphere. However, The binding energies of Ca(2p) electrons assumed to be a constant reference level, and as it can be seen from Table 3-15 this energy in the specimens is nearly identical. Due to different crystal structures of the specimens, a slight variation in their values is acceptable (Table 3-15).

2.5.4 FTIR spectroscopy

Infrared (IR) phonon spectra are sensitive to local lattice distortions [137]. At 300 K, the spectrum shows three main phonon bands. There are six vibration modes in the MnO_6 octahedron with an ideal perovskite-type structure. Among these modes, there are three kinds of modes corresponding to the stretching vibration and other three corresponding to the bending vibration. The mode, located around 170 cm^{-1}, represents a vibrating motion of the La (Ca) ions against the MnO_6 octahedral. The bending mode, located around 330 cm^{-1} , reflects an internal motion of the Mn and O ions located along a particular direction against the other oxygen ions in a plane perpendicular to the direction. This mode is strongly affected by a change in the Mn-

O-Mn bond angle. The stretching mode, located near 580 cm^{-1} , corresponds to an internal motion of the Mn ion against the oxygen octahedron and is sensitive to the Mn-O bond length [138, 139].

The infrared absorption spectra from 450 to 750 cm^{-1} for the samples measured at room temperature, are shown in Figure 3-48. The main absorption band around 563–602 cm^{-1}corresponds to stretching of the metal–oxygen bond in the perovskite, which involves the internal motion of a change in Mn–O–Mn bond length in MnO_6 octahedral. Generally, there are two major factors that obviously affect the infrared vibration frequency of the multiplex perovskite oxide compound: one is the geometry factor and another is the electric factor. Substitution of A- or B- site ions with a small ionic radius in the $CaMnO_3$ system decreases the volume of crystal unit cells and shortens the average distance between atoms and then increases the electron–phonon interaction and hence the Mn−O bond stretching vibration frequency decreases as the infrared absorption intensity increases. It is obvious when the substitute ion is larger the Mn−O bond stretching vibration frequency will increase. The above results are caused by the geometrical and electronic factors together. An absorption peak observed at 710 cm^{-1} is related to the coupling between crystal lattice and charge [140].

Replacing Mn with a smaller or bigger transition or pure metals increases the magnitude of the octahedral tilting, which in turn causes a decrease or increase in Mn-O-Mn bond angle [141].

Un-doped $CaMnO_3$ has a well resolved band at 569 cm^{-1}. This band corresponds to O-Mn-O vibration modes. As it can be seen from the Figure 3-48, doping the B- site has an effect on this vibration's mode. According to this figure, the peaks around 569 cm^{-1} subjected to change, while the $CaMnO_{3-\delta}$ doped with Fe, Al, Ti and Zr ions, demonstrated a successful doping

process. This shift is more obvious in iron-doped samples, which may have resulted from more oxygen vacancies in this sample (Table 3-15).

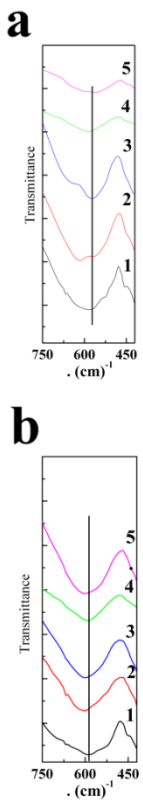

Figure 3-48 Infrared spectra of the products obtained from heat treated sample in air (a) and in N_2 (b) at 950 °C for 3 hr. 1-CM, 2-CLMF, 3-CLMA, 4-CLMT and 5-CLMZ

The effect of heat treating the samples in N_2 at 950 °C can be distinguee from Table 3-16. In all cases the band shifts to higher wavelength. This increase is more obvious in Fe, Al and Zr doped samples while it is less severe in undoped and Ti doped samples. The interaction of electron–phonon decreases due to the oxygen removal from the lattice. This will decrease the packing factor ratio of the lattice and hence the Mn−O bond stretching vibration frequency increases. In undoped sample although more oxygen left the lattice compare to other products, the stretching vibration frequency did not increase so much. This can be explained by the crystal

structure. In undoped sample the lattice loses so much oxygen and there are significant amounts of non-bridging oxygen inside the structure (Figure 3-50-c) as a result the lattice is not as rigid as before and less energy needed for electron–phonon interaction.

Table 3-16 The O-Mn-O vibration modes in doped and undoped calcium manganites heat treated in air and in N_2 at 950 ^oC for 3 hr.

Sample	$(cm)^{-1}$	
	Air	N_2
CM	586.35	590.21
CLMF	563.21	601.78
CLMA	574.78	601.78
CLMT	586.35	590.21
CLMZ	578.64	601.78

2.5.5 XRD analysis

Figure 3-49 shows the XRD data of the $CaMnO_{3-\delta}$ heat treated in air and pure N_2. As it can be seen, the crystal structure changed and the peaks are doubled. These splitting of the reflections present in the XRD-pattern of cubic perovskite are directly related to the type of octahedral tilting. It seems as a result of heat treating the samples inside the N_2 for a long time a high amount of oxygen vacancies are formed inside the samples and start to order inside the

structure. The structure will try to tilt in order to compensate the oxygen vacancies inside the lattice.

In other words, while oxygen leaves the lattice, the structure tries to fill its position by tilting and moving other ions closer to each other.

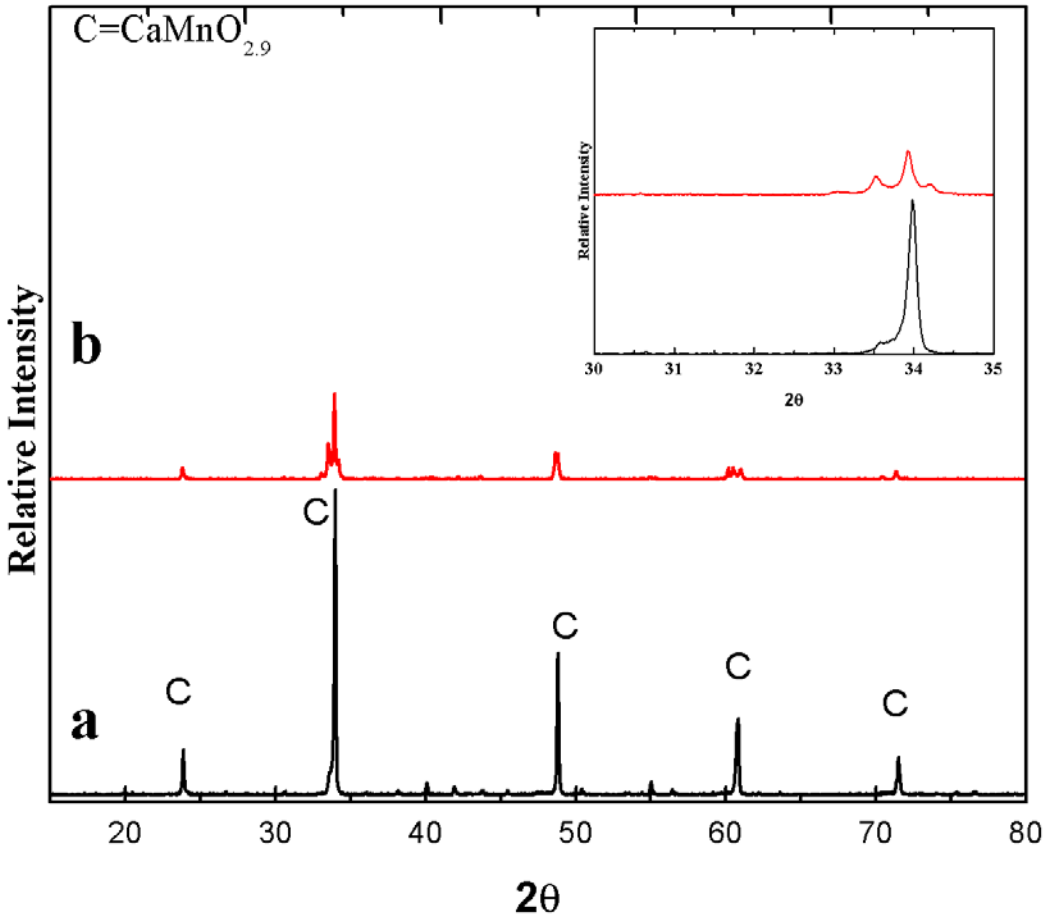

Figure 3-49 XRD patterns of $CaMnO_{3-\delta}$ soaked at 950°C for 3 h (a) in air (b) in N_2. The inset shows zooming at the main peak

According to XRD analysis the main phase after the heat treatment process in N_2 is $CaMnO_{2.5}$. Therefor Equation 2 can be rewritten as Equation 3:

Equation. 3 $2CaMnO_{2.9} \rightarrow 2CaMnO_{2.5} + 2/5O_2$

In this way the loss will be 4.5 wt. % which is much closer to the calculated data.

Figure 3-50 shows the XRD pattern of the doped perovskites, which were heat treated at air and nitrogen at 950°C for 3 hr. As it can be seen from the figure, in all cases, a single phase was formed. According to XRD database, this phase has calcium manganate ($CaMnO_3$) perovskite structure which is doped with lanthanum at A site and iron, titanium, aluminum, or zirconium ions at B site.

In the case of A- and B-site-doped particles (CLMT, CLMF, and CLMZ), the XRD patterns looked very similar to each other in all cases, without any evidence of another residual phase, indicating that the stoichiometry of the precursor was correct for the production of the perovskite structure.

Besides the ionic radii requirements, another condition to be fulfilled is electroneutrality, that is the sum of charges of A and B equals the total charge of oxygen anions. This is achieved by means of suitable charge distribution of the form $A^{1+}B^{5+}O_3$, $A^{2+}B^{4+}O_3$, or $A^{3+}B^{3+}O_3$. In addition to this, partial substitution of A and B ions is allowed, thus yielding an excess of compounds while preserving the perovskite structure. However, deficiencies of cations at the A- or B-sites or of oxygen anions are common, which results in defective perovskites. Oxygen vacancies are more common than those involving cationic vacancies [109]. In Figure 3-50 insets the main peak shifts of the XRD pattern are shown. In reality instead of manganese ions (Mn^{4+}), iron or aluminum ions (Fe^{3+}, Al^{3+}) incorporate into perovskite lattice and carry a shortage of positive charge into the lattice and this should be compensated. Compensation can be affected by formation of oxygen vacancies ($V[O^{2+}]$). Formation of oxygen vacancies will contract the lattice and then lead to shifting the Bragg reflections to the higher wavelength.

On the other side, replacing ions with different sizes will result in lattice expansion or contraction. The order of ionic size of ions which were used in this study is as follows: Mn^{4+} < $Al3^{+}$ < Fe^{3+} < Mn^{3+} < Ti^{4+} < Zr^{4+}. As it can be seen, zirconium ions are bigger than the others which may result in higher lattice distortion with respect to the others and lead to Bragg shift to the left as it can be seen in Figure 3-50.

Figure 3-50 shows the XRD pattern of the doped perovskites which were heat treated in N_2 as well. As it can be seen in all cases Bragg's reflections shift to higher wavelengths excluding Ti doped samples. This shift was attributed to two possible mechanisms, explained as follows:

If the oxygen atom is either in the interstitials lattice position or in octahedral positions, the lattice will shrink as a result of oxygen release from the structure by the following concept; in the former case the lattice which is forced to expand as a result of oxygen incorporation will back to its original position and consequently the lattice will contract. In the latter case, the neighbor ions try to tilt or bend the lattice in order to fill the oxygen vacancy positions[142]. In this way the lattice again goes a contraction process. Therefore, as it can be seen form Figure 3-50 in all cases, the XRD peaks shift to the right according to the Bragg law.

In case of Al and Zr this shifts are related to the RO capacity of the structures as these ions do not change their size in reduction or N_2 atmosphere. This is consistent with the results from TGA analyzes, suggesting that RO capacity of these materials orders in the following direction: CLMA> CLMZ).

This indicates that there is more shift to the higher wavelength or more lattice contraction as results of oxygen removal from the lattice structures. On the other hand, as iron is a multi-valence element, it will prefer to change its valence during the oxidation or reduction steps. This

can bring trickier situation to the theory. Iron size can change from 55 to 61 pm during the oxygen removal step. Therefore, the lattice will expand, while the oxygen is leaving the lattice and the structure prefers to fill its empty position. It seems the Braggs shifts will not relate to RO capacity directly in this case. This explains the reason for low Braggs shift in iron doped samples while they have the highest RO capacity among the others.

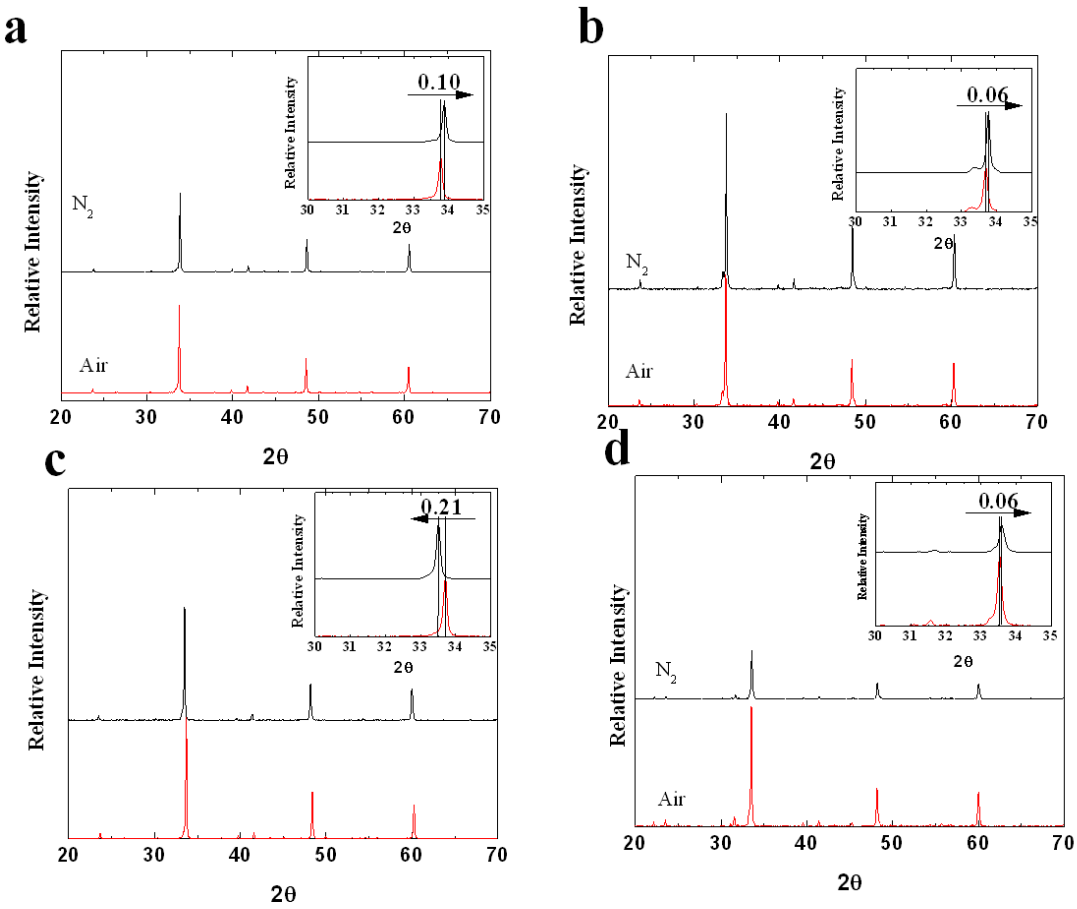

Figure 3-50 XRD patterns of fresh (after synthesis) and N_2 treated (950°C for 3 h) for CLMA (a), CLMF (b), CLMT(c) and CLMZ (d). The inset shows zooming at the main peak

Finally, in Ti^{4+} doped samples unlike the other doped samples the lattice expands, while the oxygen leaves the lattice. It seems the lattice pinned to it is positions and there is no large movement of ions inside the lattice. In this case, persisting oxygen inside the lattice brings the bands closer to produce the perovskite structure. In N_2 atmosphere when the oxygen leaves the lattice the bonds prefer to go to their original position and relax the stress induced by oxygen

bonding. In all doped samples the splitting of the main peak was not significant. This may show the structure is more stable and did not tilt as much as undoped samples. As a result, doped samples are more stable and they are not prone to segregation.

2.6 Iron-based perovskites as oxygen carriers

As previously mentioned due to shortcomings of $CaMnO_3$, different approaches have been followed to improve the redox properties of this material and lower its production costs.

One proposed approach is using iron as the B-site cation (instead of manganese) to evaluate the redox properties compared to $CaMnO_3$. Hence, $CaFeO_3$ was synthesized as the base material. The XRD results as shown in Figure 3-51 reveal that $Ca_2Fe_2O_5$, a brownmillerite structure, instead of $CaFeO_3$ has been formed. Brownmillerite structures have the general formula of $A_2B_2O_5$. They usually are known to have two dimensional layers of BO_4 corner-shared tetrahedral and BO_6 corner-shared octahedral. A general schematic of brownmillerite structure is shown in Figure 3-52. It is known that at high defect concentrations, it is energetically desired for the structure to add two vacancies in one octahedron resulting in a brownmillerite structure [143]. The observation in XRD patterns is due to high defect concentration in the structure which shows that calcium has a low ionic radii (1.34 Å) to fit the A-site in the structure. It is of great importance to know that the preparation method plays an important role in surface physicochemical properties, surface area, porosity, purity, stability, and crystal size. The synthesis method can be another reason for calcium not being incorporated into the structure.

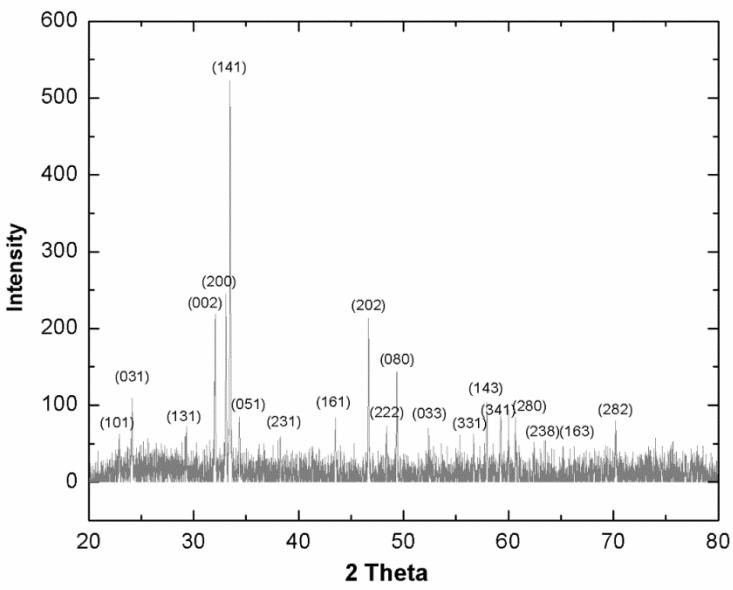

Figure 3-51 XRD results obtained for $Cr_2Fe_2O_5$

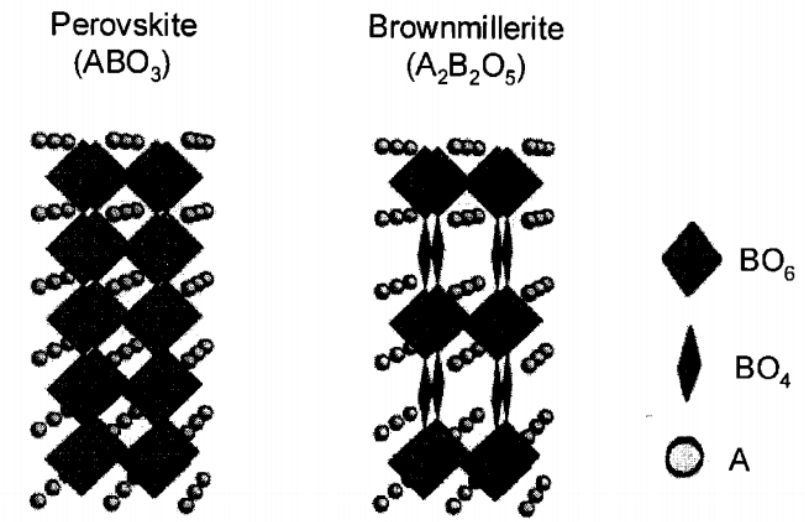

Figure 3-52 Brownmilllerite structure ($A_2B_2O_5$) and perovskite structure (ABO_3) [144]

It is obvious that calcium needs to be replaced with a cation with larger ionic radii. Substitutions were chosen in different sizes to assess how this parameter affects the structure and performance of the oxygen carriers.

A-site cations in perovskites are usually chosen from group IA and IIA in the periodic table because of their relatively large ionic radius. Since metals in the first group possess low melting

temperatures (which makes them undesirable for CLC purposes), the A-site choices are going to be from group IIA.

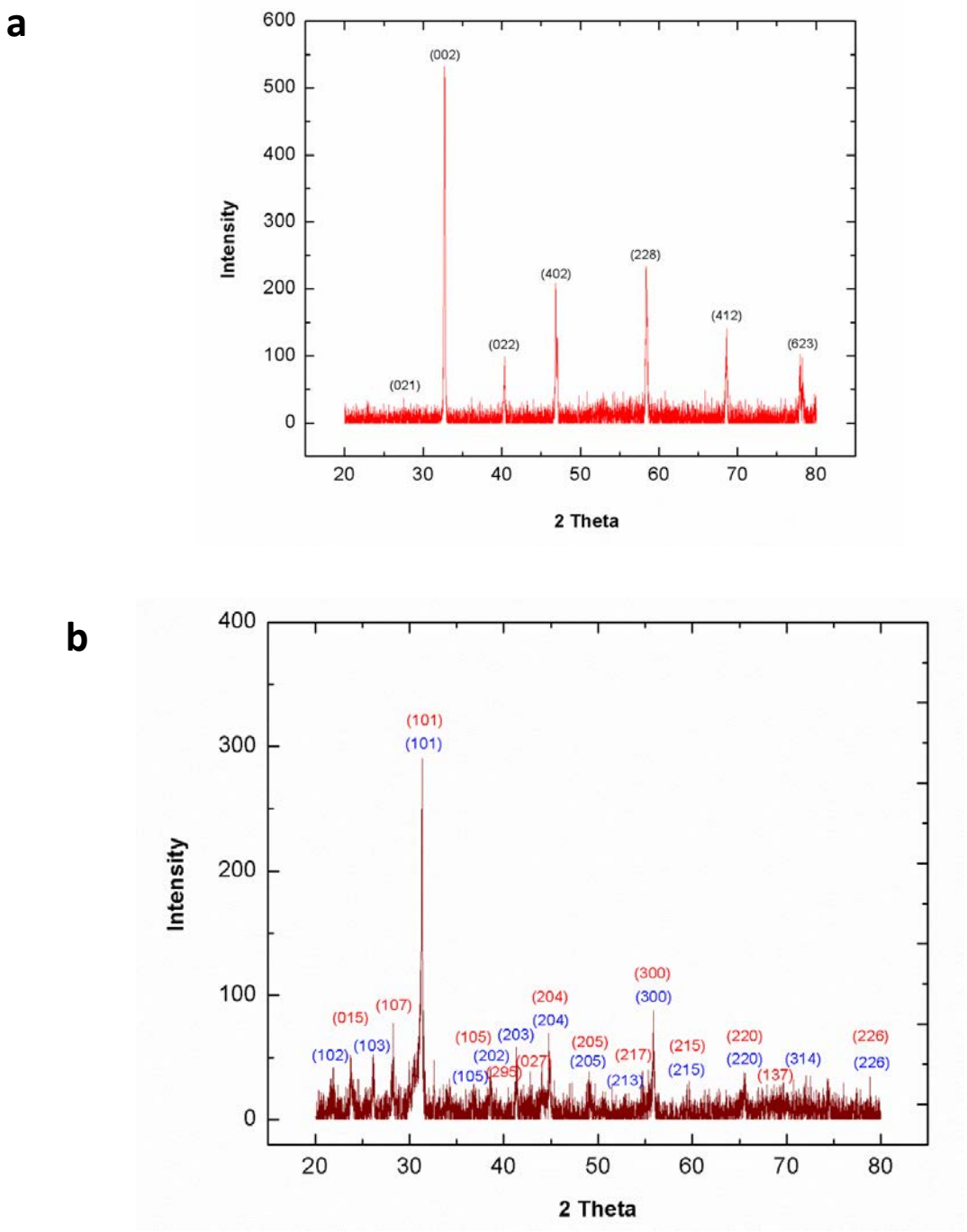

Figure 3-53 XRD results for (a) $SrFeO_3$ and (b) $BaFeO_3$ perovskites, the blue color represents perovskite $BaFeO_3$ and the red color shows $BaFeO_3$-Delta phase

In this group, Strontium and Barium are the only choices of higher ionic radii than calcium. $SrFeO_3$ (SF) and $BaFeO_3$ (BF) were synthesized to evaluate the size effects of A-site cations. The XRD results are shown in Figure 3-53.

As is shown in Figure 3-53-a, $SrFeO_{3-\delta}$ is proven to be a perovskite structure with no additional phase present with the formula of $SrFeO_{2.75}$. Figure 3.53.b, on the other hand, represents impurities present along with $BaFeO_3$. As mentioned before, the synthesis method can have a huge effect on the perovskite materials by affecting the crystal size, surface area, porosity, purity, and stability. Hence, Barium not being incorporated to the structure can be a result of the chosen synthesis method. This phenomenon can also be explained by the large ionic radius of Ba^{2+} (1.61 Å). It has been proven that $BaFeO_3$ has high oxygen permeability due to its relatively large lattice free volume. However, as shown by current XRD results, using a great amount of this cation in perovskite structure results in structure deterioration and a decrease in structural stability [145]. For this reason, the lattice enlargement abilities may be employed by using it as a dopant on the A-site in low quantities.

So far, $SrFeO_{3-\delta}$ has proven to be a potential basis candidate for further modifications of the iron-based perovskites. The thermogravimetric analysis (TGA) of this material in comparison with $CaMnO_3$ is shown in Figure 3-54. It can be concluded from the TGA results that both structures need improvement in terms of stability since their oxygen capacity differs from cycle to cycle.

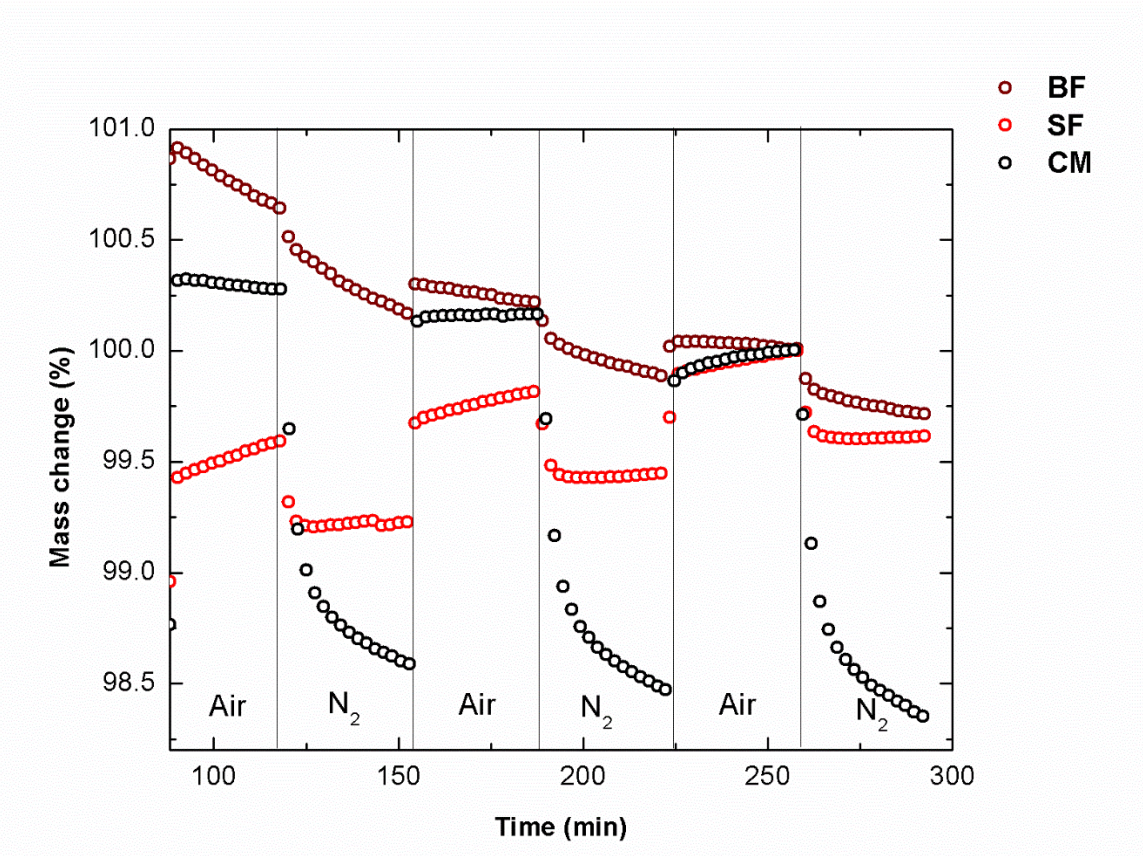

Figure 3-54 TGA results obtained for $CaMnO_{3-\delta}$ and $SrFeO_{3-\delta}$. It is evident that SrFeO3-δ needs further modifications to reach the oxygen capacity of $CaMnO3-_{\delta}$.

As expressed in earlier chapters (chapter two), one strategy to increase the oxygen release of a perovskite is adding dopants to the A and B-site cations. The following sections present the results obtained by doping the A and B-site cations with different cations of various charges and sizes.

As mentioned earlier, B-site cations are influential in oxygen transport properties of the perovskite structure on account of their multivalent nature. If used properly and in the right amount (depending on other materials incorporated in the structure and ambient atmosphere characteristics) their role in performance enhancement of oxygen carriers will be substantial. As a result the choice of B-site dopant can be as important as the choice of B-site cations. B-site

cations are usually selected by following criteria: size, charge, electron configurations and redox properties. The choice of B-site dopants in this study was based on the proximity of ionic size of the B-site and the dopant to ensure the crystal structure stability of the compounds.

Titanium is chosen as one of the B-site dopants. This material as shown by Hallberg et al. [29] can be incorporated as a B-site dopant on $CaMn_{1-x}M_xO_{3-\delta}$ (M = Ti, Fe, Mg) structure. Doping Ti on the B-site has also been proven to be beneficial for the reactivity improvements by Arjmand et al. as well [146]. Consequently choosing it as a B-site dopant on Fe-based perovskites may also be beneficial. Manganese has also been chosen for B-site substitution. This material has been employed as the B-site cation in many studies and is one of the best candidates. Hence using it as a B-site dopant can also be of importance. Aluminum is not a transition metal with a multivalent nature. However, this material was chosen to be doped on the B-site. Using Al on the B-site can be effective on the performance of the perovskite structure mainly because it has one valence state (3+). Incorporating Al^{3+} can carry a shortage of positive charge into the lattice and this should be compensated. Compensation can be affected by formation of oxygen vacancies. This can allow for more oxygen release during reduction ($Fe^{4+} \rightarrow Fe^{3+} + O_2$).

Due to its toxic nature and high cost, Cobalt is not usually considered as a viable option for perovskite synthesis for CLC purposes especially at an industrial scale. However, if Cobalt doped perovskites are effective enough and cobalt effects on the oxygen carrier performance are significant, its advantages can over weigh its disadvantages since this material has proven to be influential in oxygen carrier performance in many studies [35, 37, 147].

Several formulations were synthesized with partial substitution of the B-site with Ti, Al, Co and Mn by10 mol%. The XRD results are shown in Figure 3-55. It can be observed from the XRD results demonstrated in Figure 3-55-a, that all synthesized materials have the same crystal structure as the base perovskite, $SrFeO_3$. The main peak shifts are also shown in Figure 3-55-b.

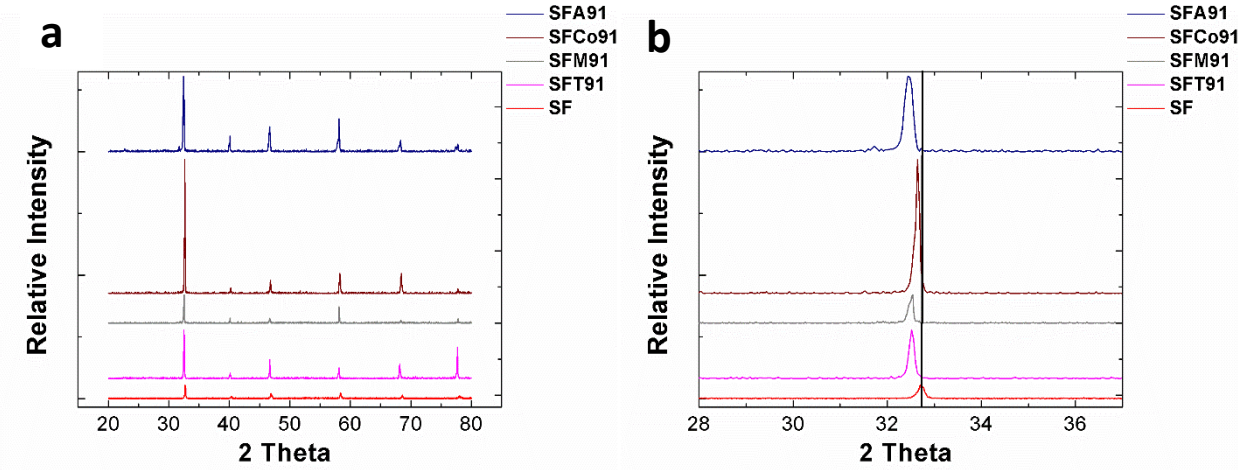

Figure 3-55 (a) Comparative XRD results for B-site doped oxygen carriers (b) zooming on the main peaks. Comprehensive information on the elements used in the above-mentioned structures is presented in Table 3-1.

The information provided in Table 3-17 facilitates the way towards better understanding of the elemental behavior in the synthesized structures. As shown in XRD results (Figure 3-55-a), all materials have shown the similar XRD pattern as $SrFeO_{2.75}$. However, according to Figure 3-55-b, a peak shift to the left is observed for all the prepared samples. According to Bragg's law, since θ has been reduced, the d-spacing in the structures should have been increased. One main reason for changes in d-spacing can be lattice contractions and expansions caused by adding dopants and modifying the structure.

Table 3-17 . Information on the most common oxidation states and electron configurations of elements incorporated in the perovskite structure

Element name	Atomic Number	Common oxidation states	Electron configurations	
Aluminum (Al)	13	3+	1s22s22p63s23p1	$\frac{\uparrow\downarrow}{1s}\ \frac{\uparrow\downarrow}{2s}\ \frac{\uparrow\downarrow}{1}\ \frac{\uparrow\downarrow}{2p}\ \frac{\uparrow\downarrow}{1}\ \frac{\uparrow\downarrow}{3s}\ \frac{\uparrow}{1}\ \frac{1}{3p}\ \frac{1}{1}$
Cobalt (Co)	27	2+,3+	Ar]4s23d7]	[Ar] $\frac{\uparrow\downarrow}{4s}\ \frac{\uparrow\downarrow}{1}\ \frac{\uparrow\downarrow}{1}\ \frac{\uparrow}{3d}\ \frac{\uparrow}{1}\ \frac{\uparrow}{1}$
Manganese (Mn)	25	2+,3+,4+,6+,7+	Ar]4s23d5]	[Ar] $\frac{\uparrow\downarrow}{4s}\ \frac{\uparrow}{1}\ \frac{\uparrow}{1}\ \frac{\uparrow}{3d}\ \frac{\uparrow}{1}\ \frac{\uparrow}{1}$
Titanium (Ti)	22	4+	Ar]4s23d2]	[Ar] $\frac{\uparrow\downarrow}{4s}\ \frac{\uparrow}{1}\ \frac{\uparrow}{1}\ \frac{1}{3d}\ \frac{1}{1}\ \frac{1}{1}$
Iron (Fe)	26	2+,3+	Ar]4s23d6]	[Ar] $\frac{\uparrow\downarrow}{4s}\ \frac{\uparrow\downarrow}{1}\ \frac{\uparrow}{1}\ \frac{\uparrow}{3d}\ \frac{\uparrow}{1}\ \frac{\uparrow}{1}$

Information on the Ionic radii of the cations can be useful information in this matter. The ionic radius of cations with coordination number of 6 are reported by Dronskowski and Hoffmann [148] and are shown in Table 3-18.

Table 3-18 Possible Ionic radius of cations incorporated in B-site

Element name and symbol	Oxidation state		
	Ionic Radii (Å)		
Aluminum (Al)	3+		
	0.535		
Cobalt (Co)	4+	3+	2+
	0.530	0.61	0.745
Manganese (Mn)	4+	3+	2+

	0.53	0.645	0.83
Titanium (Ti)	4+	3+	2+
	0.605	0.670	0.860
Iron (Fe)	4+	3+	2+
	0.585	0.645	0.780

By considering the ionic radius of Al^{3+}, it can be expected that since this cation has a shorter ionic radii than iron, there should have been lattice contraction and a peak shift to the right. However, it is observed otherwise. This incident can be because of the change in valence of iron when associated with aluminum. Since iron has larger ionic radii in smaller oxidation states, the lattice expansion can be justified.

In case of Cobalt as the B-site dopant, since oxidation states of 3^+ and 2^+ are more common and easily transferrable to one another, the increase in d-spacing can be explained. Titanium with the oxidation state of 4^+ being the most common is expected to expand the lattice and consequently increase d-spacing.

Doping manganese has also been a reason for lattice expansion. Since Mn^{4+} can be produced from Mn^{3+} more easily than Fe^{4+} from Fe^{3+}, it seems like manganese has changed iron's oxidation states to a lower quantity (2 or 3). As a result the d- spacing has increased and the observation is reasonable.

TGA is the next step to evaluate the performance of the synthesized materials. The TGA results are shown in Figure 3-56. As is shown in Figure 3-56, the TGA results comply with the XRD results. Since aluminum has decreased iron's oxidation state, the oxygen release capacity

of the structure has decreased substantially. The Cobalt doped structure on the other hand, shows noticeable oxygen release increase compared to $SrFeO_{2.75}$. This is because cobalt can change states between 2 and 3 easily and it has caused iron to be at higher oxidation states which is a result of high oxygen transport. In case of manganese doped structure, manganese is acting as the multivalent cation since its oxidation states are easily transferable. Hence, iron is acting as a fixed valence cation facilitating oxidation and reduction of manganese and resulting in the highest oxygen capacity. However, the titanium doped structures do not show significant oxygen release in an inert atmosphere. The main reason can be explained by XRD results. Since this material does not change states easily and it has lowered the oxidation state of iron, the oxygen capacity of the structure has decreased substantially (in the same order of magnitude as the aluminum doped structure).

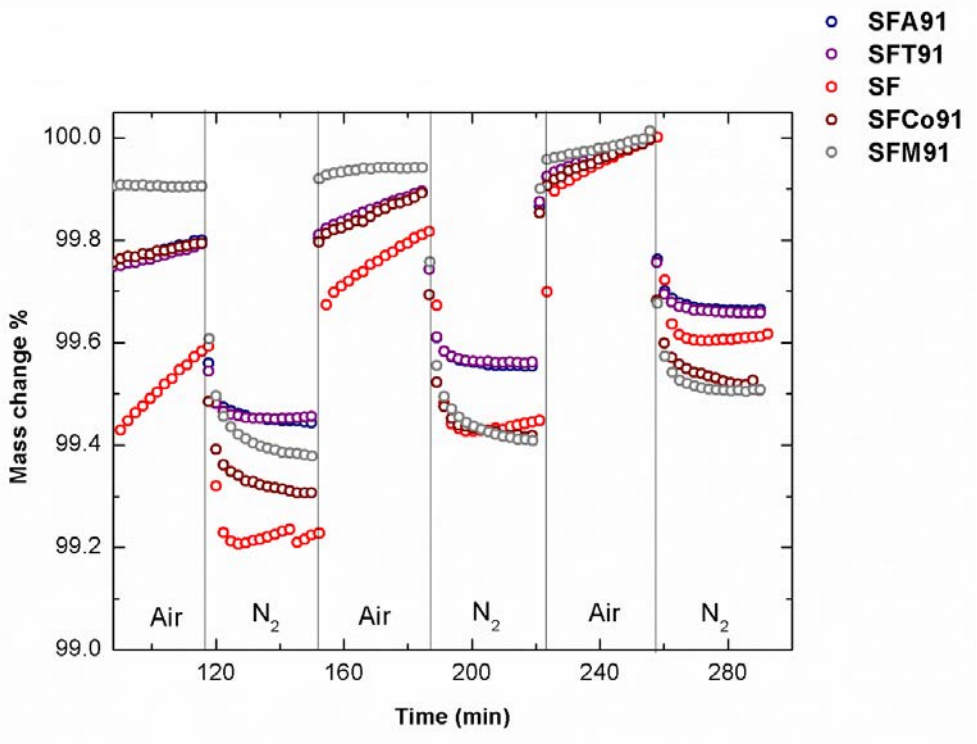

Figure 3-56 TGA results for B-site doped samples

Manganese doped structures possessed the highest oxygen capacity. As a result, adding more manganese was proposed. Manganese was doped on the original structure in amounts of 20 and 30 %. The XRD results and TGA results are shown in Figure 3-57 and Figure 3-58 respectively.

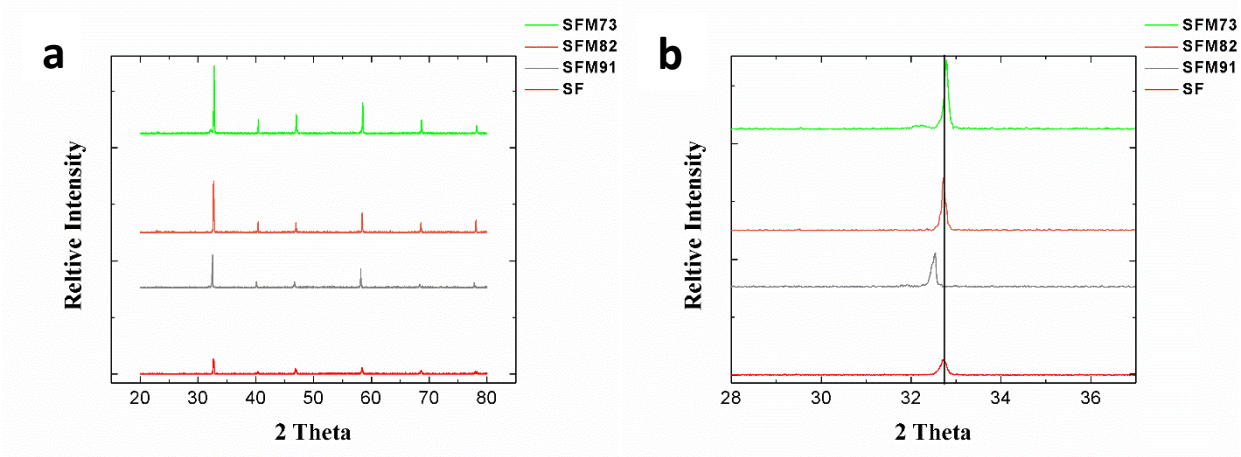

Figure 3-57(a) XRD results for manganese doped structures in comparison with $SrFeO_{2.75}$ (b) zooming at the main peak

Figure 3-57-a demonstrates the perovskites with 10, 20 and 30 mol % manganese doped in their structures. As is shown, all of the XRD patterns are similar to the parent compound $SrFeO_{2.75}$. The XRD patterns shown in Figure 3-57-b indicate different amounts of lattice contraction and expansion with different amounts of doped Mn. As testified by the previous XRD results, manganese forces iron to its lower oxidation state and this results in lattice enlargement. However, as the amount of manganese in the structure increases the amount of Mn^{4+} (which has a shorter ionic radii) in the perovskite oxide increases. This can result in a lattice contraction and consequently a shift to the right for the amount of 30 mol%.

It can be observed from the TGA results (Figure 3-58) that as the amount of manganese in the structure increases, the amount of oxygen capacity increases as well. As mentioned before, manganese has a more effortless change of valence in comparison with iron. Hence, in

manganese doped structures, iron will act as a single valence cation facilitating the way for manganese to change its valence upon oxidation and reduction and towards a more stable structure. This will lead to a structure with more oxygen capacity and enhanced oxygen transfer properties. The stability of the $SrFe_{0.7}Mn_{0.3}O_{3-\delta}$ is clearly shown in TGA results as this material did not change its oxygen release amount during three oxidation and reduction cycles. As it is obvious, the amount of doped manganese directly correlates with the oxygen capacity of the structure. This means that adding more manganese to the structure definitely has a positive effect on the oxygen transport properties. However, by using more Mn in the structure, the perovskite will be a Mn-based perovskite and this was not the aim of the approach. The comparison with the parent compound $SrFeO_{3-\delta}$, the base compound $CaMnO_{3-\delta}$ and the $SrFe_{0.7}Mn_{0.3}O_{3-\delta}$ in terms of oxygen capacity is shown in Figure 3-59.

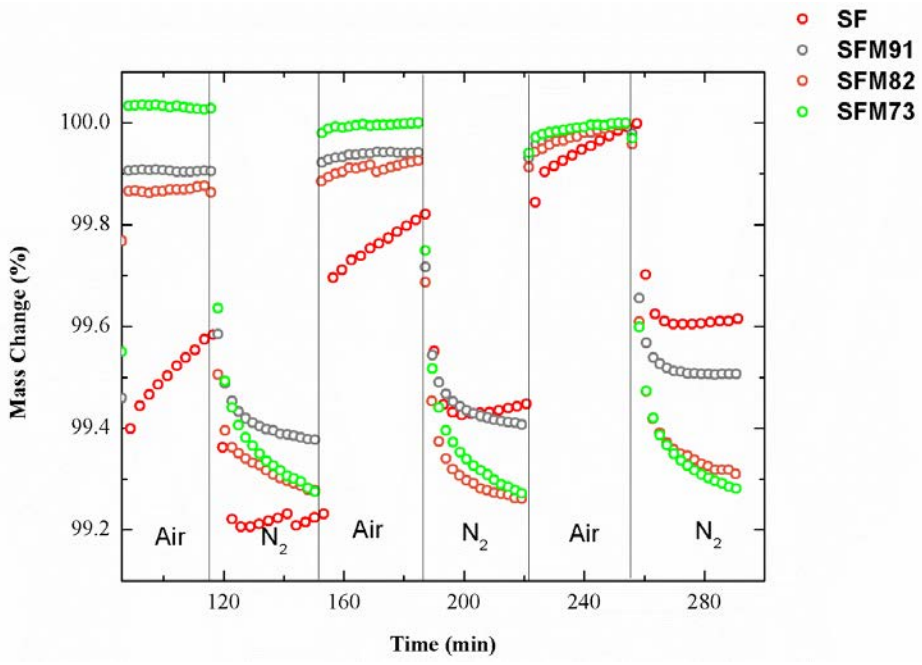

Figure 3-58 TGA results for manganese doped perovskites with 10, 20 and 30 mol% manganese compared to the parent compound

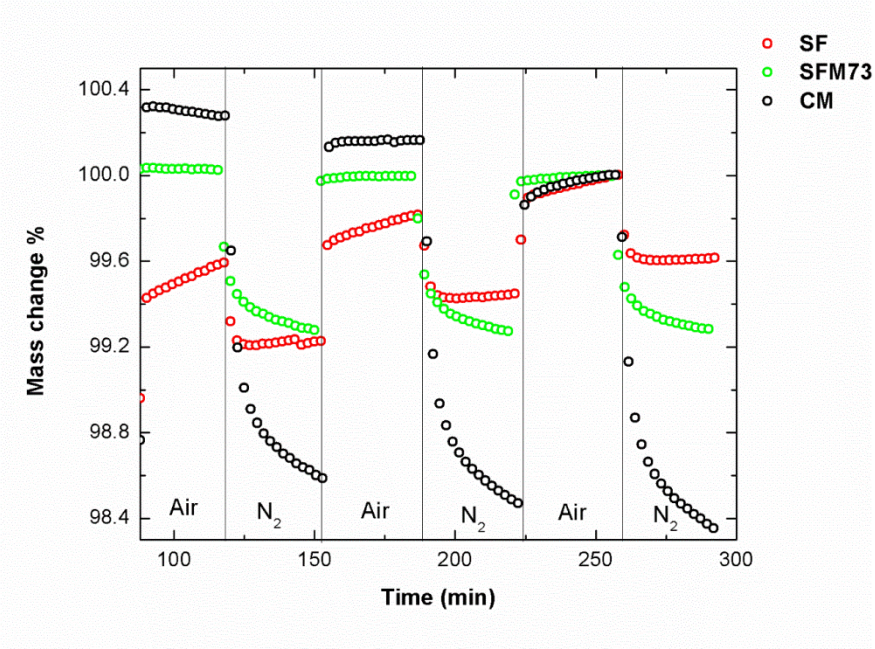

Figure 3-59 TGA results, a comparison between SFM73, the parent compound SF and the base compound CM

As is demonstrated above, the synthesized oxygen carrier SFM73, has clearly achieved enhanced oxygen transport properties compared to the parent compound. This structure shows more mass change in an inert atmosphere and has shown to be more stable during three oxidation and reduction cycles. However, there is still a relatively large gap between the oxygen capacity of SFM73 and $CaMnO_{3-\delta}$.

2.7 Extended operation CLC using perovskites as oxygen carriers

2.7.1 XRD Results

Figure 3-60 and 61 show the XRD results of CM and CSMF before and after extended runs respectively. As it can be seen, the peaks are splitting in CM sample. This is due to transformation from cubic to orthorhombic structure. In other word, the structure is undergoing huge changes, which is from single perovskite to double perovskite structure.

The XRD result of CSMF shows the structure did not change after 150 cycles and all the peaks remain unchanged before and after the test.

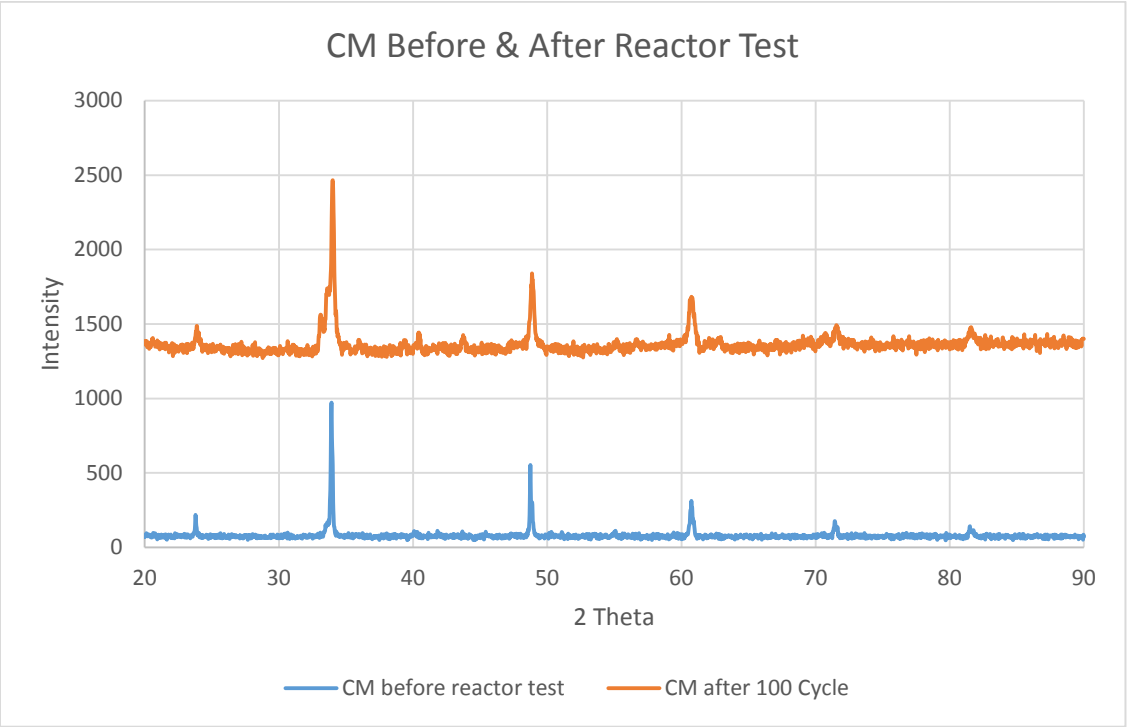

Figure 3-60 XRD Results of CM Before and After 100 Cycles

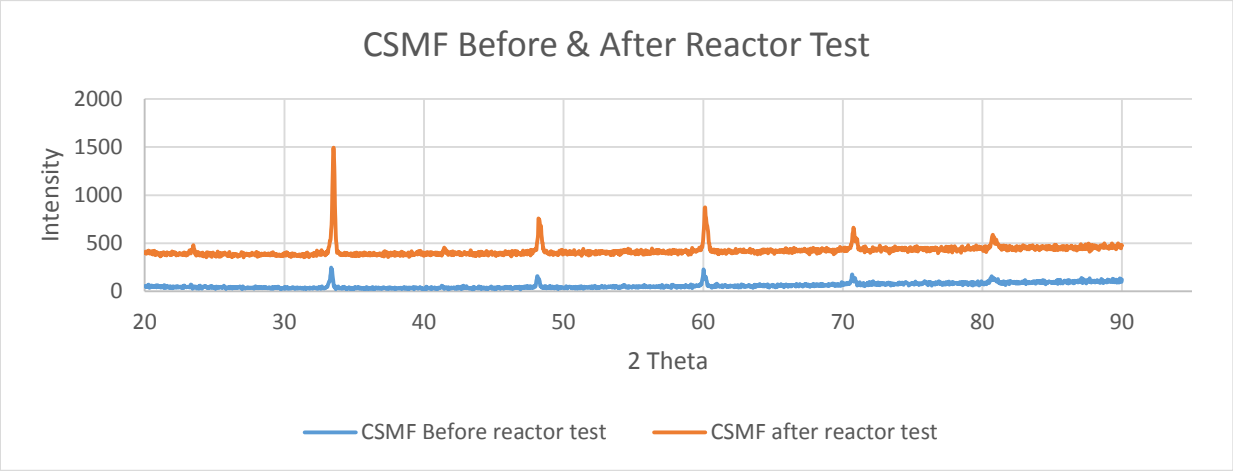

Figure 3-61 XRD Results of CSMF before and after 150 Cycles

2.7.2 SEM Results

SEM images (Figure 3-62) shows that the size of CM particles has decreased after reactor test and there are considerable amount of fine particles in the after test samples. This observation confirms that the mechanical strength of CM particles was not sufficient. Therefore, particles break down to smaller particles because of collision and attrition inside the fluidized bed reactor.

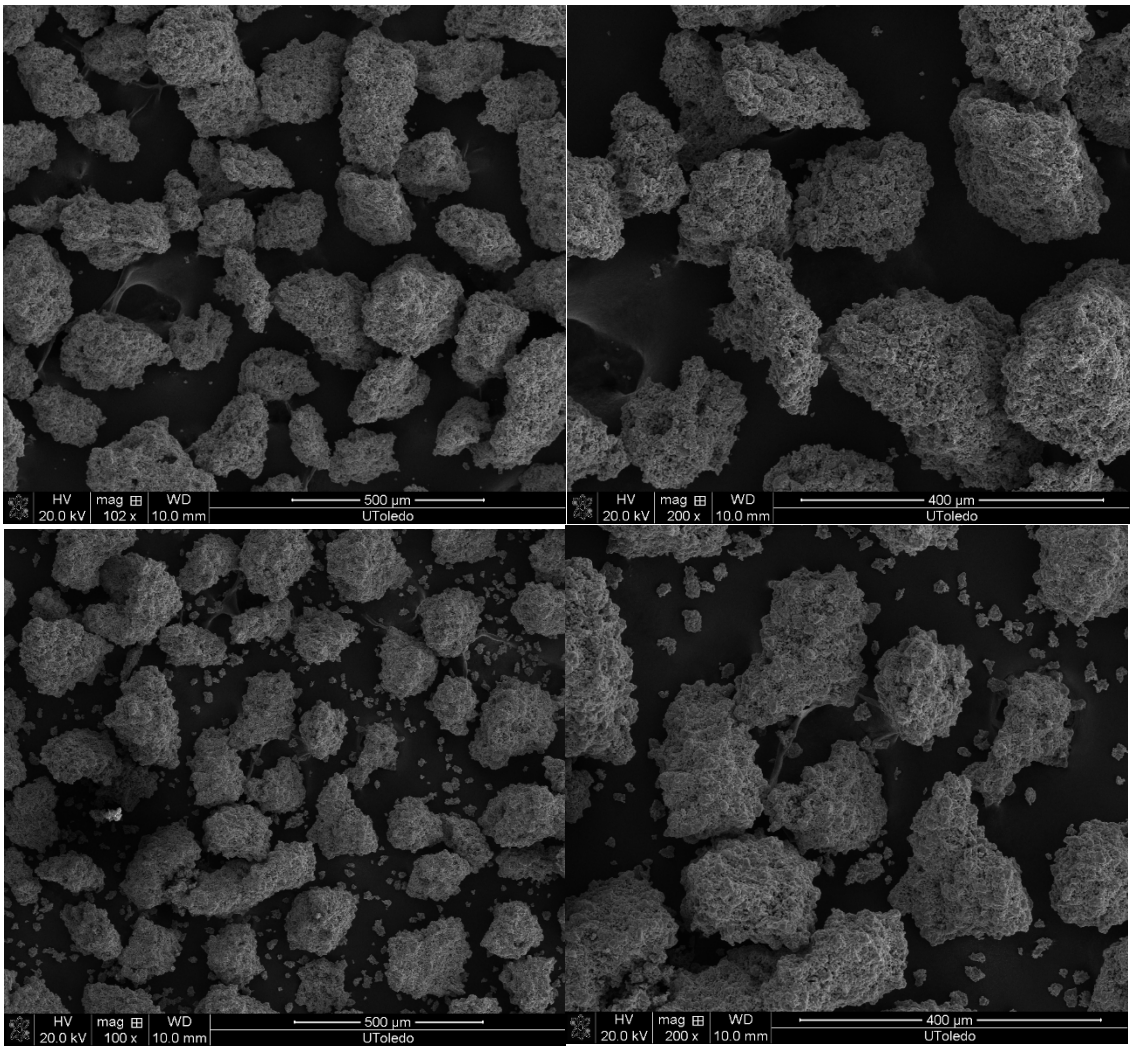

Figure 3-62 SEM images of CM before and after reactor test in two different magnitudes: 100x, 200x,

The SEM images of CSMF carriers before and after reactor testes are shown in Figure 3-63. The size and porosity of carriers do not show obvious change. Moreover, the amount of fine particles after reactor test is negligible. This observation confirms the mechanical stability of CSMF particle compare to the CM particles.

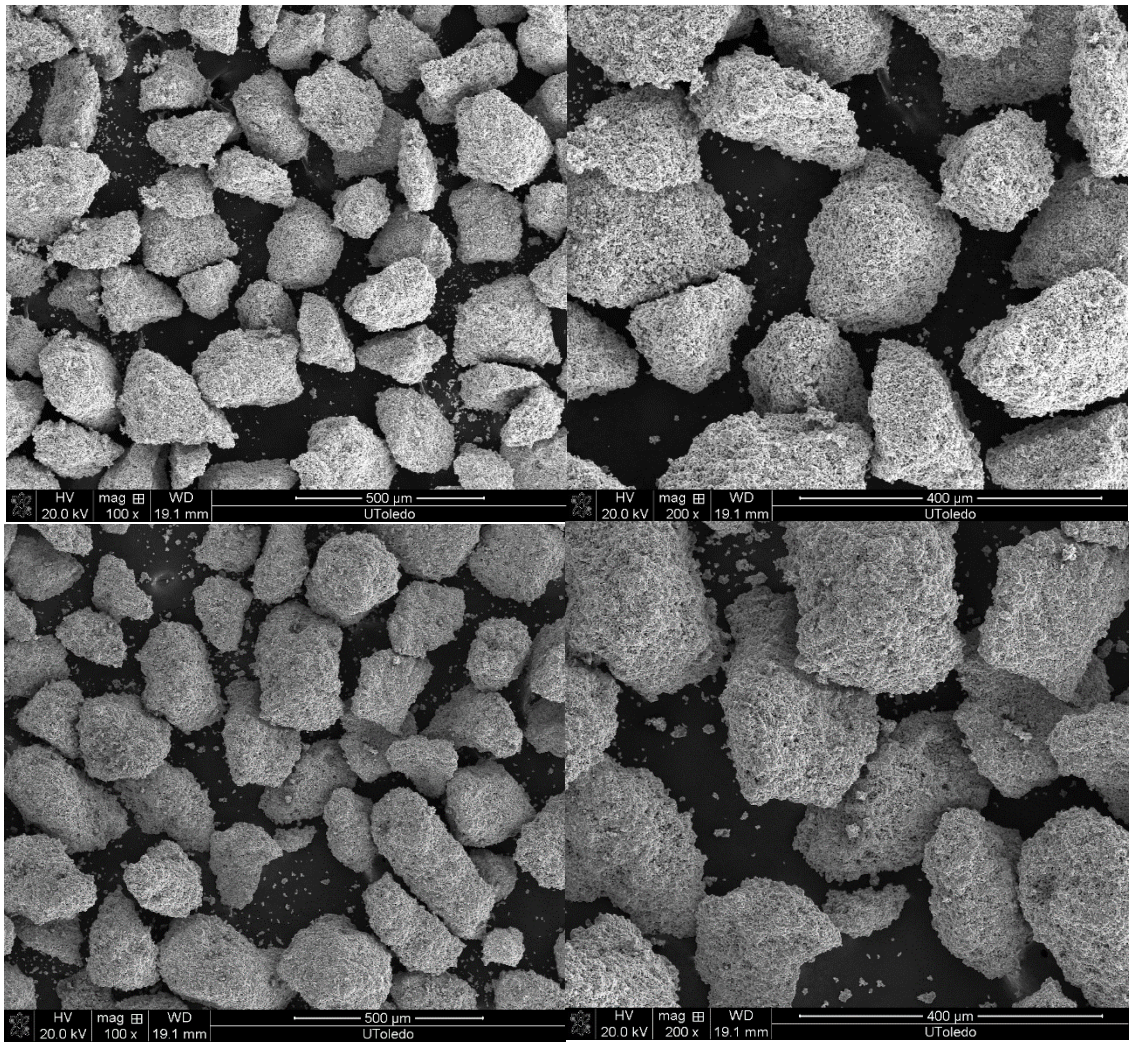

Figure 3-63 SEM images of CSMF before and after reactor test in two different magnitudes: 100x, 200x

2.7.3 TGA Results

The mass change of oxygen in the samples assigned to the oxygen carrying capacity (RO) of the carriers and defined as follows (Eq.10):

$$R = \frac{(mox - mred)}{mox} \quad (10)$$

Where mred and mox are the masses of the oxygen carrier in oxidized and reduced states, respectively.

Figures 3-64 and 65 show the oxygen capacity of the materials before and after the extended reactor tests. In Figure 3-64, RO varies between 3.5 and 2.5 for CM particles, and 2 and 3.5 for CSMF particles before and after the extended tests respectively. This decrease and increase in oxygen capacity was expected due to unstable structure of CM particles confirmed by XRD results.

.

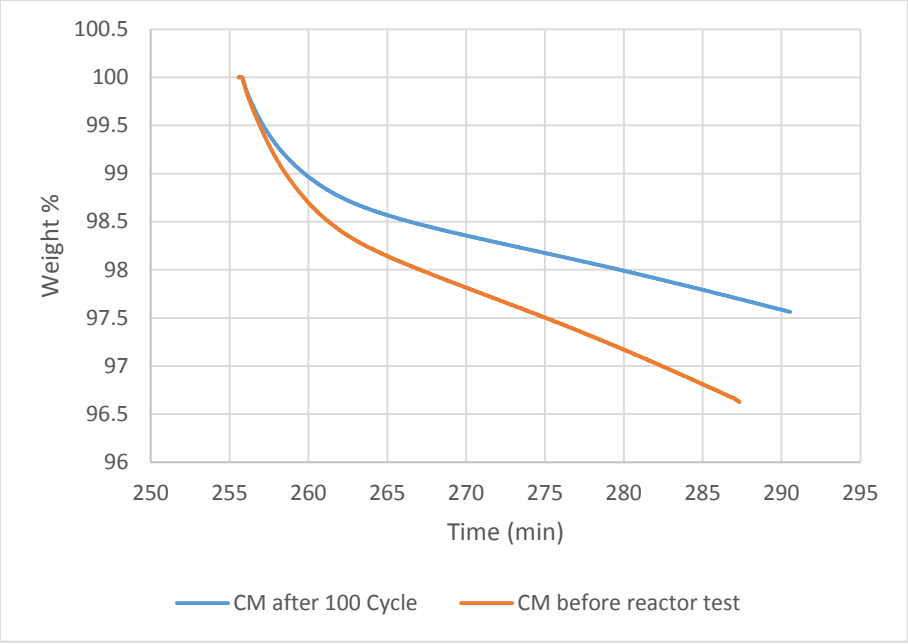

Figure 3-64 TGA Results of CM before and After 100 Cycles

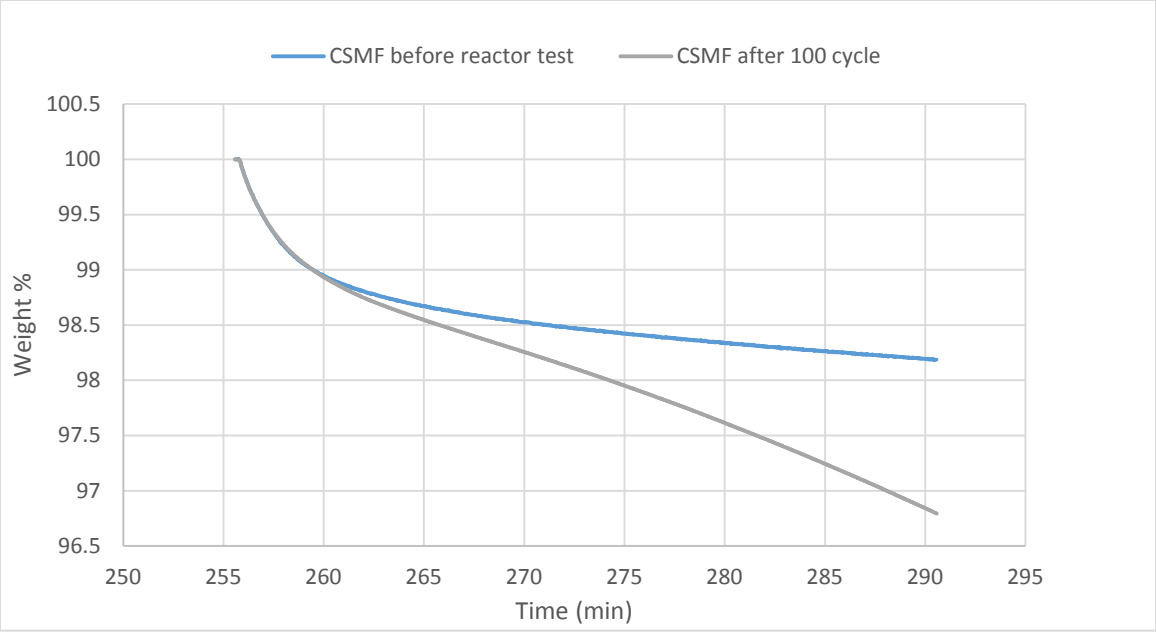

Figure 3-65 TGA Results of CSMF before and after 100 Cycles

2.7.4 BET Results

Table 3-19 shows the surface area of CM and CSMF particles measured by the BET instrument. The surface areas of CM particles decreased by 40%, while the CSMF surface area reduced by only 15%.

Table 3-19 BET of the Oxygen Carriers before and after the Reactivity Test (±0.1 error)

Sample	BET Surface Area
CM – Before Reactor Test	1.0 m^2/g
CM – After Reactor Test	0.6 m^2/g
CSMF – Before Reactor Test	0.7 m^2/g
CSMF – After Reactor Test	0.6m^2/g

2.7.5 Reactor Data

The reactivity experiments are conducted at 950 °C, using methane as the fuel and 30 grams of the prepared particles in the reactor bed. The concentration profiles of O2, CH4 and CO2 during the combustion period, for oxygen carriers investigated in this study, are shown in Figures 3-66, 67, 68 and 69 respectively. Initially, the carriers are oxidized in a stream containing 8% O_2. In the next step when the oxidizing stream is switched with pure nitrogen (inert), the oxygen concentration decreases gradually corresponding to the way shown in the Figure 3-66 and 67.

When methane is purged to the reactor, CO_2 is produced as a result of methane conversion; Some uncombusted methane is detected in both cases (see Figures 3-68 and 3-69).

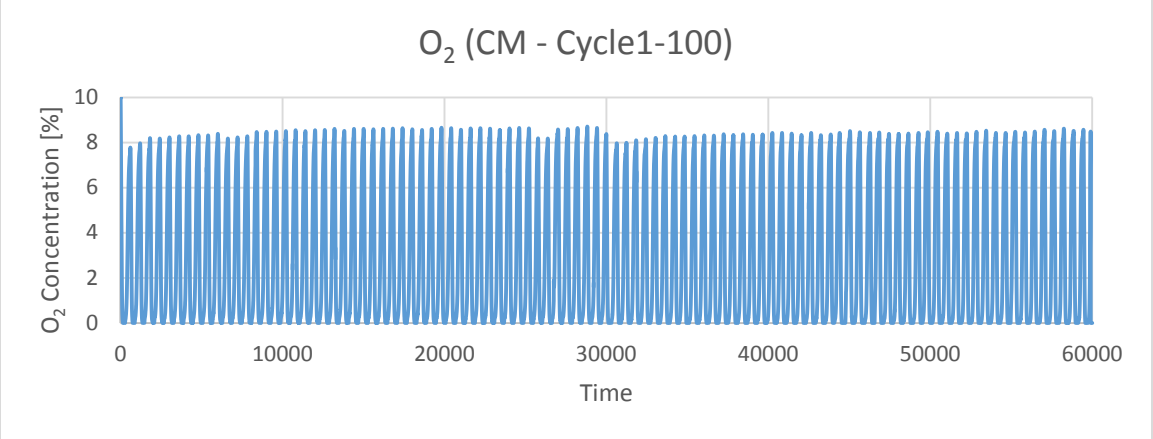

Figure 3-66 Oxygen Release Profile of CM

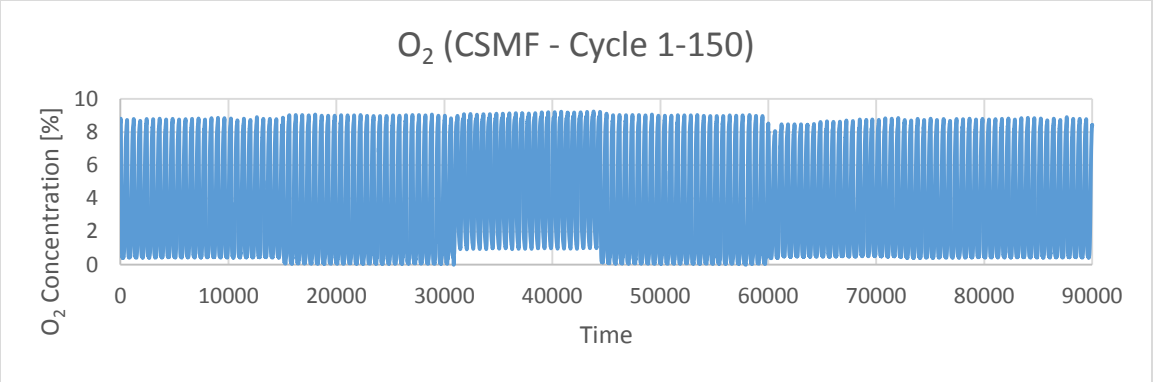

Figure 3-67 Oxygen Release Profile of CSMF

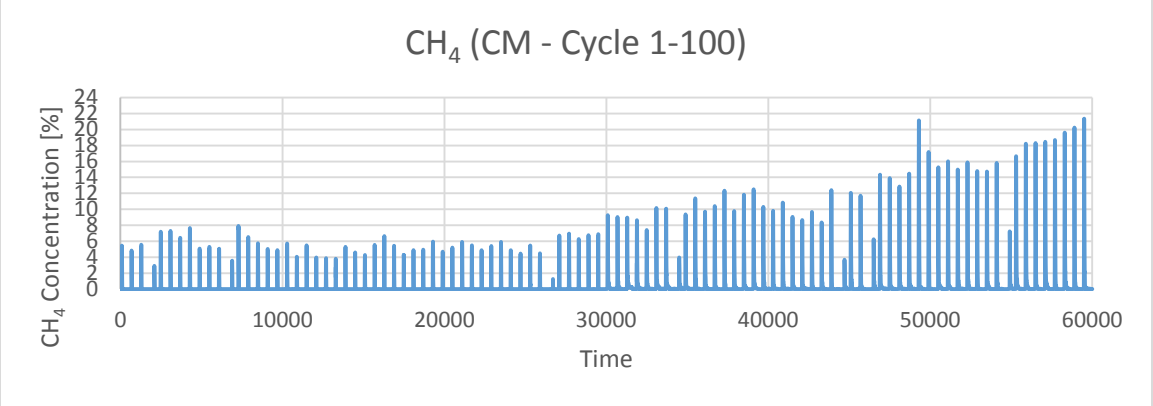

Figure 3-68 Uncombusted CH4 Profile of CM

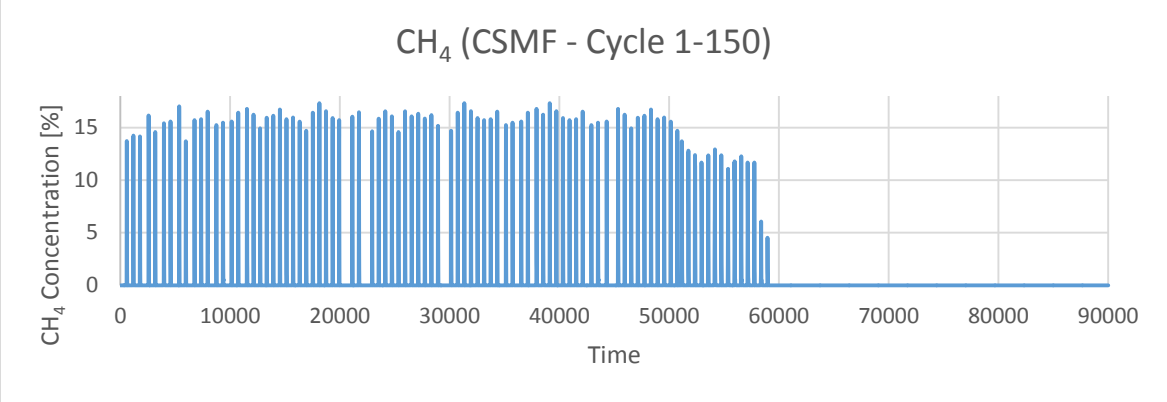

Figure 3-69 Uncombusted CH_4 Profile of CSMF

It can be seen from Figure 3-69 that the amount of uncombusted CH_4 decreases over time, which indicates CSMF particles has modified their structure to the more stable form. Therefore, complete combustion occurs during the last 50 cycles. This observation was supported

previously by the XRD and TGA analysis. CSMF carriers resulted in complete combustion of methane after 100 cycles whereas, the amount of uncombusted CH_4 increased by time in CM particles. This is supporting the fact that CM particles are decomposing over the time, while CSMF particles remain stable.

3 Conclusions

A series of novel doped perovskite-type oxygen carrier particles were synthesized by the tumbler mixing technique and characterized with XRD, TGA, SEM and Ft-IR techniques. It is shown that doping at A and B sites decreases the oxygen transfer capacities of the various investigated formulations. All single perovskite samples exhibited store and release oxygen behavior.

By using TGA analysis, a screening performed on a group of double perovskite material was synthesized in this project. Three systems were chosen for the next step of the project, including CSMF,CLMF and CM. A design of experiment methodology was employed to define the synthesis condition, dispersant concentration, pH, and mixing time. From the conducted experiments, one can conclude that there are some major factors that have effects on the amount of zeta potential and the dispersion of particles in slurry depending on the nature of the mixture and particles in it. These factors are pH, amount of dispersant and time of mixing. In our case (with specific oxides that are used in the slurry) it can be seen that better dispersion of the particles takes place in a basic environment in a higher amount (2.35g) of proper dispersant (NH4PAA) and in the right amount of time (3 hours).

Based on the surface area analysis, an optimum slurry composition for extruding porous perovskite structure was reported. The results showed that the starch amount in the composition

had an optimum value. In our case this value was 1.2 wt. %. In order to check the proposed slurry formula for other doping systems, a series of novel doped perovskite-type oxygen carrier particles were synthesized by the tumbler mixing technique which was followed by an extrusion and characterized with XRD, SEM, and TGA techniques. The results showed that the proposed composition was suitable for other doping systems as well and almost all the samples had the same surface area which is the main advantage of the extrusion technique. In addition, all the samples were single phase and there was no evidence of any other second or residual phase among the samples.

The results showed that doping strontium at A- site and iron at B- site will increase the oxygen capacity as well as sustainability of the perovskites during combustion of methane. Based on Iodometric titration results, manganese ions alter their electron valance to lower state while they exposed to nitrogen atmosphere. In $CaMnO_3$, more than 70% of Mn^{4+} ions converted to Mn^{3+}, while in doped samples it is between 10 to 50% which keep the structure firm.
Almost complete methane combustion was obtained at 950 °C for all doped and undoped samples. Neither particle fragmentation nor agglomeration was noticed during the experiments. Whereas the bed temperature did not show significant effect on CLOU behavior, it has a great effect on reaction of methane.

The integration of XRD, TGA, XPS, FTIR and Iodometric titration in our approach enabled us to gain a deeper understanding with respect to the relevant aspects such as effect of substitution on A and B sites, phase changes during cycling and microstructural stability. We demonstrated direct evidence of lattice expansion/contraction by using the lattice parameters deduced from high-resolution XRD patterns.

Based on Iodometric titration results, manganese ions alter their electron valance to lower state while they exposed to nitrogen atmosphere. In $CaMnO_3$, more than 70% of Mn^{4+} ions converted to Mn^{3+}, while in doped samples it is between 10 to 30%, which keep the structure firm.

We believe that the mechanisms that we identified to govern the cation segregation on the doped $CaMnO_3$ are actually applicable to a wider family of perovskite oxide structures.

Iron and manganese-based perovskites were investigated for their use in Chemical Looping Combustion processes. The materials were synthesized using solid state reaction followed by mechanical extrusion. The main objective of using such synthesis method was the mass production ability of it. The perovskite oxides were generally evaluated for their oxygen release, reactivity and performance. Detailed characterizations and analysis for synthesized oxygen carriers were implemented. $CaMnO_{3-\delta}$ is a perovskite material that due to its high oxygen capacity and low stability has been the subject of numerous studies. In this study, manganese has been replaced by iron which is of lower cost and the structure was doped on A and B-sites for performance enhancement.

Strontium and Iron doped calcium manganese perovskites ($SrFe_{0.9}Mn_{0.1}O_{3-\delta}$) and undoped calcium manganese perovskites were prepared as oxygen carriers in chemical looping combustion using extrusion followed by solid state reaction. The stability of such carriers in extended tests (100-150 cycles) is investigated. The tested samples were characterized before and after the long tests with XRD, SEM, BET and TGA analyses. Results reveal that the manganese-doped structure ($SrFe_{0.9}Mn_{0.1}O_{3-\delta}$) remained stable after extended runs, while the undoped sample $CaMnO_3$ started decomposing to double perovskite structure after 100 cycles.

Based on the new finding the modified calcium manganese perovskite structures can be a good candidate for future pilot tests.

Acknowledgments

Authors would like to thank the Department Of Energy of United States (DOE) for the award of a project (Award Number FE0008774).

Graphical materials list

List of Tables

References

1. Adanez, J., et al., *Progress in Chemical-Looping Combustion and Reforming technologies.* Progress in Energy and Combustion Science, 2012. **38**(2): p. 215-282.
2. Hossain, M.M. and H.I. de Lasa, *Chemical-looping combustion (CLC) for inherent separations—a review.* Chemical Engineering Science, 2008. **63**(18): p. 4433-4451.
3. Kenarsari, S.D., et al., *Review of recent advances in carbon dioxide separation and capture.* RSC Advances, 2013. **3**(45): p. 22739-22773.
4. Fujimori, T. and T. Yamada, *Realization of oxyfuel combustion for near zero emission power generation.* Proceedings of the Combustion Institute, 2013. **34**(2): p. 2111-2130.
5. Fryda, L., et al., *Study on ash deposition under oxyfuel combustion of coal/biomass blends.* Fuel, 2010. **89**(8): p. 1889-1902.
6. Sathre, R., et al., *A framework for environmental assessment of CO2 capture and storage systems.* Energy, 2012. **37**(1): p. 540-548.
7. Mattisson, T., *Materials for Chemical-Looping with Oxygen Uncoupling.* Hindawi Publishing Corporation ISRN Chemical Engineering, 2013. **2013**: p. 19.
8. Fan, L.-S., et al., *Chemical looping processes for CO2 capture and carbonaceous fuel conversion - prospect and opportunity.* Energy & Environmental Science, 2012. **5**(6): p. 7254-7280.
9. Rydéna and T.M. Anders Lyngfelta, De Chenb, Anders Holmenb, Erlend Bjørgumc, *Novel oxygen-carrier materials for chemical-looping combustion and chemical-looping reforming; LaxSr1−xFeyCo1−yO3−δ perovskites and mixed-metal oxides of NiO, Fe2O3 and Mn3O4.* International Journal of Greenhouse Gas Control 2008. **2**(1): p. 21-36.
10. Adánez, J., et al., *Ilmenite Activation during Consecutive Redox Cycles in Chemical-Looping Combustion.* Energy & Fuels, 2010. **24**(2): p. 1402-1413.
11. Leion, H., et al., *The use of ilmenite as an oxygen carrier in chemical-looping combustion.* Chemical Engineering Research & Design: Transactions of the Institution of Chemical Engineers Part A, 2008. **86**(9): p. 1017-1026.
12. Rydén, M., et al., *Chemical-Looping Combustion with Liquid Fuels.* Energy Procedia, 2013. **37**(0): p. 654-661.
13. Arjmand, M., et al., *Investigation of different manganese ores as oxygen carriers in chemical-looping combustion (CLC) for solid fuels.* Applied Energy, 2014. **113**(0): p. 1883-1894.
14. Shen, L., et al., *A mechanistic investigation of a calcium-based oxygen carrier for chemical looping combustion.* Combustion and Flame, 2008. **154**(3): p. 489-506.
15. Jing, D., et al., *Innovative Oxygen Carrier Materials for Chemical-Looping Combustion.* Energy Procedia, 2013. **37**(0): p. 645-653.
16. Chiu, P.C. and Y. Ku, *Chemical Looping Process - A Novel Technology for Inherent CO2 Capture.* Aerosol and Air Quality Research, 2012. **12**(6): p. 1421-1432.
17. Lyngfelt, A., *Chemical-looping combustion of solid fuels – Status of development.* Applied Energy, 2014. **113**(0): p. 1869-1873.

18. Bao, J. and Z.C. Li, Ningsheng, *Experiments of char particle segregation effect on the gas conversion behavior in the fuel reactor for chemical looping combustion.* Applied Energy, 2014. **113**(0): p. 1874-1882.
19. Zeng, L., et al., *Chemical looping processes - particle characterization, ionic diffusion-reaction mechanism and reactor engineering.* Reviews in Chemical Engineering, 2012. **28**(1): p. 1-42.
20. De Chen and R.L. Erlend Bjorgum, Kjersti omdahl Christensen, Anders Holmen, *Micokinetic model assisted catalyst design for steam methane reforming.* studies in surface science and catalysis, 2004. **147**(147): p. 139-144.
21. Richter and P.G. Holtappels, T ; Nakamura, T ; Gauckler, LJ *Materials design for perovskite SOFC cathodes.* Monatsh Chem, 2009. **140**: p. 985-999.
22. Oishi, M., et al., *Oxygen nonstoichiometry and defect structure analysis of B-site mixed perovskite-type oxide (La, Sr)(Cr, M)O3 (M=Ti, Mn and Fe).* Journal of Solid State Chemistry, 2008. **181**(11): p. 3177-3184.
23. Feng and M.Z. L.Q. Jiang, H.B. Liu, X. Zhou, C.H. Li *Formability of ABO3 cubic perovskites.* Journal of Physics and Chemistry of Solids 69 (2008) 967–974, 2008.
24. Chonghe Li and P.W. Kitty Chi Kwan Soh, *Formability of ABO3 perovskites.* Journal of Alloys and Compounds 2004. **372**: p. 40-48.
25. Pena, M. and J. Fierro, *Chemical Structures and Performance of Perovskite Oxides.* Chem. Rev, 2001. **101**: p. 1981-2017.
26. Zhu, L., et al., *Effects of Preparation Methods on the Catalytic Performance of LaMn0.8Mg0.2O3 Perovskite for Methane Combustion.* Chinese Journal of Catalysis, 2010. **31**(8): p. 1006-1012.
27. Voorhoeve, R.J.H., et al., *PEROVSKITE OXIDES - MATERIALS SCIENCE IN CATALYSIS.* Science, 1977. **195**(4281): p. 827-833.
28. Andoulsi, R., K. Horchani-Naifer, and M. Ferid, *Effect of the preparation route on the structure and microstructure of LaCoO3.* Chemical Papers, 2014. **68**(5): p. 608-613.
29. Hallberg, P., et al., *Chemical Looping Combustion and Chemical Looping with Oxygen Uncoupling Experiments in a Batch Reactor Using Spray-Dried CaMn1–xMxO3−δ (M = Ti, Fe, Mg) Particles as Oxygen Carriers.* Energy & Fuels, 2013. **27**(3): p. 1473-1481.
30. Labhsetwar, N., et al., *Ceramics in Environmental Catalysis: Applications and Possibilities.* Chinese Journal of Catalysis, 2012. **33**(9–10): p. 1611-1621.
31. Pishahang and S.S. Egil Bakken , Yngve Larring , Christopher Ian Thomas *Oxygen non-stoichiometry and redox thermodynamics of LaMn1−xCoxO3−δ.* Solid State Ionics, 2013. **231**: p. 49-57.
32. He, F., et al., *The use of $La_{1-x}Sr_xFeO_3$ perovskite-type oxides as oxygen carriers in chemical-looping reforming of methane.* Fuel, 2013. **108**(0): p. 465-473.
33. Evdou, A., V. Zaspalis, and L. Nalbandian, *$La_{1-x}Sr_xFeO_3$ perovskites as redox materials for application in a membrane reactor for simultaneous production of pure hydrogen and synthesis gas.* Fuel, 2010. **89**(6): p. 1265-1273.
34. Thursfield, A., et al., *Chemical looping and oxygen permeable ceramic membranes for hydrogen production – a review.* Energy & Environmental Science, 2012. **5**(6): p. 7421-7459.
35. Xiaoping, D.A.I., Y.U. Changchun, and W.U. Qiong, *Direct Methane Oxidation in the Absence of Gaseous Oxygen Using La0.8Sr0.2Fe0.9Co0.1O3 Perovskite Oxide as the Oxygen Carrier.* Chinese Journal of Catalysis, 2008. **29**(10): p. 954-956.
36. Zeng, Y. and S.R. Tamhankar, N ; Fitch, F; Acharya, D; Wolf, R *A novel cyclic process for synthesis gas production.* Chemical Engineering Science,, 2003. **58**(3-6): p. 577-582.
37. Readman, J.E., et al., *La0.8Sr0.2Co0.2Fe0.8O3-delta as a potential oxygen carrier in a chemical looping type reactor, an in-situ powder X-ray diffraction study.* Journal of Materials Chemistry, 2005. **15**(19): p. 1931-1937.
38. Dai, X., C. Yu, and Q. Wu, *Comparison of LaFeO3, La0.8Sr0.2FeO3, and La0.8Sr0.2Fe0.9Co0.1O3 perovskite oxides as oxygen carrier for partial oxidation of methane.* Journal of Natural Gas Chemistry, 2008. **17**(4): p. 415-418.
39. Murugan, A., A. Thursfield, and I.S. Metcalfe, *A chemical looping process for hydrogen production using iron-containing perovskites.* ENERGY & ENVIRONMENTAL SCIENCE, 2011. **4**(11): p. 4639-4649.
40. He, F., et al., *Synthesis of three-dimensionally ordered macroporous LaFeO3 perovskites and their performance for chemical-looping reforming of methane.* Chinese Journal of Catalysis, 2013. **34**(6): p. 1242-1249.

41. Nalbandian, L., A. Evdou, and V. Zaspalis, *La1−xSrxMyFe1−yO3−δ perovskites as oxygen-carrier materials for chemical-looping reforming.* International Journal of Hydrogen Energy, 2011. **36**(11): p. 6657-6670.
42. Toniolo, F.S., et al., *Structural investigation of LaCoO3 and LaCoCuO3 perovskite-type oxides and the effect of Cu on coke deposition in the partial oxidation of methane.* Applied Catalysis B: Environmental, 2012. **117–118**(0): p. 156-166.
43. Eudou, A., V. Zaspalis, and L. Nalbandian, *La(1-x)SrxMnO3-delta perovskites as redox materials for the production of high purity hydrogen.* International Journal of Hydrogen Energy, 2008. **33**(20): p. 5554-5562.
44. Ksepko, E. and T.S. Topolnicka, M *New perovskite-type Sr(Fe1-xCux)O3-sigma materials for oxygen transfer in chemical looping* Przemysl chemiczny 2010. **89**(6): p. 806-810.
45. Sarshar, Z., F. Kleitz, and S. Kaliaguine, *Novel oxygen carriers for chemical looping combustion: La1-xCexBO3 (B = Co, Mn) perovskites synthesized by reactive grinding and nanocasting.* Energy & Environmental Science, 2011. **4**(10): p. 4258-4269.
46. Valechha, A.P. and Y.T. S. Rayalu, Nitin Labhsetwar, *Improved Oxygen Carriers for Cleaner Energy Generation through Chemical Looping Combustion.* Journal of Novel Carbon Resource Scineces, 2011. **4**: p. 13-16.
47. Moradi, G.R., M. Rahmanzadeh, and F. Khosravian, *The effects of partial substitution of Ni by Zn in LaNiO3 perovskite catalyst for methane dry reforming.* Journal of CO2 Utilization, 2014. **6**(0): p. 7-11.
48. Rørmark, L. and K.S. Wiik, S.; Grande, T., *Oxygen stoichiometry and structural properties of La1−xAxMnO3±δ (A = Ca or Sr and 0 ≤ x ≤ 1).* J. Mater. Chem, 2002. **12 (4), 1058−1067**.
49. Bakken, E., T. Norby, and S. Stølen, *Nonstoichiometry and reductive decomposition of CaMnO3−δ.* Solid State Ionics, 2005. **176**(1–2): p. 217-223.
50. Leion, H. and Y.B. Larring, E ; Bredesen, R ; Mattisson, T ; Lyngfelt, A *Use of $CaMn_{0.875}Ti_{0.125}O_3$ as Oxygen Carrier in Chemical-Looping with Oxygen Uncoupling.* Energy Fuels 2009, 23, 5276–5283, 2009.
51. Rydén, M., A. Lyngfelt, and T. Mattisson, *CaMn0.875Ti0.125O3 as oxygen carrier for chemical-looping combustion with oxygen uncoupling (CLOU)—Experiments in a continuously operating fluidized-bed reactor system.* International Journal of Greenhouse Gas Control, 2011. **5**(2): p. 356-366.
52. Jing and H.L. Tobias Mattisson, Magnus Rydén, and Anders Lyngfelt, *Examination of Perovskite Structure CaMnO3-δ with MgO Addition as Oxygen Carrier for Chemical Looping with Oxygen Uncoupling Using Methane and Syngas.* Hindawi, 2013. **2013**.
53. Kallen, M. and M.D. Ryden, C ; Mattisson, T ; Lyngfelt, A *$CaMn_{0.9}Mg_{0.1}O_{3-\delta}$ as Oxygen Carrier in a Gas-Fired 10 kWthChemical- Looping Combustion Unit.* Industrial & Engineering Chemistry Research, 2013. 52(21): p. 6923-6932, 2013.
54. Arjmand, M., et al., *Sulfur Tolerance of CaxMn1-yMyO3-delta (M = Mg, Ti) Perovskite-Type Oxygen Carriers in Chemical-Looping with Oxygen Uncoupling (CLOU).* Energy & Fuels, 2014. **28**(2): p. 1312-1324.
55. Arjmand, M. and A.A. Hedayati, Abdul-Majeed ; Leion, Henrik; Ryden, Magnus ; Mattisson, Tobias, *CaxLa1–xMn1–yMyO3−δ (M = Mg, Ti, Fe, or Cu) as Oxygen Carriers for Chemical-Looping with Oxygen Uncoupling (CLOU).* Energy & Fuels, 2013.
56. Ksepko, E., *Perovskite-type $Sr(Mn_{1-x}Ni_x)O_3$ materials and their chemical-looping oxygen transfer properties.* International Journal of Hydrogen Energy, 2014. **39**(15): p. 8126-8137.
57. Ksepko, E. and T.T. Topolnicka, Ewa K.; Sciazko, Marek;, *Preparation and characteristics of solid Sr(Mn1-xNix)O-3 solutions in relation to their uses in chemical looping oxygen transfer* Przemysl chemiczny 2009. **88**(6): p. 674-676.
58. Hu, R., et al., *Preparation and catalytic activities of the novel double perovskite-type oxide La2CuNiO6 for methane combustion.* Catalysis Communications, 2012. **21**(0): p. 38-41.
59. Troncoso and M.J.M.-L. , J. A. Alonso and M. T. Fernández-Díaz, *Evaluation of Sr2MMoO6 (M=Mg, Mn) as anode materials in solidoxide fuel cells: A neutron diffraction study.* Journal of Applied Physics, 2013. 113(2), 2013: p. 023511-023511.
60. Y. P. Liu, e.a., *First-Principle Calculations of Half-MetallicDouble Perovskite La2BB'O6 (B,B'=3d transition metal).* Commun. Comput. Phys., 2013. 14(1): p. 174-185, 2013.
61. Nakamura, T. and J. CHOY, *Determination of ionic valency pairs via lattice constants in ordered perovskites (ALa)(Mn2+Mo5+)O6 (A = Ba, Sr, Ca) with applications to (ALa)(Fe3+Mo4+)O6, Ba2(Bi3+Bi5+)O6 and Ba2(Bi3+Sb5+)O6.* Journal of Solid State Chemistry, 1977. **20**(3): p. 233-244.
62. Li, C., et al., *Double perovskite oxides $Sr_2Mg_{1-x}FexMoO_{6-\delta}$ for catalytic oxidation of methane.* Journal of Natural Gas Chemistry, 2011. **20**(4): p. 345-349.

63. Ormerod, R.M., *Solid oxide fuel cells.* Royal Society of Chemistry, 2003. **32**: p. 17-28.
64. Falcón, H., et al., *Double perovskite oxides A2FeMoO6−δ (A=Ca, Sr and Ba) as catalysts for methane combustion.* Applied Catalysis B: Environmental, 2004. **53**(1): p. 37-45.
65. Pan, X., et al., *Effect of Co doping on the electrochemical properties of Sr2Fe1.5Mo0.5O6 electrode for solid oxide fuel cell.* International Journal of Hydrogen Energy, 2013. **38**(10): p. 4108-4115.
66. Huang, Y. and R.X. Dass, ZL ; Goodenough, JB, *Double perovskites as anode meterials for solid-oxide fuel cells.* Science, 2006. 312(5771): p. 254-257, 2006.
67. Zhang and Tianmin Hea, *Performance of double-perovskite Sr2−xSmxMgMoO6−δ as solid-oxide fuel-cell anodes.* Journal of Power Sources 196 2011. **196**: p. 8352– 8359.
68. Zhang, Q., T. Wei, and Y.-H. Huang, *Electrochemical performance of double-perovskite Ba2MMoO6 (M=Fe, Co, Mn, Ni) anode materials for solid oxide fuel cells.* Journal of Power Sources, 2012. **198**(0): p. 59-65.
69. Zhang and Q.H. Qingjun Zhoua, Tianmin He, *Double-perovskites $A_2FeMoO_{6-\delta}$ (A = Ca, Sr, Ba) as anodes for solid oxide fuel cells.* Journal of Power Sources 195 (2010) 6356–6366, 2010.
70. Zhou, Q., T. He, and Y. Ji, *SmBaCo2O5+x double-perovskite structure cathode material for intermediate-temperature solid-oxide fuel cells.* Journal of Power Sources, 2008. **185**(2): p. 754-758.
71. Zhu, Z., et al., *Investigation of SmBaCuCoO5+δ double-perovskite as cathode for proton-conducting solid oxide fuel cells.* Materials Research Bulletin, 2010. **45**(11): p. 1771-1774.
72. Jin, F., et al., *Characterization and evaluation of double perovskites $LnBaCoFeO_{5+\delta}$ (Ln = Pr and Nd) as intermediate-temperature solid oxide fuel cell cathodes.* Journal of Power Sources, 2013. **243**(0): p. 10-18.
73. Tao, S. and J. Irvine, *A redox-stable efficient anode for solid-oxide fuel cells.* Nature Materials, 2003. **2**(5): p. 320-323.
74. Huang, Y.-H., et al., *Double-Perovskite Anode Materials Sr2MMoO6 (M = Co, Ni) for Solid Oxide Fuel Cells.* Chemistry of Materials, 2009. **21**(11): p. 2319-2326.
75. Campbell, K.D., *Layered and double perovskites as methane coupling catalysts.* Catalysis Today, 1992. **13**(2–3): p. 245-253.
76. Vallet-Regi, M. and a.J.M.G.-C. E. Garcia, *Synthesis and characterization of a new double perovskite: LaCaMnCoO6.* Journal of the Chemical Society, Dalton Transactions, 1988(3): p. 775-779, 1988.
77. Jin, F. and Y.W. Shen, R; He, TM, *Double-perovskite $PrBaCo_{2/3}Fe_{2/3}Cu_{2/3}O_{5+\delta}$ as cathode material for intermediatetemperature solid-oxide fuel cells.* Journal of Power Sources 2013. **234**(0).
78. Didier, C., J. Claridge, and M. Rosseinsky, *Crystal structure of brownmillerite Ba2InGaO5.* Journal of Solid State Chemistry, 2014(0).
79. Qin, W., et al., *Theoretical study of oxidation-reduction reaction of Fe2O3 supported on MgO during chemical looping combustion.* Applied Surface Science, 2013. **266**: p. 350-354.
80. Tsipis, A.C., *DFT flavor of coordination chemistry.* Coordination Chemistry Reviews, 2014. **272**(0): p. 1-29.
81. Kagomiya, I., et al., *Oxygen vacancy formation and the ion migration mechanism in layered perovskite $(Sr,La)_3Fe_2O_{7-delta}$.* Physical Chemistry Chemical Physics, 2014. **16**(22): p. 10875-10882.
82. Shiiba, H., et al., *Calculation of arrangement of oxygen ions and vacancies in double perovskite GdBaCo2O5+delta by first-principles DFT with Monte Carlo simulations.* Physical Chemistry Chemical Physics, 2013. **15**(25): p. 10494-10499.
83. Wang, Y. and H.P. Cheng, *Oxygen Reduction Activity on Perovskite Oxide Surfaces: A Comparative First-Principles Study of LaMnO3, LaFeO3, and LaCrO3.* Journal of Physical Chemistry C, 2013. **117**(5): p. 2106-2112.
84. Cardona, R., et al., *Structural and magnetic properties of double-perovskite Ba2MnMoO6 by density functional theory.* Journal of Magnetism and Magnetic Materials, 2008. **320**(14): p. e85-e87.
85. Kronberger, Anders Lyngfelt, and a.H.H. Gerhard Loffler, *Design and Fluid Dynamic Analysis of a Bench-Scale Combustion System with CO2 Separation-Chemical-Looping Combustion.* Industrial & Engineering Chemistry Research 2005. **44**(3): p. 546-556.
86. Kimball, E. and A.F. Lambert, Anita; Leenman, Rebecca; Comte, Elodie; van den Bos, W. A. P.; Blom, Richard;, *Reactor choices for chemical looping combustion (CLC) — Dependencies on materials characteristics.* Energy Procedia, 2013. **37**(0): p. 567-574.
87. Miller, A.R., *FLUIDIZED BED REACTOR*, in *Indianapolis, Ind*, N. Union Carbide Corporation and N. York, Editors. 1977. p. 10.

88. Son, S.R., Kim, S.D., *Chemical-looping combustion with NiO and Fe_2O_3 in a thermobalance and circulating fluidized bed reactor with double loops.* Industrial & Engineering Chemistry Research 45 (8), 2689–2696., 2006.
89. Haslinger, W. and H.G. Hofbauer, L.; Boukis, I., *Scaleup guidelines for a circulating fluidized bed biomass pyrolyser In Circulating Fluidized Bed Technology VI.* Werther, J., Ed.; DECHEMA, 1999: p. 899-905.
90. Hofbauer, H. and H.V. Stoiber, G., *Gasification of Organic Material in a Novel Fluidization Bed System.* Proceedings of the 1st SCEJ Symposium on Fluidization, Tokyo, 1995: p. 291-299.
91. Pröll, T., et al., *Natural minerals as oxygen carriers for chemical looping combustion in a dual circulating fluidized bed system.* Energy Procedia, 2009. **1**(1): p. 27-34.
92. Noorman, S., M. van Sint Annaland, and J.A.M. Kuipers, *Experimental validation of packed bed chemical-looping combustion.* Chemical Engineering Science, 2010. **65**(1): p. 92-97.
93. Adanez, J.G.-L., F; de Diego, LF ; Gayan, P ; Celaya, J ; Abad, A *Nickel-copper oxygen carriers to reach zero CO and H-2 emissions in chemical-looping combustion.* INDUSTRIAL & ENGINEERING CHEMISTRY RESEARCH, 2006. **45**(8): p. 2617-2625.
94. Diego, L.F.d., et al., *Impregnated CuO/Al2O3 oxygen carriers for chemical-looping combustion: Avoiding fluidized bed agglomeration.* Energy & Fuels, 2005. **19**(5): p. 1850-1856.
95. Lyngfelt, A., B. Leckner, and T. Mattisson, *A fluidized-bed combustion process with inherent CO2 separation; application of chemical-looping combustion.* Chemical Engineering Science, 2001. **56**(10): p. 3101-3113.
96. Pröll, T., et al., *A novel dual circulating fluidized bed system for chemical looping processes.* AIChE Journal, 2009. **55**(12): p. 3255-3266.
97. Spallina, V., et al., *Integration of coal gasification and packed bed CLC for high efficiency and near-zero emission power generation.* International Journal of Greenhouse Gas Control, 2014. **27**(0): p. 28-41.
98. Jin, H. and M. Ishida, *Reactivity Study on Natural-Gas-Fueled Chemical-Looping Combustion by a Fixed-Bed Reactor.* Industrial & Engineering Chemistry Research, 2002. **41**(16): p. 4004-4007.
99. Noorman, S. and M.K. Annaland, H, *Packed bed reactor technology for chemical-looping combustion.* Ind Eng Chem Res 2007; 46:4212–20, 2007.
100. Dahl, I.M., et al., *On the development of novel reactor concepts for chemical looping combustion.* Energy Procedia, 2009. **1**(1): p. 1513-1519.
101. Fosse, S. and H.a.a.R. Blom, *Chemical Looping Combustion in a Rotating Bed Reactor Finding Optimal Process Conditions for Prototype Reactor.* Environmental Science and Technology, 2011.
102. Zhao and T.C. Chukwunwike O. Iloeje, Ahmed F. Ghoniem, *Design of a rotary reactor for chemical-looping combustion. Part 2: Comparison of copper-, nickel-, and iron-based oxygen carriers.* Fuel, 2014. **121**(0): p. 344-360.
103. Zhao, Z., T. Chen, and A.F. Ghoniem, *Rotary Bed Reactor for Chemical-Looping Combustion with Carbon Capture. Part 1: Reactor Design and Model Development.* Energy & Fuels, 2012. **27**(1): p. 327-343.
104. Zhao, et al., *Design of a rotary reactor for chemical-looping combustion. Part 1: Fundamentals and design methodology.* Fuel, 2014. **121**(0): p. 327-343.
105. Li, F., et al., *Syngas chemical looping gasification process: Bench-scale studies and reactor simulations.* AIChE Journal, 2010. **56**(8): p. 2186-2199.
106. Fan, L.-S., *Chemical looping systems for fossil energy conversions.* 1st ed2010: Wiley-AIChE.
107. Wolf, J., M. Anheden, and J. Yan, *Comparison of nickel- and iron-based oxygen carriers in chemical looping combustion for CO2 capture in power generation.* Fuel, 2005. **84**(7–8): p. 993-1006.
108. Kunii, D. and O. Levenspiel, *Fluidization Engineering*1991: Butterworth-Heinemann.
109. Peña, M.A. and J.L.G. Fierro, *Chemical Structures and Performance of Perovskite Oxides.* Chemical Reviews, 2001. **101**(7): p. 1981-2018.
110. Rormark, L., et al., *Oxygen stoichiometry and structural properties of La1 - AMnO3 +/- (A = Ca or Sr and 0 [less-than-or-equal] x [less-than-or-equal] 1).* Journal of Materials Chemistry, 2002. **12**(4): p. 1058-1067.
111. Lekse, J.W., et al., *Double Perovskite Materials for Applications in Chemical Looping and Oxygen Storage*, in *2012 AIChE Annual Meeting* 2012, American institute of chemical engineers: pittsburgh.
112. Jorge, M.E.M., A.C. Dos Santos, and M.R. Nunes, *Effects of synthesis method on stoichiometry, structure and electrical conductivity of CaMnO3-δ.* International Journal of Inorganic Materials, 2001. **3**(7): p. 915-921.

113. Ramezanipour, F., et al., *Systematic study of compositional and synthetic control of vacancy and magnetic ordering in oxygen-deficient perovskites Ca 2Fe 2-xMn xO 5+yand CaSrFe 2-xMn xO 5+y (x = 1/2, 2/3, and 1; Y = 0-1/2).* Journal of the American Chemical Society, 2012. **134**(6): p. 3215-3227.
114. Komiyama, T., et al., *Synthesis, thermal stability, and oxygen intake/release characteristics of YBa(Co1-xAlx)4O7+δ.* Materials Research Bulletin, 2010. **45**(10): p. 1527-1532.
115. Motohashi, T., et al., *Oxygen storage capability of Brownmillerite-type $Ca_2AlMnO_{5+\delta}$ and its application to oxygen enrichment.* Chemistry of Materials, 2013. **25**(3): p. 372-377.
116. Motohashi, T., et al., *Remarkable oxygen intake/release capability of BaYMn2O 5+δ: Applications to oxygen storage technologies.* Chemistry of Materials, 2010. **22**(10): p. 3192-3196.
117. Ramezanipour, F., et al., *Local and Average Structures and Magnetic Properties of Sr2FeMnO5+y, y = 0.0, 0.5. Comparisons with Ca2FeMnO5 and the Effect of the A-Site Cation.* Inorganic Chemistry, 2011. **50**(16): p. 7779-7791.
118. Fang, T.T., M.S. Wu, and T.F. Ko, *On the formation of double perovskite Sr2FeMoO6.* Journal of Materials Science Letters, 2001. **20**(17): p. 1609-1610.
119. Rager, J., et al., *Oxygen Stoichiometry in Sr2FeMoO6, the Determination of Fe and Mo Valence States, and the Chemical Phase Diagram of SrO-Fe3O4-MoO3.* Journal of the American Ceramic Society, 2004. **87**(7): p. 1330-1335.
120. Zötzl, M. and H. Pöllmann, *Stability and Properties of Brownmillerites Ca2(Al, Mn, Fe)2O5 and Perovskites Ca(Mn, Fe)O3−x in the System Ca2Fe2O5–"Ca2Mn2O5"–"Ca2Al2O5".* Journal of the American Ceramic Society, 2006. **89**(11): p. 3491-3497.
121. Palmer, H.M., et al., *Crystal Structure and Magnetic Properties of Ca2MnAlO5.5, an n = 3 Brownmillerite Phase.* Chemistry of Materials, 2006. **18**(5): p. 1130-1133.
122. Kosmulski, M., *IEP as a parameter characterizing the pH-dependent surface charging of materials other than metal oxides.* Advances in Colloid and Interface Science, 2012. **171–172**(0): p. 77-86.
123. Suntako, R., P. Laoratanakul, and N. Traiphol, *Effects of dispersant concentration and pH on properties of lead zirconate titanate aqueous suspension.* Ceramics International, 2009. **35**(3): p. 1227-1233.
124. Azimi, G., et al., *(MnzFe1—z)yOx combined oxides as oxygen carrier for chemical-looping with oxygen uncoupling.* AIChE Journal, 2013. **59**(2): p. 582-588.
125. Arjmand, M., et al., *CaxLa1–xMn1–yMyO3−δ (M = Mg, Ti, Fe, or Cu) as Oxygen Carriers for Chemical-Looping with Oxygen Uncoupling (CLOU).* Energy & Fuels, 2013. **27**(8): p. 4097-4107.
126. Tali, R., *Determination of average oxidation state of Mn in $ScMnO_3$ and $CaMnO_3$ by using iodometric titration.* Journal for BASIC SCIENCES, 2007. **23**(1): p. 9-19.
127. Priolkar, K.R. and R. Rawat, *Effect of heterovalent substitution at Mn site on the magnetic and transport properties of.* Journal of Magnetism and Magnetic Materials, 2008. **320**(3–4): p. 325-330.
128. Ramesh, K., et al., *Re-investigating the CO oxidation mechanism over unsupported MnO, Mn2O3 and MnO2 catalysts.* Catalysis Today, 2008. **131**(1–4): p. 477-482.
129. L.S.M. TRAQUEIA, F.M.B. MARQUES, and V.V. KHARTON, *Oxygen Ion Conduction in Oxide Materials: Selected Examples and Basic Mechanisms.* Bol. Soc. Esp. Ceram., 2006. **45** (3): p. 115-121.
130. Bossche, M.v.d., *Oxygen vacancy ordering in iron-doped calcium titanate*, in *Science and Technology Inorganic Materials Science*2005, University of Twente: Enschede. p. 59.
131. Hedayati, A., et al., *Evaluation of novel ceria-supported metal oxides as oxygen carriers for chemical-looping combustion.* Industrial and Engineering Chemistry Research, 2012. **51**(39): p. 12796-12806.
132. García-Labiano, F., et al., *Effect of Fuel Gas Composition in Chemical-Looping Combustion with Ni-Based Oxygen Carriers. 1. Fate of Sulfur.* Industrial & Engineering Chemistry Research, 2009. **48**(5): p. 2499-2508.
133. Sundqvist, S., et al., *CaMn0.875Ti0.125O3−δ as an Oxygen Carrier for Chemical-Looping with Oxygen Uncoupling (CLOU)—Solid-Fuel Testing and Sulfur Interaction.* Energy Technology, 2013. **1**(5-6): p. 338-344.
134. Sarshar, Z., et al., *Development of Sinter-Resistant Core–Shell LaMnxFe1–xO3@mSiO2 Oxygen Carriers for Chemical Looping Combustion.* Energy & Fuels, 2012. **26**(5): p. 3091-3102.
135. Kumar, S., et al., *Studies on surface composition and chemical states of calcium manganites.* Nuclear Instruments and Methods in Physics Research Section B: Beam Interactions with Materials and Atoms, 2005. **237**(3–4): p. 623-630.
136. Zampieri, G., et al., *Electronic structure of CaMnOx with 2.66<~x<~3.00 studied with photoemission and x-ray-absorption spectroscopy.* Physical Review B, 1998. **58**(7): p. 3755-3761.

137. Okimoto, Y., et al., *Anomalous Variation of Optical Spectra with Spin Polarization in Double-Exchange Ferromagnet: $La_{1-x}Sr_xMnO_3$.* Physical Review Letters, 1995. **75**(1): p. 109-112.
138. Arima, T.-h. and Y. Tokura, *Optical Study of Electronic Structure in Perovskite-Type RMO3 (R=La, Y; M=Sc, Ti, V, Cr, Mn, Fe, Co, Ni, Cu).* Journal of the Physical Society of Japan, 1995. **64**(7): p. 2488-2501.
139. Kim, K.H., et al., *Frequency Shifts of the Internal Phonon Modes in $La_{0.7}Ca_{0.3}MnO_3$.* Physical Review Letters, 1996. **77**(9): p. 1877-1880.
140. Pawar, R.P., et al., *Studies on (Sr1−xCax) MnO3 (0.0≤x≤1.0) ceramics having negative magnetization.* Journal of Magnetism and Magnetic Materials, 2014. **354**(0): p. 303-308.
141. Tan, T.-Y., et al., *Coupling of Jahn–Teller and tilting distortions in high temperature structural phase transition of the Ca0.2Sr0.6Nd0.2Mn1−xCrxO3; 0 ≤ x ≤ 0.2 perovskites.* Solid State Sciences, 2012. **14**(4): p. 506-514.
142. Lichtenthaler, T., *Ordering of oxygen vacancies in reduced phases of $CaMnO_{3-x}$ and $SrMnO_{3-x}$.*, in *Department of Chemistry*2005, University of Oslo.
143. St, et al., *Oxygen-deficient perovskites: linking structure, energetics and ion transport.* Physical Chemistry Chemical Physics, 2006. **8**(4): p. 429-447.
144. Sangar, N., *Nanocrystalline Perovskites for catalytic combustion and oxygen separation*, in *Chemical Engineering*2002, Massachusetts Institute of Technology.
145. Song, S., et al., *Oxygen permeation and partial oxidation of methane reaction in $Ba_{0.9}Co_{0.7}Fe_{0.2}Nb_{0.1}O_{3-\delta}$ oxygen permeation membrane.* Journal of Membrane Science, 2012. **415–416**(0): p. 654-662.
146. Arjmand, M.H., Ali; Azad, Abdul-Majeed ; Leion, Henrik; Ryden, Magnus ; Mattisson, Tobias, *$Ca_xLa_{1-x}Mn_{1-y}M_yO_{3-\delta}$ (M = Mg, Ti, Fe, or Cu) as Oxygen Carriers for Chemical-Looping with Oxygen Uncoupling (CLOU).* Energy & Fuels, 2013.
147. Rydén, M. and T.M. Anders Lyngfelta, De Chenb, Anders Holmenb, Erlend Bjørgumc, *Novel oxygen-carrier materials for chemical-looping combustion and chemical-looping reforming; $La_xSr_{1-x}Fe_yCo_{1-y}O_{3-\delta}$ perovskites and mixed-metal oxides of NiO, Fe_2O_3 and Mn_3O_4.* International Journal of Greenhouse Gas Control 2008. **2**(1): p. 21-36.
148. Richard Dronskowski, R.H., *Computational Chemistry of Solid State Materials: A Guide for Materials Scientists, Chemists, Physicists and others*2006.